Closing the Last Deglacial Global Sea-Level Budget by Different Antarctic Deglaciation Models

By

Yucheng Lin

31 May 2019

Declaration

This thesis is an account of research undertaken between July 2017 and May 2019

at the Earth Dynamics Group, Research School of Earth Sciences,

The Australian National University, Canberra, Australia.

Except where acknowledged in the text,

this thesis represents original work by the author.

Word Count: 20,624

Yucheng Lin 林玉成

Yucheng Lin

May 2019

Acknowledgements

Abstract

The last deglacial history of the Antarctic Ice Sheet (AIS), the world's largest freshwater reservoir, is important for monitoring the current AIS change and projecting the future sea-level rise trend. However, due to the lack of direct observational constraints on AIS last deglacial history, currently, most of the knowledge of AIS deglaciation is from glacial isostatic adjustment (GIA) modelling studies. Currently, the most widely used AIS GIA models are ICE-6G_C (Argus et al., 2014, Peltier et al., 2015), W12 (Whitehouse et al., 2012a) and IJ05_R2 (Ivins et al., 2013). Although after combining with their preferred Earth models, they all show good capability to predict reasonable predictions compared to the geodetic observations (e.g, Global Positioning System), the great differences between their adopted deglaciation models would cause large uncertainties in their estimations. Here we show a global sea-level budget consistent GIA modelling approach to compare them with two high-quality far-field sea-level datasets (H18; Hibbert et al., 2018, L14; Lambeck et al., 2014) constructed using different underlying philosophies to test their compatibilities with the far-field sea-level observations. Similar to a previous study of Lambeck et al. (2014), the global sea-level budget in this study is defined by the global ice volume history reconstructed from each observational datasets. From our calculation, a large ice mass loss between 20-15 ka BP predicted by W12 is most likely to be incorrect, since it shows large inconsistencies with both observational datasets, suggesting that during this late glacial period, AIS should have a stable or an advanced phase. And during ~15-11 ka BP, far-field sea-level records shows a preference with ICE-6G_C, which is the only model with a distinct contribution to meltwater pulse 1a and 1b, showing good consistency with the much more dynamic cryospheric environment revealed by the new global ice volume history reconstruced from the H18 dataset, as well as previous GIA studies (e.g., Clark et al., 2002).
.

Content

List of Abbreviations

AD	Anno Domini
ANU	Australian National University
AIS	Antarctic Ice Sheet
BP	Before present
BIS	British Ice Sheet
cm	Centimetre
ESL	Ice-equivalent sea level/Eustatic sea level
EIS	Eurasia Ice Sheet
GBR	Great Barrier Reef
GIA	Glacial isostatic adjustment
GPS	Global Positioning System
GRACE	Gravity Recovery And Climate Experiment
GMSL	Global mean sea level
GOCE	Gravity Field and Steady-State Ocean Circulation Explorer
Gt	Gigaton
LGM	Last Glacial Maximum
McMC	Markov chain Monte Carlo
MWP-1A	Meltwater Pulse-1A
MWP-1B	Meltwater Pulse-1B
NAIS	North American Ice Sheet
PDF	Probability density function
P_{RSL}	Probability maximum sea level
RSL	Relative sea level
SD	Standard deviation
ICESat	Ice, Cloud, and land Elevation Satellite
InSAR	Interferometric Synthetic Aperture Radar
IHD	Ice height difference
IRD	Ice-rafted debris
ka	Thousand years
km	Kilometre
Pa s	Pascal-second
yr	Year
WAIS	West Antarctic Ice Sheet

Chapter 1 Introduction

In the contemporary world, 2.4 billion people, nearly one-third of the total human population, live within 100 kilometres of the coastal area. The great majority of them are at risk from natural hazards associated with global sea level rise, such as flooding, leading to unpredictable economic loss every year. This fact was emphasised by the devastating flooding caused by Typhoon Mangkhut in September 2018, which resulted in over 1.2 billion dollars economic loss in China (News China, 2018). The impact of such events will only get worse as sea level continues to rise. Hence, much attention now has been given to measuring and predicting the meltwater discharge from the Antarctic Ice Sheet (AIS), the world's largest freshwater reservoir, which is projected to be the dominant source of global sea level rise by the end of the 21st century (Stocker, 2014). Currently, the two widely-used methods of measuring AIS meltwater discharge involve interpreting gravity anomalies induced by ice mass loss (as measured by the Gravity Recovery and Climate Experiment (GRACE) and GRACE Follow-On satellites) and ice sheet elevation change (as measured by satellite altimeters such as ICESat-2). However, both of these methods are strongly contaminated by glacial isostatic adjustment (GIA; details are described in Chapter 2), a geophysical signal caused by the interaction between solid Earth and the melting of past ice sheets that results in ongoing changes to the gravity field, bedrock topography and land motion in Antarctica. Therefore, to develop more accurate measurements of the AIS melting rate and a better projection of future sea-level rise trend, GIA signal must be removed from geodetic measurements.

Currently, ice history and Earth rheology parameters, the two primary prerequisites of estimating GIA signal, are both poorly-constrained in Antarctica, which significantly hinders the understanding of present GIA signal, and hence, the interpretation of satellite geodetic measurements. Particularly, Antarctic ice history during the last deglaciation (from ~20 ka BP to present) is vigorously debated due to the poor quality of the observational data relating to the past extent of the AIS (~100 direct observational data in total of past ice sheets height since Last Glacial Maximum, LGM; e.g., Bentley et al., 2014), which mainly owing to Antarctica's remote geographical position, severe climate and ice coverage. Consequently, the estimates of the Antarctic contribution to last deglacial global sea-level rise range from 2.5 m (Colhoun et al., 1992) to

above 20 m (Bassett et al., 2007, Lambeck et al., 2014, Nakada et al., 2000). A further complication when investigating present GIA signal is the complex Earth internal structure in Antarctica (Nield et al., 2018). Seismic studies reveal that Antarctica is considered to be composed of two distinct regions defined by Earth internal structure: a thick cratonic lithosphere and a high-viscosity uppermost mantle in East Antarctica, and thinner lithosphere and lower viscosity uppermost mantle in West Antarctica (Morelli and Danesi, 2004). This means that of the regions in overlying high-viscosity mantle (e.g., East Antarctica) GIA signals are sensitive to ancient ice history (e.g., ice history from the LGM to Holocene), whereas in the region underlain by lower viscosity mantle (e.g., Amundsen Sea), only the recent ice history is relevant (e.g., past few decades to centuries; Barletta et al., 2018).

During the past decade, multiple numerical approaches have been developed and combined with an improved Antarctic observational dataset of past ice sheet extent (e.g., sea-level records and glacio-geological evidence) for reconstructing Antarctic ice history since the LGM, such as W12/W12a (Whitehouse et al., 2012a, Whitehouse et al., 2012b), IJ05_R2 (Ivins et al., 2013) and ICE-6G_C (Argus et al., 2014, Peltier et al., 2015). These ice models are combined with their preferred Earth models to estimate the GIA-induced gravity anomaly signal and remove it from GRACE data. This results in different estimates of Antarctic mean ice-mass change from 2003 to 2012: -69 ± 18 Gt yr^{-1}, -57 ± 34 Gt yr^{-1} and -124 ± 34 Gt yr^{-1} are obtained for W12a, IJ05_R2 and ICE-6G_C respectively (Argus et al., 2014, Nield, 2014). The accuracy of these estimates relies on the validity of their corresponding ice history models. Although all ice models show a relatively good fit with selected observational evidence, such as paleo grounding line positions, moraine positions and relative sea-level indicators, different underlying modelling strategies (e.g., ice physics approach and GIA analysis approach) produce models which differ in the manner in where and when the deglaciation occurs.

With different Earth models all these ice models are able to generate a good fit to the present-day GIA uplift signal, however, the timing and pattern of far-field (i.e., located far away from large continental ice sheets) sea-level rise induced by the melting of these ice models are not identical. Comparing these modelled sea-level rise patterns with observational sea-level indicators (e.g., coral reef and organic matter) can provide insights into the validity and accuracy of the melting time and magnitude of these ice models. So far, there

is no systematic analysis on how these regional Antarctic ice models (except ICE-6G_C which is a global ice model) correspond to the last deglacial global sea-level rise pattern recorded by observational evidence. This research aims to improve this critical knowledge gap and provide new information for improving current Antarctic ice models or building the next generation of ice model.

Chapter 2 Background

This research focuses on improving the understanding of Antarctic ice history and global sea-level variation during the last deglaciation, which is a multi-disciplinary challenge that requires comprehensive knowledge involving glacial isostatic adjustment (GIA), sea-level change reconstruction, ice-sheet reconstruction and the global sea-level budget. This chapter will describe the necessary background and underlying theories of these subjects.

2.1 Glacial Isostatic Adjustment Modelling

Glacial isostatic adjustment (GIA) describes the response of solid Earth, oceans and global gravitational field to the changing surface load, mainly attributed to the growth and decay of global ice sheets (see Figure 2.1). Because of the viscous-fluid behaviour of Earth's mantle, the solid Earth response to the changing ice load is a time-delayed process. The relaxation time of this process depends on the magnitude of change in ice load and viscosity of Earth's mantle, varying from decadal time scales (caused by low mantle viscosity, i.e., ~10^{18} to 10^{19} Pa s; Barletta et al., 2018) to millennial time scales (caused by high mantle viscosity, i.e.,
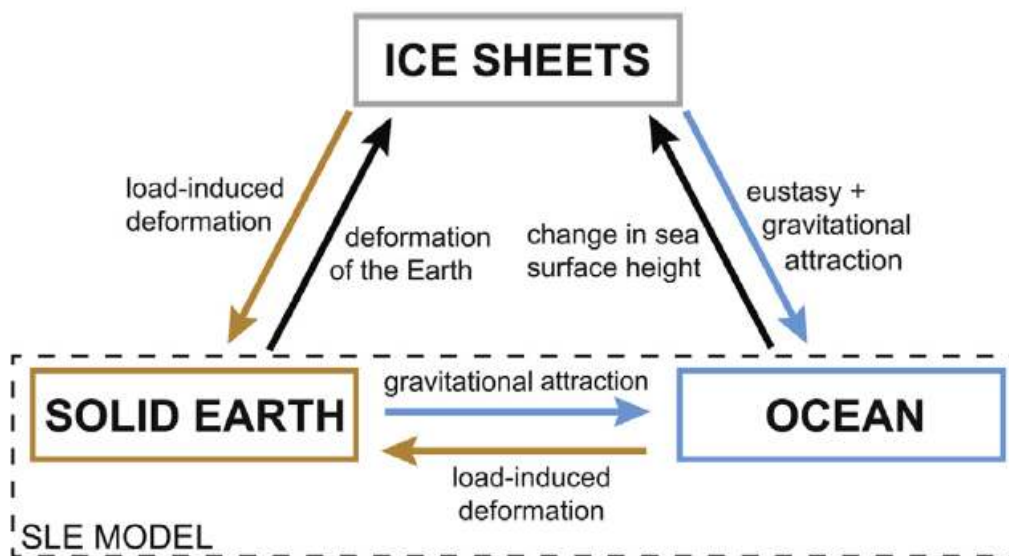
Figure 2.1. A simplified schema giving an overview of the interactions between ice sheets, solid Earth and the ocean included in a GIA model. Ice sheets are modelled with multi-disciplinary approaches, solid Earth response is calculated using a viscoelastic Earth model, ocean surface is governed by the shape pf geoid. The combination of ocean and solid Earth components represent the change in relative sea level as governed by solving sea-level equation (SLE, dashed box). Figure from (De Boer et al., 2017).

~10^{20} to 10^{21} Pa s). Thus, following the decay of the ice sheets from the end of the LGM, the solid Earth underneath formerly glaciated areas (e.g., North America, Scandinavia and Antarctica) is still uplifting at a rate of up to 20 mm yr^{-1} today (Lambeck et al., 2017, Milne et al., 2001, Peltier et al., 2015), which implies the solid Earth is not in isostatic equilibrium.

As the most direct way to explore Earth's mantle property, understanding GIA is not only useful for constraining mantle viscosity (e.g., Lambeck et al., 2017, Lau et al., 2018, Mitrovica and Forte, 2004, Nakada et al., 2017), but also one of the major techniques to constrain the extent of former ice sheets by exploring present-day GIA signals (e.g., Argus et al., 2014, Gomez et al., 2013, Ivins et al., 2013, Lambeck et al., 2017, Peltier et al., 2015, Whitehouse et al., 2012a). A vital additional extension of GIA is that it describes meltwater redistribution in a gravitationally consistent way by solving the sea-level equation (Farrell and Clark, 1976), which makes it possible to model the complicated GIA-related processes of relative sea-level change (RSL; i.e., distance between the local ocean and solid Earth surface) during glacial cycles (details in section 2.1.1). In general, there are two essential inputs to a numerical model to predict GIA related processes introduced above: (*i*) A history of the global sheets (describing how global ice geometry and volume varied with time) (*ii*) and an Earth model (describing the Earth's internal structure and properties that determines how Earth responds to the changing surface load).

2.1.1 *Development of Fundamental Theory*

As one of the few geophysical processes that can be readily observed without sophisticated measurement techniques in human timescales, GIA has long been recognized in Scandinavia. A typical example is the relocation of ancient Östhammar port, which has moved seaward due to land uplift which made former port no longer accessible by boat in AD 1491 (Ekman, 2009). In the 18th century, the first scientific measurement of GIA was carried out and concluded the RSL in the Gulf of Bothnia was falling at a rate of 1.4 cm yr^{-1} (Celsius, 1743), but Celsius wrongly suggested the notion that this RSL drop was due to water evaporation. In the following century, Agassiz (1840) proposed that the Earth experienced a past ice age (Evans, 1887). And based on this theory, from discovering marine sediments above current sea level in Forth Valley, Scotland, Jamieson (1865) inferred that the reason for local RSL drop was not water evaporation. Instead,
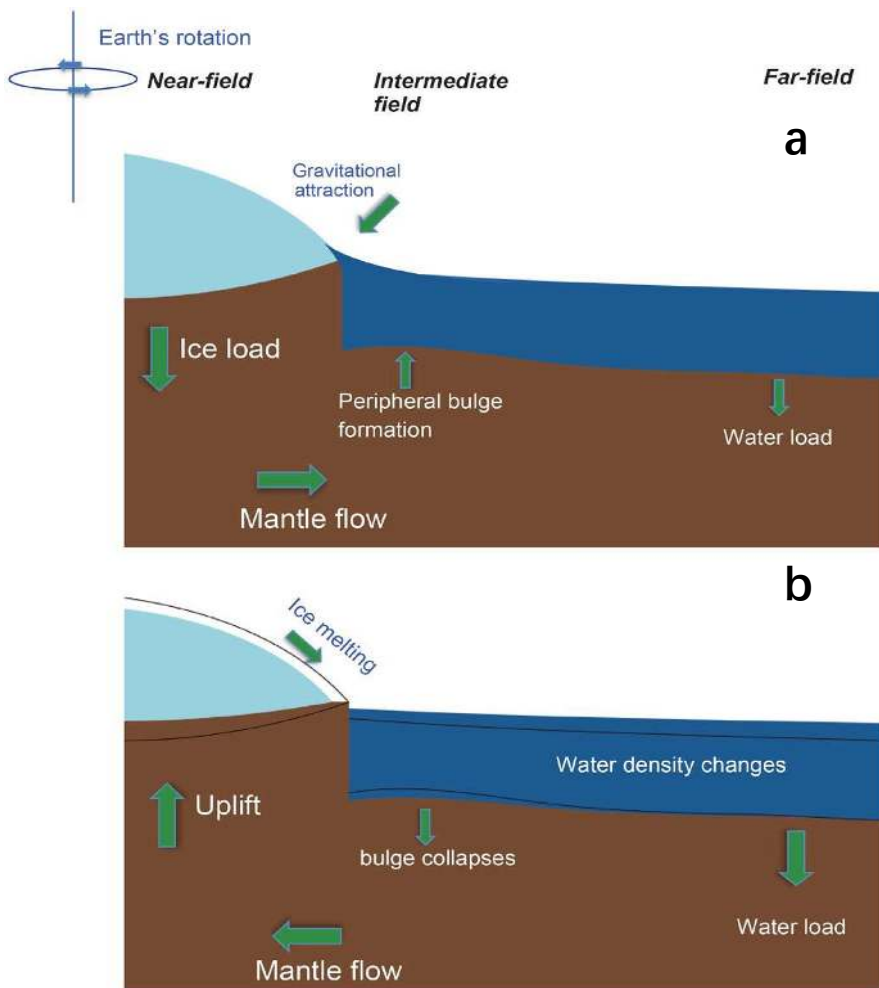
Figure 2.2 Schematic diagram of physical processes and their impact associated with GIA. (a) During the ice age (e.g., LGM), GIA effects include: mantle underlying an accreting ice sheet slowly flows away, creating a crust topographic depression in near-field with an intermediate-field peripheral bulge; gravitational attraction toward the ice margin to adjacent seawater; perturbation of Earth's rotational vector. (b) During the ice melting age (e.g., Last Deglaciation), mantle slowly flows back to re-establish isostatic equilibrium, causing crust rebound and bulge collapses; local gravitational attraction on seawater decrease; shape of solid Earth and geoid changes due to Earth's rotation (not shown); water load causes the oceanic crust deformation. Figure from (Yokoyama and Esat, 2011).

he proposed the weight of the former ice sheet must have depressed the land below sea level, and after the decay of the former ice sheet, the land began to rebound, which leads to the local RSL drop (see Figure 2.2). This conjecture was further confirmed and became well-accepted by a study on Scandinavia's ancient coastlines (De Geer, 1896).

Several fundamental theories were developed to explain the observed natural processes in the late 18th century, and people started to carry out detailed calculations to quantify GIA effects, which form the basis of contemporary GIA models. Woodward (1888) performed calculations related to geoid (shape of ocean surface defined by gravity and Earth rotation) variation caused by redistribution of the surface mass associated with growth and decay of ice sheets. He took into account the self-gravitational effect and mass conservation when transferring water between ice sheets and ocean, which explains the near-field (i.e., located near large ice sheets) geoid drop during the deglacial period (see Figure 2.2 b). Nansen (1921) used

the concepts of isostasy and mass balance to show that the Earth would continue to deform viscously for a prolonged period following the retreat of the ice sheets (see Figure 2.2 b). Haskell (1935) further explored mantle viscosity (~10^{21} Pa s for upper mantle) and formally provided a solution for recovery of fluid after removal of a load, but he omitted the details for mathematical treatment due to the prohibitive amount of computational labour required.

2.1.2 *Sea-Level Equation*

As computational resources continued to improve, studies into the viscosity of Earth's mantle and meltwater redistribution developed rapidly from the 1960s onward (e.g., Peltier, 1974, Farrell and Clark, 1976, Lambeck, 1980, McConnell, 1968). Peltier (1974) used Green's functions and the viscoelastic correspondence principle to formally establish a spherically symmetric, self-gravitating, non-rotating and radially stratified Earth model with a Maxwell-viscoelastic rheology to calculate solid Earth deformation responding to changing surface load. This theory was then applied to solve the sea-level equation assuming a non-rotating Earth with fixed ocean area, which defines the gravitationally self-consistent redistribution of meltwater across the ocean (Farrell and Clark, 1976). Thus, given the global ice load history and solid Earth parameters, spatially varying RSL history can be uniquely determined by solving the sea-level equation. Following their seminal investigation, extensive theoretical development of sea-level equation has been covered in the next decades to incorporate time-varying ocean functions (i.e., shoreline migration; Johnston, 1993, Kendall et al., 2005, Lambeck and Nakada, 1990, Wu and Peltier, 1984), Earth-rotational feedback (e.g., Lambeck, 1980, Wu and Peltier, 1984, Milne and Mitrovica, 1998, Mitrovica et al., 2005) and floating ice in shallow basins (Lambeck et al., 2003, Milne and Mitrovica, 1996). After these theoretical improvements, GIA model has successfully explained a series of complicated natural phenomena including 'ocean syphoning' effect (Mid-Holocene highstand; Mitrovica and Milne, 2002) and 'continental' levering effect (Lambeck and Nakada, 1990). The theory of sea-level equation is now well established and has been successfully implemented by different numerical methods that show a satisfactory agreement with each other (see Spada et al., 2011, Martinec et al., 2018 for benchmarking studies of different numerical implementations used to determine the response of solid Earth to changing surface load and sea-level equation).

Here we restate the main form of the sea-level equation to illustrate some underlying theories, following the notation of Spada and Stocchi (2006), starting from the definition of relative sea level (RSL):

$$RSL(\omega, t) = N(\omega, t) - U(\omega, t) \quad [2.1]$$

where $\omega \equiv (\theta, \lambda)$, θ is colatitude and λ is longitude; t is time with respect to present. $N(\omega, t)$ represents absolute sea level denoted as the distance between sea surface and centre of mass of the solid Earth, and $U(\omega, t)$ is the height of seafloor relative to solid Earth's centre of mass. Within the oceans, $RSL(\omega, t)$ value is always positive. Equation [2.1] illustrates that the RSL change depends not only on the height of sea surface but also the seafloor surface. Variation of these two surfaces both occurs in response to changing surface load, which is calculated within the sea-level equation (notation given by Spada and Stocchi, 2006):

$$S(\omega, t) = \frac{\rho_i}{\gamma} G_s \otimes_i I + \frac{\rho_w}{\gamma} G_s \otimes_o S - \frac{m_i}{\rho_w A_o} - \frac{\rho_i}{\gamma} \overline{G_s \otimes_i I} - \frac{\rho_w}{\gamma} \overline{G_s \otimes_o S} \quad [2.2]$$

where $S(\omega, t)$ describes the spatio-temporal change of relative sea level (with respect to present-day RSL) responds to the ice and ocean loading histories, I and S respectively, which are also functions of location and time. The first two terms of the right hand side of equation [2.2] describe the spatial varying perturbation to sea level due to the ice and ocean load; ρ_i and ρ_w are the ice and ocean water density; γ is the reference gravity at the surface of the Earth; G_s is the Green's function that describes the solid Earth displacement and gravitational potential perturbation due to changes in surface load (described in section 2.1.3), constructed by combining viscoelastic surface load Love numbers (described in section 2.1.4); $\otimes_i$ and $\otimes_o$ denote convolutions in space and time over the ice sheets and ocean respectively. The third term of equation [2.2] is often referred as the 'eustatic' term of sea-level change, which is the spatially uniform sea-level change across the ocean area A_o caused by a change in ice mass m_i. By the definition of mass conservation, mass gain in oceans equals to the mass loss in ice sheets, which can be expressed into sea-level change as:

$$\frac{m_i}{\rho_w A_o} = \overline{S(\omega, t)} \quad [2.3]$$

where overbar means average over the area of ocean. This term is sometimes also referred as 'ice-volume equivalent sea level' (although this conversion is not straightforward) or 'global mean sea level' change (e.g., Yokoyama et al., 2019a). The last two terms of equation [2.2] represent the spatial average of the first two terms (indicated by overbar), which must be subtracted to ensure overall mass conservation. Since the unknown variable $S(\omega, t)$ appears on the both sides of equation [2.2], the sea-level equation is an implicit equation and needs to be solved iteratively.

2.1.3 *Green's Function*

The sea-level Green's function, G_s in equation [2.2], used to describe solid Earth rheology, is given by:

$$G_s(\theta', \lambda', t) \equiv G_\emptyset - \gamma G_u \quad [2.4]$$

which governs the offset between the geoid and seafloor topography at location θ', λ' relative to the load center. The Green's functions $G_\emptyset$ and G_u are used to calculate the perturbations to gravitational potential ($\emptyset$) and solid Earth vertical deformation (u) in response to surface loading due to a point load on a spherically symmetric, radially stratified (i.e., 1-D) Earth model with an effectively elastic lithosphere and a liquid core (e.g., Tushingham and Peltier, 1992), based on Maxwell viscoelastic Love number theory (Peltier, 1974). The viscoelastic Green's functions in equation [2.4] are given by (Spada and Stocchi, 2006):

$$\begin{Bmatrix} \frac{1}{\gamma} G_\emptyset \\ G_u \end{Bmatrix} (\theta', t) = \frac{a}{m_e} \sum_{l=0}^{\infty} \begin{Bmatrix} k_l \\ h_l \end{Bmatrix} (t) P_l(cos\theta') \quad [2.5]$$

where a and m_e are the mean radius and mass of the solid Earth; l is spherical harmonic degree, k_l and h_l are the time-varying Love numbers for gravitational potential and vertical displacement, respectively. $P_l(cos\theta')$ represents the Legendre polynomial.

2.1.4 *Love Numbers*

The load-deformation coefficients, so-called 'Love numbers', in the Green's function reflect the solid Earth's structure and rheology, and are one of the two key inputs to a GIA model. Love numbers govern the deformation of solid Earth and the resulting perturbation of the geoid in response to surface load for

given Earth properties. Love numbers k_l and h_l in equation [2.5] can be compactly expressed as (Spada and Stocchi, 2006):

$$\begin{Bmatrix} k_l \\ h_l \end{Bmatrix}(t) = \begin{Bmatrix} 1 + k_l^e \\ h_l^e \end{Bmatrix}\delta(t) + H(t)\sum_{j=1}^{M}\begin{Bmatrix} k_{lj} \\ h_{lj} \end{Bmatrix}e^{-t/\tau_{lj}} \quad [2.6]$$

which are sum of an elastic and a viscous component. The first term on the right-hand side of equation [2.6] is the elastic part (depends only on the elastic properties) which contains a local impulsive load $\delta(t)$ (Dirac's delta) multiplied by the elastic Love numbers for gravitational potential k_l^e and solid Earth vertical displacement h_l^e. The last term of equation [2.6] represents the viscos response, which is the sum over the viscoelastic modes M of the viscoelastic Love numbers k_{lj} and h_{lj} multiplied by Heaviside step function $H(t)$ given by:

$$H(t) = \begin{cases} 1, & t \geq 0 \\ 0, & t < 0 \end{cases} \quad [2.7]$$

τ_{lj} is relaxation time of the j-th viscoelastic mode that depends on the solid Earth's properties. The number of viscoelastic modes is governed by the stratification of the Earth model.

2.1.5 *Earth Models*

As one of two essential inputs for a GIA model, the Earth model not only governs how the solid Earth responds to changes in surface load but also has an impact on ice sheet variation by changing topography underneath the ice sheet. Thus, exerting a fundamental control on ice dynamics as well as the position of the grounding line (see, e.g., Adhikari et al., 2014, Gomez et al., 2013, 2018, Whitehouse et al., 2019). Knowledge of Earth parameters like internal stratification (or 3-D structure), mantle viscosity, lithosphere thickness and internal rheology is limited and can only be inferred rather than measured. This, in turn, becomes a multi-disciplinary challenge involving different research areas such as seismic imaging (e.g., Lloyd, 2018), experimental petrology (e.g., Faul and Jackson, 2005, Ranalli and Fischer, 1984) and 3-D Earth modelling (e.g., through 3-D finite element model; see Wahr and Zhong, 2012, Wu and van der Wal, 2003). Since the key point of this research is not improving the Earth model, here we do not give a further introduction on Earth models. For a full review of the Earth model's impact on Antarctic ice sheet evolution and GIA studies, the reader is referred to Whitehouse et al. (2019).

2.2 Glacial Isostatic Adjustment Observations

Because GIA impacts a large variety of geophysical processes (Figure 2.1), there are various types of observational data for constraining different unknown parameters associated with ice history and Earth rheology. Table 2.1 gives a brief description of different types of GIA observations. For each observational data type, attention must be paid to whether there are unmodelled processes reflected in datasets that may strongly bias the analysis results (e.g., tectonic processes impact on interpolations of RSL records and seasonal hydrological impacts on geodetic gravimetry) and whether the assigned errors are realistic (e.g., different paleo sea-level indicators' uncertainties).

2.2.1 *Relative Sea-Level*

There are several types of observational RSL indicators that can provide valuable information on the past sea-level change (Murray-Wallace and Woodroffe, 2014), such as coral reef, paleo shorelines and fossil shell. The recorded RSL signal reflects the $S(\omega, t)$ in equation [2.2], which represents the RSL value relative to present sea level. Because over relatively short geological time scale (tens of thousands of years) the influences on global sea-level variation are dominated by water exchange between ice sheets and ocean (Ruddiman, 2001), RSL indicators are widely-used for constraining global grounded ice volume at the LGM (e.g., Yokoyama et al., 2001) as well as understanding last deglacial sea-level rise signal (e.g., Lambeck et al., 2014).

To reconstruct past sea-level history from sea-level indicators, three parameters must be known (including associated uncertainties): (*i*) the records' age (e.g., using radiocarbon or uranium-series dating); (*ii*) current elevation of sea-level records; (*iii*) the relationship between the sea-level indicator and past mean sea level. Among these prerequisites, the relationship between the sea-level indicator and past mean sea level is currently the most problematic issue that hampers the accuracy of sea-level reconstructions (record dating used to be the biggest problem before the arrival of modern dating methods such as radiometric dating). This problem arises from the complicated spatio-temporal varying ecological controls on the depth-habitat relationship, for example, the local temperature, salinity, nutrient availability, turbidity and hydrodynamics can all alter the depth at which a particular marine species can survive (Hibbert et al., 2016). But if the living-depth is known (sometimes with large uncertainties), past water depth at a specific age and location

Table 2.1. GIA Observations Summary

GIA Unknowns	Observations (with an example study)	Indications	Errors or Uncertainties
Ice History	Glacio-geological evidence (e.g., Hillenbrand et al., 2014)	Past ice grounding line positions; past ice sheet height; paleo-environment	Limited data amount leads to contradictory interpretations of ice grounding line scenarios (e.g., Weddell Sea, Antarctica); ice core air bubble analysis of past ice sheet height is affected by several not well-known processes
	Biological indicator (e.g., stomach oil deposit; see Hiller et al., 1988)	Past ice sheet height and paleoenvironment	Both containing unknown GIA signal; limited number of integrated records (e.g., may be compacted or displaced);
	Cosmogenic surface exposure dating (e.g., Small et al., 2019)	Past ice sheet height; Lower limit of the timing of ice retreat	Ambiguous interpretations; contains unknown GIA signal;
	RSL records (e.g., Yokoyama et al., 2018)	Ice sheet geometry; global ice volume	Poorly-constrained ecological effects on paleo depth-habitat distribution; affected by tectonic motions; sensitive to both ice geometry and Earth parameter
Earth Rheology	Surface deformation (e.g., measured by GPS, InSAR and altimetry; see Milne et al., 2001)	Mantle viscosity; past ice volume/geometry	Difficult to disentangle contributions from past and recent ice melting effects; affected by plate motion and hydrological cycle
	Gravity anomaly (e.g., GRACE and GOCE; see Root et al., 2015)	Viscosity structure; past ice thickness; spatial pattern of local GIA signal	Difficulties in disentangling the signal induced by solid Earth and ice mass loss; contaminated by non-GIA-related signal like hydrological cycles or tectonic movements
	Seismic signals (e.g., through seismic anisotropy and resistivity inversion; see Eaton et al., 2009)	Elastic and density structure of Earth; lithosphere thickness; mantle viscosity	Seismic-induced elastic lithosphere thickness is not necessarily relevant for GIA study; no direct relationship between seismic wave velocity and mantle viscosity, interpretation is ambiguous
	Solid Earth oblateness (e.g., Mitrovica and Wahr, 2011)	Lower mantle viscosity	Difficult to disentangle the long-term and contemporary response to mass redistribution

InSAR and GOCE stands for Interferometric Synthetic Aperture Radar and Gravity Field and Steady-State Ocean Circulation Explorer, respectively.
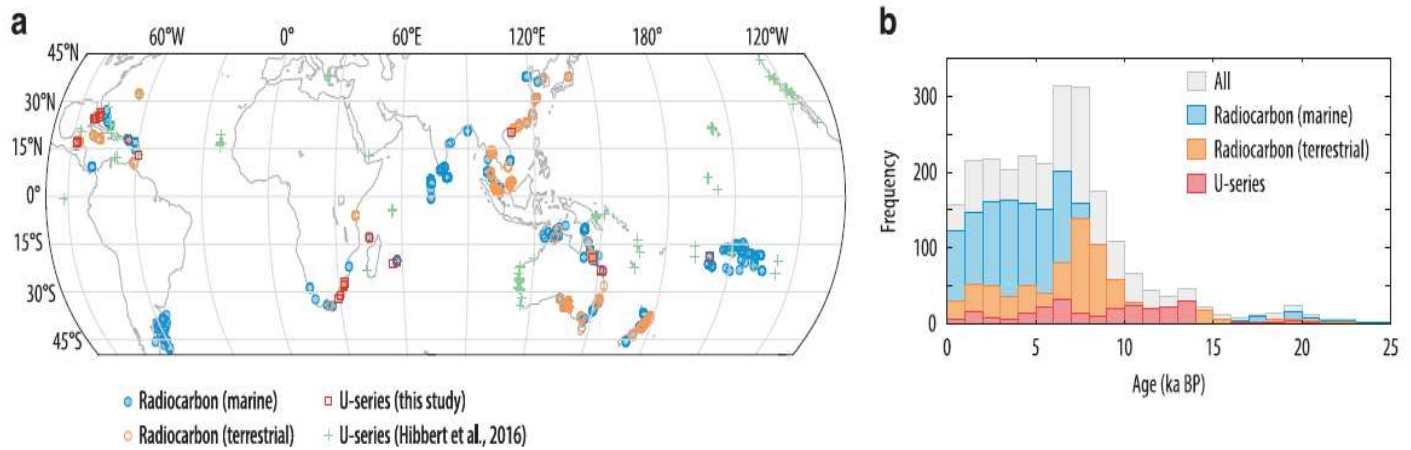
Figure 2.3. An example of location and age of far-field RSL records (a) Location of RSL records (b) Age frequency of RSL records. Colours represent for different dating methods. Figure from (Hibbert et al., 2018).

can be determined. Currently, most of the paleo-ecological controls on biological RSL indicators are still poorly known, so the most commonly used method is to assume that the modern depth-habitat relationship is representative of the past (further details will be discussed in Chapter 3 & 4). After decades of work on determining past RSL from sea-level indicators, a reasonable saptio-temporal coverage of sea-level data from the LGM has been achieved (see Figure 2.3 for an example of the spatio-temporal distribution of far-field sea-level data).

2.2.2 *Past Ice Extent Data*

GIA effects at the former glaciated areas in the Northern Hemisphere are relatively well-known benefited by the extensive observational data (Hughes et al., 2016) and networks of GPS measurements (Peltier et al., 2015). In contrast, as described in Chapter 1, Antarctic deglaciation history from the LGM is poorly-constrained due to limited data on past ice extent. Arguably the most widely applied observational constraints on past ice height are from cosmogenic surface exposure dating of the glacially-deposited materials or glacially-eroded bedrock (Bentley et al., 2014, Bentley et al., 2010, Stone et al., 2003) on nunataks to infer the presence of formerly thicker ice. Apart from this, radiocarbon dating of organic remains on biological 'no-ice' indicators like the stomach oil deposits from nesting petrels (Hiller et al., 1988), remains of marine birds and mammals (Hall and Denton, 1999), algal remains in former ice-margin ponds (Bockheim et al., 1989) and pro-glacial lakes (Hall et al., 2001) is also a commonly-used method that provides a minimum age for ice retreating.

In East Antarctica, where there only a few nunataks exists (i.e., cosmogenic surface dating constraints are lacking), most of the observational constraints are from ice core analysis, such as air bubble analysis and isotopic analysis (Mackintosh et al., 2014). However, the atmospheric and isotopic content of ice cores do not have a direct relationship with ice sheet height difference and needs to be interpreted considering multiple processes including the poorly-known GIA effect on ice sheet elevation. As a result, observational evidence from this method is associated with large uncertainties (several hundred meters).

Apart from direct observations on past ice sheet height mentioned above, some indirect glacio-geological observations like ice-rafted debris (IRD; e.g., Weber et al., 2014) and marine geological evidence (e.g., tills) that reflects glacial overriding are also important indicators of AIS discharge history. These indirect constraints are crucial in numerical modelling of AIS deglaciation, such as ice sheet physics modelling (Gomez et al., 2018, Whitehouse et al., 2012a) and climatic modelling (Golledge et al., 2014), which provides insights into AIS ice volume at the LGM and AIS deglaciation history (see details of ice sheet reconstruction in section 2.3).
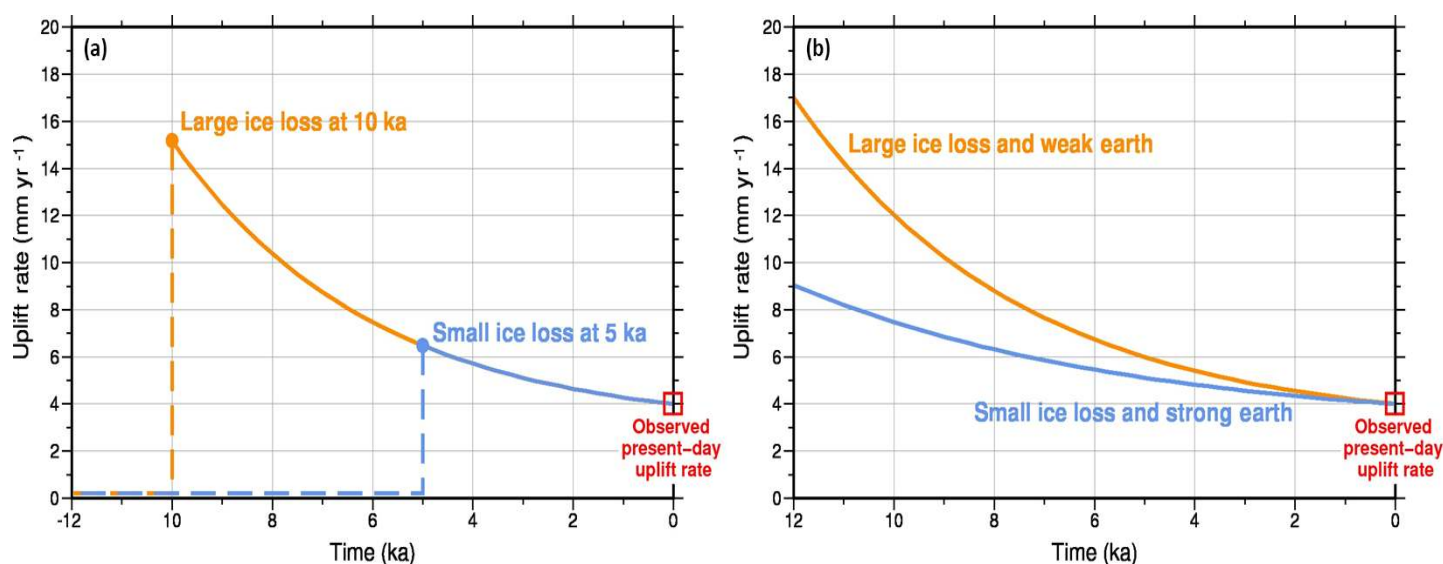
Figure 2.4 An example illustrates the non-uniqueness problem in GIA modelling. (a) Trade-off between the timing and magnitude of ice loading change: large ice loss occurred at early stage (here 10 ka BP) can result in same present-day uplift rate as small ice loss occurred later (here 5 ka BP). (b) Trade-off between ice load history and Earth rheology: large ice loss combined with weak rheology (i.e., low mantle viscosity) can produce same present-day uplift signal as the small ice loss combined with strong rheology (i.e., high mantle viscosity). Figure from (Whitehouse, 2018b).

2.3 Antarctic Ice-Sheet Reconstruction

The sparse and poorly-constrained observational dataset in Antarctica and poorly-constrained Earth rheology result in a strong non-uniqueness problem in Antarctic GIA modelling studies (Purcell, 2017; see Figure 2.4). To overcome this problem, one of the commonly-used methods is to determine the ice history outside the confines of the GIA model. Indirect observations, such as far-field sea level markers (Hibbert et al., 2018, Hibbert et al., 2016), IRD (Weber et al., 2014) and direct glacio-geological constraints on the timing and magnitude of past ice sheet thickness change (see Table 2.1; Anderson et al., 2014, Bentley et al., 2014) can be used to constrain numerical ice model inputs (e.g., De Boer et al., 2014, Golledge et al., 2014, Gomez et al., 2018, Whitehouse et al., 2012a) to reconstruct AIS deglaciation history. Additionally, datasets that are sensitive to both ice history and Earth rheology, such as near-field RSL change (see Figure 3. of Whitehouse et al., 2012b), can also provide powerful constraints on this coupled problem.

At present, three major modelling techniques (which are not necessarily independent) for reconstructing past ice-sheet (not only Antarctica) variation are:

o **Ice-Sheet Dynamic Modelling**: This kind of ice-sheet model is physically-consistent, taking account of physics related to ice-sheet flow, which is useful to predict the response of ice sheets to paleoenvironmental changes and external forcings, such as variations in temperature, ice accumulation rate and relative sea-level change. Glacio-geological evidence can be used to constrain the model parameters (e.g., ice bed sliding parameter) when reconstructing past ice history (e.g., Gowan et al., 2016). The advantage of this method is that it provides valuable information in the area where observational data are lacking like inland of East Antarctica. But the main limitation of this method is that the paleoclimate and ice-sheet boundary conditions, on which these models rely, are poorly constrained. Additionally, there are large uncertainties associated with ice-sheet model parameters such as geothermal heat flux parameter and different ice bed sliding parameters.

o **Climatic Modelling:** This modelling approach incorporates global climatic impact on AIS variation through atmospheric and oceanic forcing effects, which plays a key role in rapid meltwater discharge event, such as meltwater pulse-1A (MWP-1A; a dramatic global sea-level rise event occurred at around 14.6 ka BP). The strength of Antarctic atmospheric and oceanic forcing is investigated by Earth system

modelling constrained by multiple types of paleo-proxy data from different regions worldwide (e.g., intermediate complexity models introduced by Menviel et al., 2011, Weaver et al., 2003), which is used as the input for driving ice-sheet dynamic model independently. This method is a valuable tool to investigate AIS response to transient global climate change, such as rapid warming during MWP-1A (Johnsen, 1999), and ocean warming effects (e.g., Golledge et al., 2014). Whereas, the results of climatic modelling of AIS will not only inherit uncertainties from ice physics modelling mentioned above but also contains large uncertainties associated with the poorly-known Earth's paleoclimatic and paleoceanographic system, such as the trigger points of MWP-1A.

o **GIA Modelling**: GIA modelling approach does not always produce ice sheets that are physically-consistent with ice-sheet flow. For example, Argus et al. (2014) constructed their ice-sheet model ICE-6G_C using a 'GIA only' method by iteratively adjusting ice thickness to satisfy observational constraints (including present-day uplifts rate and near-field RSL records) and do not consider ice physics. For most of East Antarctica where no observational constraints exist, ICE-6G_C predicts no ice thickness change from LGM to present, which is not realistic. In contrast to this simple approach, a more complicated coupled ice sheet – sea level model is being developed, where ice sheets and sea level can vary consistently in space and time and dynamically affect each other (e.g., De Boer et al., 2014, Gomez et al., 2018, 2013). This approach is able to provide insights into GIA effects on ice sheet dynamics (e.g., the GIA stabilising effects during ice sheet retreat), which play an important role in modulating rates of ice-sheet readvance and retreat. However, the major limitations for this approach are poorly-understood parameterisation of Earth rheology and expensive computation (Whitehouse et al., 2019).

2.4 Global Sea-Level Budget and the 'Missing-Ice' Problem

The last deglacial global sea-level budget dictates the relationship between global sea-level rise and mass lost from the ice sheets during the last deglaciation. During glacial cycles of duration ~10^5 yr, the most important contribution to the global sea-level signature is the exchange of mass between ice sheets and oceans (Lambeck et al., 2014), with comparatively small global changes associated with mantle convection and changing ocean temperatures (McKay et al., 2011). Therefore, the sum of ice-equivalent sea-level (ESL) rise from the individual reconstructions of ice sheet models should be approximately equal to the observed

global mean sea level (GMSL) change inferred from far-field sea-level indicators (see section 2.2.1). If so, the global sea-level budget is closed.
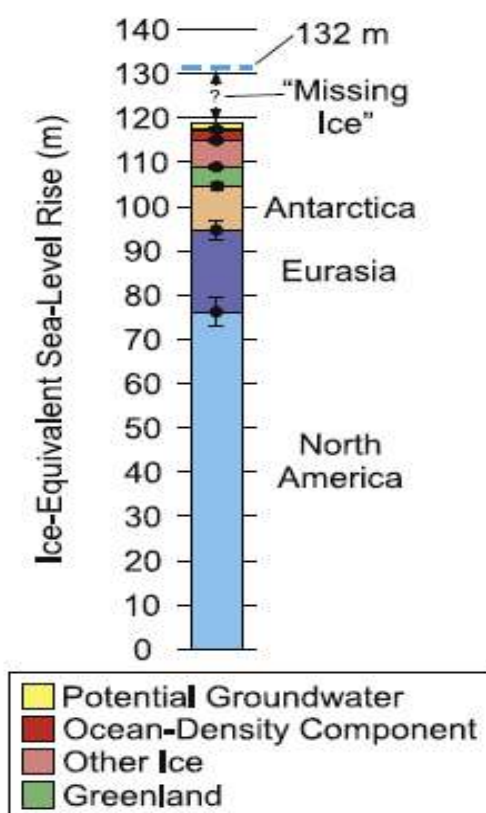

Figure 2.5. A bar graph showing the disparity between observational total sea-level rise since LGM (132 m) and the sea-level equivalent ice stored in continental ice sheets. Different colours indicate different source of global sea-level rise, error bars represent the uncertainty associated with each individual ice sheet contribution estimate. The potential contribution from groundwater and ocean steric effects have also been considered, but around 15 m of global sea level are still unaccounted for. See Table 1 of Simms et al. (2019) for details of each estimate. Figure from (Simms et al., 2019).

However, a long-standing problem is that the sea-level budget is not closed, in other word, the sum of individual ice sheet reconstructions are not necessarily consistent with far-field observational sea-level evidence (Clark and Tarasov, 2014, Simms et al., 2019). Figure 2.5 illustrates the large discrepancy between these two estimates, even after the potential contributions from groundwater and ocean steric expansion have been considered, there are still at least 15 m sea level-equivalent ice sheets at the LGM remain unaccounted for (see Simms et al., 2019 for details of each estimate). This problem is often referred as the 'missing ice' problem (Andrews, 1992).

The reservoir containing this 'missing' ice is a highly-disputed and critical research topic as over 55 years of research has not resulted in a closure (Carlson et al., 2019). Traditionally, the 'missing ice' has been solely attributed to Antarctica (e.g., Bassett et al., 2007, Nakada et al., 2000 which conclude Antarctica can contribute more than 20 m to post-LGM sea-level rise). However, recent ice-sheet modelling studies based on the latest glacio-geological datasets (e.g., De Boer et al., 2017, Gomez et al., 2018, Whitehouse et al.,

2012a) and cosmogenic surface exposure age derived melting rates (Small et al., 2019) suggest a contradictory result that Antarctica can contribute no more than 10 m post-LGM global sea level rise (this could be even smaller if considering the GIA stabilizing effects on ice dynamic). This contradiction led several studies argue for a hypothetical ice sheet at the East Siberian margin (Niessen et al., 2013), though attempts to find evidence for a significant LGM ice sheet in this region (e.g., Barr and Clark, 2011, Brigham-Grette et al., 2003, Jakobsson et al., 2014, Menviel et al., 2011), they have so far been unsuccessful.

Broadly speaking, there are two possible solutions to explain the 'missing ice' problem at LGM: (*i*) There are some large undiscovered ice sheets at LGM like the East Siberian ice sheet mentioned above; (*ii*) The current estimates of ice sheet contributions are underestimated. Before searching for a yet undiscovered ice mass by extensive fieldwork, which is time-consuming and labour-intensive. It is necessary to investigate whether the current estimates of ice sheets contribution are accurate enough. Therefore, the main focus of this study is to use a GIA modelling approach to investigate the Antarctic contribution to post-LGM sea-level rise (which has been proved to be the key of closing the global sea-level budget (Clark and Tarasov, 2014, Simms et al., 2019)), by comparing different AIS models induced global sea-level variation signatures to the far-field sea-level observations during the last deglaciation. This research will be presented in the following order:

1. The selection and treatment of datasets used in this study, including the different AIS models, ice models in other regions and the observational far-field sea-level records.
2. The methodologies used to investigate the last deglacial global sea-level rise patterns associated with different Antarctic ice models.
3. Quantitative analysis of model predictions with observational sea-level records at specific sites for specific periods to determine which Antarctic ice history is most compatible with sea-level observations.
4. Discuss the discrepancies between model predictions and observations and their implications on Antarctic deglaciation history.

Chapter 3 Methods and Data

3.1 Modelling and Analysis Strategy

This section will provide an overall outline of the modelling and analysis strategy before moving into the details of each process. The detailed description of each method and result is presented below following this outline. In general, this research can be divided into the following five steps (but each step is not necessarily independent):

1. **Ice model selection**: This step describes the procedures of selecting Antarctic/other regions ice models used in this study as well as the pre-treatments required before they can be processed by GIA software (such as interpolating ice models onto rectilinear loads from disc loads for IJ05_R2).

2. **Observational sea-level records selection**: It is crucial to select high-quality far-field sea-level records for reconstructing the global ice volume history (step 4) and performing comparative analysis with sea-level predictions. In this study, we incorporate two global far-field sea-level datasets constructed using different underlying philosophies, the details of which will be provided in this step.

3. **Earth parameter searching**: As one of two primary inputs of the GIA model, Earth model plays a vital role in predicting sea-level variation. Once the ice model is defined, a comprehensive earth-model parameter space will be searched by forward modelling to find the optimum Earth parameter for specific ice model. The optimum Earth parameter is then used to correct GIA signal in observed RSL dataset (step 4) and predict global sea-level variation signature (step 5).

4. **Determining the global ice volume history from selected sea-level records**: In order to predict a global sea-level variation pattern, it is essential to ensure the global ice volume is consistent with the sea-level observations. This step will describe in detail of applying GIA corrections to observational sea-level records (which is used to construct the global ice volume history) and how to use a trans-dimensional partition modelling approach to reconstruct the underlying ESL time series with stochastic noise.

5. **Set up global ice model & Close global sea-level budget**: Because of the 'missing ice' problem (see section 2.4), direct combination of regional Antarctic ice model with other regions' ice models cannot

19

produce results consistent with the far-field sea-level observations. To ensure a meaningful sea-level prediction, the 'missing ice' needs to be assigned according to the global ice volume obtained in step 4. The outputs of this step are global sea-level budget consistent ice models associated with each AIS model.

3.2 Ice Model Selection

3.2.1 *Antarctic Ice Models*

In this study, four different last deglacial Antarctic ice models were investigated: (*i*) W12 (Whitehouse et al., 2012a); (*ii*) IJ05_R2 (Ivins et al., 2013); (*iii*) ICE-6G_C (only the Antarctica component will be used in this study; Argus et al., 2014, Peltier et al., 2015); (*iv*) ANT20 (Lambeck et al., 2014).The first three models are currently still the most widely-used models to estimate the Antarctic GIA-induced gravity anomaly and investigate current AIS mass balance from GRACE data (e.g., Shepherd et al., 2018) although they have been published for more than five years. In contrast, the last model was constructed to close the sea-level budget during the last deglaciation rather than a realistic rebound model like first three models, which is used as a reference in this study. The spatial and temporal validity of these four ice models are tested with a newly-formed Antarctic glacio-geological dataset built up by combining two commonly-used datasets: (*i*) A community-based AIS dataset (Bentley et al., 2014); (*ii*) The dataset used to construct W12, ICE-6G_C and IJ05_R2 (data from Whitehouse et al., 2012a), the detail of this dataset is given in Chapter 4.

Although several new AIS models have emerged during the past few years constructed by several novel methodologies (e.g., Golledge et al., 2014, Gomez et al., 2018), they were not included in this study due to significant uncertainties associated with 3-D Earth structure and the paleoceanographic system (also see section 2.3).

o   W12 (Whitehouse et al., 2012a)

The W12 ice model is constructed based on an ice physically-consistent numerical modelling approach (Glimmer ice-sheet model; Rutt et al., 2009), and tuned to fit 62 glacio-geological constraints of past ice thickness, most of which were derived from cosmogenic surface exposure dating of glacially-deposited

materials and glacially-eroded bedrock (Stone et al., 2003, Sugden et al., 2005). The W12 model consists of 4-time slices from 20 ka BP to present and ice thickness was linearly interpolated between time slices. The largest ice volume occurred at 20 ka BP. The evolution of W12 is assumed to be driven by variations in temperature, accumulation rate and near-field RSL, yielding a 9 ± 1.5 m (optimum 8 m) monotonic contribution to global sea-level rise over the last 20 ka with no ice thickness change after 2 ka BP. This ice model was subsequently combined with a GIA model (Whitehouse et al., 2012b) to produce uplift predictions and gravity perturbation. Comparing these outputs to recent GPS observations, they found strong misfits in the Antarctic Peninsula sector due to: (*i*) the W12 model did not account ice thickness change after 2 ka BP (which may dominate the GPS signal in the Antarctic Peninsula, Nield et al., 2012); (*ii*) the optimum Earth model for W12 is an averaged 1-D model that is too viscous for the Antarctic Peninsula (i.e. the relaxation time was too long). The W12a ice model was created to address these two issues by including the ice accumulation during the last 1,000 years. However, the W12a model was considered to be an overcorrection (Wolstencroft et al., 2015). As this change is negligible when investigating far-field sea-level variation, therefore, we do not consider W12a.

The W12 ice model was kindly provided by Pippa Whitehouse (Durham University) from personal communication. It was originally provided in global grids (with the non-Antarctic part of ICE-5G; Peltier, 2004) that comprises 512/256 equally-spaced longitude/latitude values of ice thickness at each time slice. It was then transformed into an ice model format consistent with the GIA software package adopted in this study. Specifically, this format requires equally-spaced (both longitude and latitude) rectilinear grid values of ice thickness difference (with respect to present ice thickness). For this analysis we used an 0.5-degree spatial interval (the input resolution can be higher, like 0.125-degree; or lower, like 1-degree; depending on the original model's resolution). The W12 model was linearly interpolated into 0.5-degree grids using a 2-D linear interpolated algorithm (scipy.interpolate.interp2d function within scipy package; a python library available at: *https://www.scipy.org/*).

o   IJ05_R2 (Ivins et al., 2013)

The IJ05_R2 ice model is a revised version from the original 'IJ05' deglaciation model (Ivins and James, 2005) to incorporate new ice extent constraints (grounding line position data and accumulation data from

ice core) that is largely similar to the dataset used to produce W12. They also used an ice dynamic modelling strategy (Denton, 1991, Denton and Hughes, 2002), which does not take into account ice flow dynamics. Each glacier is represented by one spherical cap (or disc) (455 caps in total; see Figure A1. of Ivins et al., 2013), the radius of each cap remains unchanged with time, ranging from 5.5 to 50 km. Whereas, the height of cap changes with time according to the observational constraints. The IJ05_R2 model's contribution to post-LGM sea-level rise is 7.5 m, which is the smallest post-LGM Antarctic contribution among these four ice models.

The IJ05_R2 model was publicly available as supporting information with their publication (*https://agupubs.onlinelibrary.wiley.com/doi/full/10.1002/jgrb.50208*). Each ice sheet in IJ05_R2 model is represented by a spherical cap rather than the rectilinear grid. In order to make this model compatible with GIA software, we interpolate it into a grid model.

o   ICE-6G_C (Argus et al., 2014, Peltier et al., 2015)

ICE-6G_C is a global deglaciation model refined from its predecessor ICE-5G (Peltier, 2004). In this study, ICE-6G_C only refers to its Antarctic component which was published by Argus et al. (2014) with the accompanying Earth model VM5a. The ICE-6G_C model was developed to fit 62 observations of past ice thickness (same as used in W12), 42 estimated present-day surface uplift rates from GPS sites and near-field RSL records from 12 sites. The strategy for constructing ICE-6G_C is a 'GIA only' method (i.e. only depends on GIA analysis, and does not consider any ice-sheet physics), which iteratively refined the model to fit the observations. The total post-LGM sea-level rise contribution is 13.6 m with no ice melt after 4 ka BP.

The ICE-6G_C model is publicly available, downloaded from W.R. Peltier's website (*http://www.atmosp.physics.utoronto.ca/~peltier/data.php*). It was originally expressed in 1 x 1-degree global grid data, which is compatible with the GIA modelling software.

o   ANT20 (Lambeck et al., 2014)

Unlike other models used in this study that are built for estimating present-day GIA-induced gravity

anomaly (i.e., a rebound model), the ANT20 model was constructed to close the global sea-level budget by assigning the net ESL to Antarctica (i.e. global ESL budget minus the sum of ESL contributions from other individual ice sheets; Lambeck et al., 2014). Put simply this model assigns all 'missing ice' to Antarctica to close the global sea-level budget since based on current knowledge there is nowhere to assign this big amount of 'missing ice' except Antarctica. The ice-sheet geometry of ANT20 was based on a theoretical large continental ice sheet geometry (a quasi-parabolic form, Cuffey and Paterson, 2010). In this model, no attempts have been made to fit any glacio-geological constraints, present-day satellite geodetic measurements or paleoclimatic data. This ice model's ESL contribution is ~28 m, which is much larger than the other three ice models used in this study, indicating a significant offset between global and Antarctic regional constraints on Antarctic contribution to post-LGM global sea level rise.

3.2.2 *Other Regions' Ice Models*

In order to generate global sea-level predictions, we adopted the non-Antarctic component of a global ice-sheet history model developed by the Australian National University (ANU) group, here denoted as ANU global ice model. This model consists of five components: (*i*) the North American Ice Sheet (NA43c model; Lambeck et al., 2017); (*ii*) the Eurasian Ice Sheet (EIS; Lambeck et al., 2006); (*iii*) the Antarctic Ice Sheet (i.e., ANT20 introduced abovel; Lambeck et al., 2014); (*iv*) the British Ice Sheet (BIS; Lambeck, 1993a, 1993b, Lambeck et al., 1996); (*v*) other mountain glaciers (e.g., Tibetan and Patagonia Ice Sheet; Lambeck et al., 2014). The detailed deglaciation history of each part is shown in Figure 3.1. Unlike ICE-6G_C (which is currently the most commonly-used global deglaciation model) that used only one Earth model VM5a to reconstruct (or adjust) global ice history simultaneously, individual components of ANU model were built up separately to match regional GIA observations and global sea-level observations (mainly used for constraining total ice volume). Therefore, the different components of ANU ice model can be treated as independent self-consistent ice-sheet reconstructions (see e.g., Lambeck et al., 2006, Lambeck et al., 2017) that are not biased by the Antarctic deglaciation history (c.f., ICE-6G_C non-Antarctic components were adjusted according to Antarctic model). This indicates, comparing to the commonly-used ICE-6G_C global ice model, ANU ice model is more appropriate to combine with different individual AIS models.
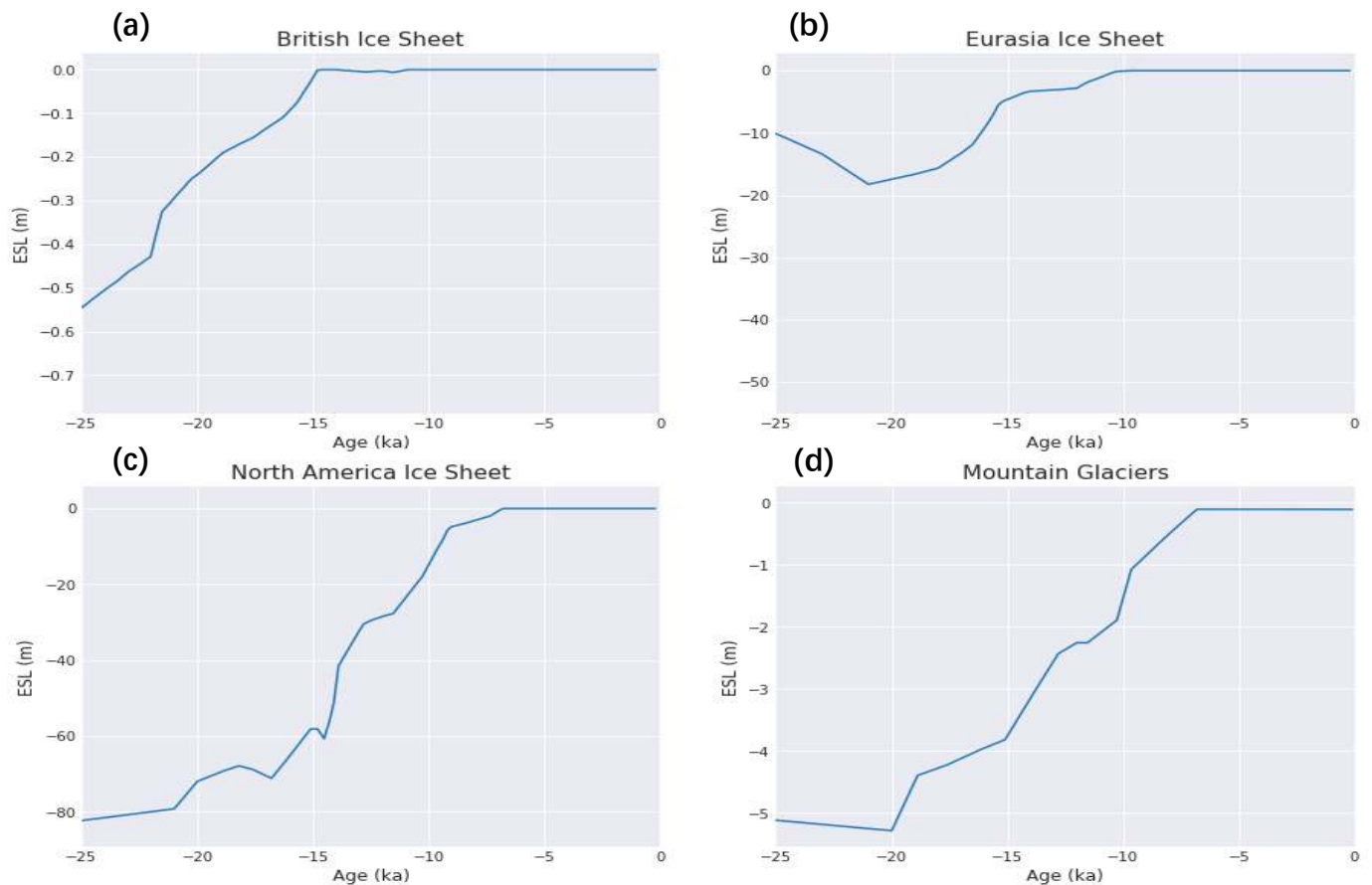
Figure 3.1 Deglaciation history of ANU ice model's non-Antarctic components. (a) British Ice Sheet (b) Eurasia Ice Sheet (c) North American Ice Sheet (d) Other Mountain Glaciers. The ESL contributions are determined by calculating the total ice volume difference between paleo time and present day (do not account the buoyancy), converting ice volume to water volume and divided by present-day ocean area. Note the y-axis of subplots are different in different regions.

3.3 Observational Far-Field Sea-Level Records Selection

Reconstructed paleo far-field sea level data plays a crucial role in GIA modelling for constraining the grounded ice margin or for searching Earth parameters. However, because of the poorly-known ecological spatio-temporal control on paleo sea-level indicators (see section 2.2.1), currently, most of GIA modelling studies are based on a simple normally distributed depth-habitat relationship that cannot fully represent the sophisticated nature of different sea-level indicators. To ensure a more robust result, we adopt two far-field global sea-level datasets (both of which include some key intermediate data from the Caribbean) using strategies introduced in Lambeck et al. (2014) and Hibbert et al. (2016, 2018), here denoted as the L14 and H18 datasets, respectively.

Amongst these two datasets, L14 is well-established for the purpose of constructing last deglacial global ice volume and constraining Earth parameter, which has been adopted in several GIA studies (e.g., Caron et al., 2017). In contrast, H18 is a rather newly-established and incomplete dataset, which has not been used in GIA modelling before. Consequently, we adopt the original L14 dataset with a brief introduction. For H18 dataset, we apply some pre-treatments as well as adding more recent records (e.g., recent Great Barrier Reef dataset from Yokoyama et al., 2018), thus, a more comprehensive description is given relating to these procedures. Considering most of ice models adopted in this study describe the ice history back to 21 ka BP, we only use the RSL records dating up to last 25,000 yr.

3.3.1 *L14 Sea-Level Dataset (Lambeck et al., 2014)*

The L14 far-field sea-level dataset was published (data available at Table S1 of Lambeck et al., 2014) along with their pioneering study on reconstructing global ice volume and sea-level variation since the LGM. This dataset comprises 968 paleo far-field sea-level records from coral and sediment data, dating up to 35 ka BP. The ages of coral and sediment records are either dated by radiocarbon or uranium-series dating, and the paleo sea-level is determined by the equation of (adapted from Lambeck et al., 2014 using the notation of this study):

$$S(\omega, t) = \xi(\omega, t) - \frac{\delta \xi_d}{2} - \delta \xi_{tide} \quad [3.1]$$

where $S(\omega, t)$ is paleo RSL with respect to present at specific location ω on specific time t; $\xi(\omega, t)$ represents the current elevation of RSL record. $\delta \xi_d$ denotes the species and environment dependent growth depth range of each record (assuming the modern range is representative of the past growth range and the growth position is normally distributed) and $\delta \xi_{tide}$ is the mean-low-water-spring level with respect to mean sea level (assuming there is no significant change in paleo tides). All sea-level records in L14 dataset have been carefully assessed (records with large uncertainties have been excluded), appropriate tectonic correction has been applied to the records collected from tectonically activate region (e.g., Barbados, Huon Peninsula and Tahiti).

3.3.2 *H18 Sea-Level Dataset (Hibbert et al., 2016, 2018)*

The H18 datast is a publicly available *(https://figshare.com/articles/Database_of_biological_and_ geomorphological _sea_level_markers_from_the_Last_Glacial_Maximum_to_the_present_Hibbet_et_al_2018_Scientific_Data_/5367880*) global far-field biological and geomorphological sea-level dataset published with a recent study of Hibbert et al. (2018) based on the methodology introduced in Hibbert et al. (2016). Figure 3.2 gives a simplified schema of data processing within this dataset, and a brief outline of each essential component of this method is given below.
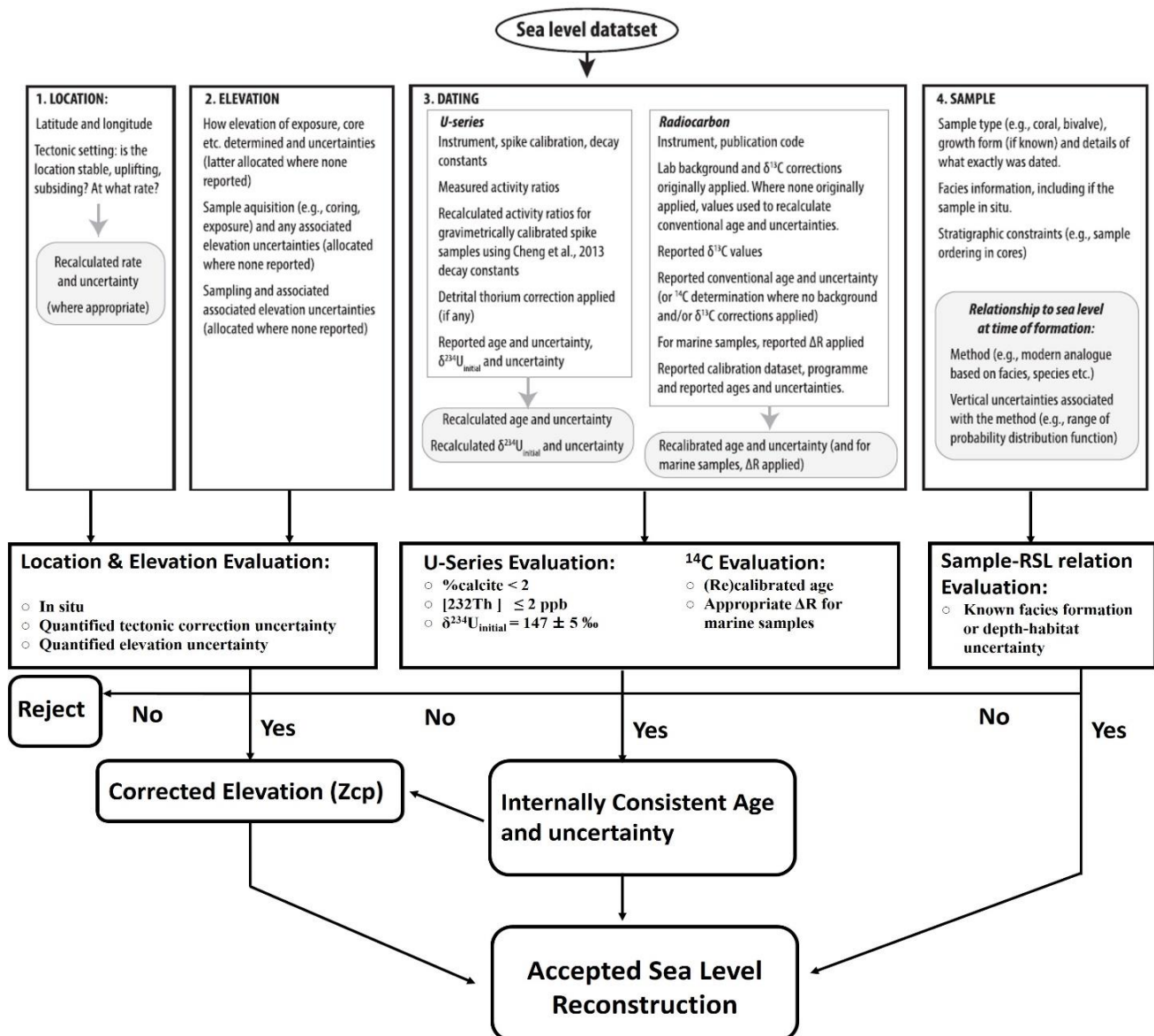

Figure 3.2 Simplified schema of the deglacial sea level database giving an overview of data acquisition and processing. The numbered boxes are four essential components needed to reconstruct probability of sea level (P_{RSL}). Grey boxes indicate additional processing of data from original publications and new outputs. The middle line of box is the screens applied in this study. Figure adapted from Hibbert et al. (2018) Figure 2.

o   **Data Source**

All original data of H18 dataset is obtained from peer-reviewed papers and books. It incorporates most of important far-field RSL dataset, an overview of age and geographical distribution of the original H18 is shown in Figure 2.3. However, it does not include all records from Tahiti (Bard et al., 2010, Deschamps et al., 2012) and Barbados (Fairbanks et al., 2005, Peltier and Fairbanks, 2006), which are considered to be the principle coral records for the late glacial period (i.e., ~25 – 15 ka BP). Additionally, one newly published high quality dataset from Noggin Pass and Hydrographer's Passage, Great Barrier Reef (GBR; Yokoyama et al., 2018) is also not included in H18. In order to provide better resolution for constraining global ice volume, we create a new H18 dataset by encompassing these records (still refer as H18).

o   **Tectonic Setting & Sample Elevation Uncertainty**

For the records from tectonically active region, the uplift/subsidence rates are constrained either by independent evidences (e.g., for Tahiti and Mururoa Atoll) or maximum elevation of fossil coral terrace corresponding to the Last Interglacial (MIS 5e, ~128-116 ka). The detailed uplift/subsidence rates are given in Table 2 of Hibbert et al. (2018). H18 has also considered the uncertainty associated with elevation in terms of measurement uncertainty and sampling uncertainty (e.g., core stretching or shortening errors) by either adopt the information within original publication or allocate a method-appropriate uncertainty (see Table 3 of Hibbert et al. (2018)) to each record. The output of this step is tectonically corrected position (Zcp) for each record with appropriate uncertainty associated with paleo elevation.

o   **Sample Age and Uncertainty**

All radiocarbon ages have been recalibrated using 'IntCal13' and 'Marine 13' calibration curve (Reimer et al., 2013) using Oxcal 4.2 program (Reimer et al., 2009). U-series ages were recalculated where necessary, assuming a closed system with the latest decay constant (Cheng et al., 2013). All ages are then adjusted to one common datum (i.e., ka BP).

o   **Sample Information and Context**

Two different approaches are used to represent the relationship between the sample and paleo sea level at

the time of its formation (i.e., the 'indicative meaning' which describes the range of elevations, with respect to a specified tidal datum, that a particular indicator forms; Shennan, 1986, Van de Plassche, 2013). A first approach is using a specific probability distribution for each coral specie, obtained from empirically-derived modern depth-habitat distribution of each taxon. The second assumes a uniform distribution within the upper and lower limits of formation range for each sea-level indicator due to the lack of information as to the most likely depth or elevation. Examples of these two approaches are shown in Figure 3.3.
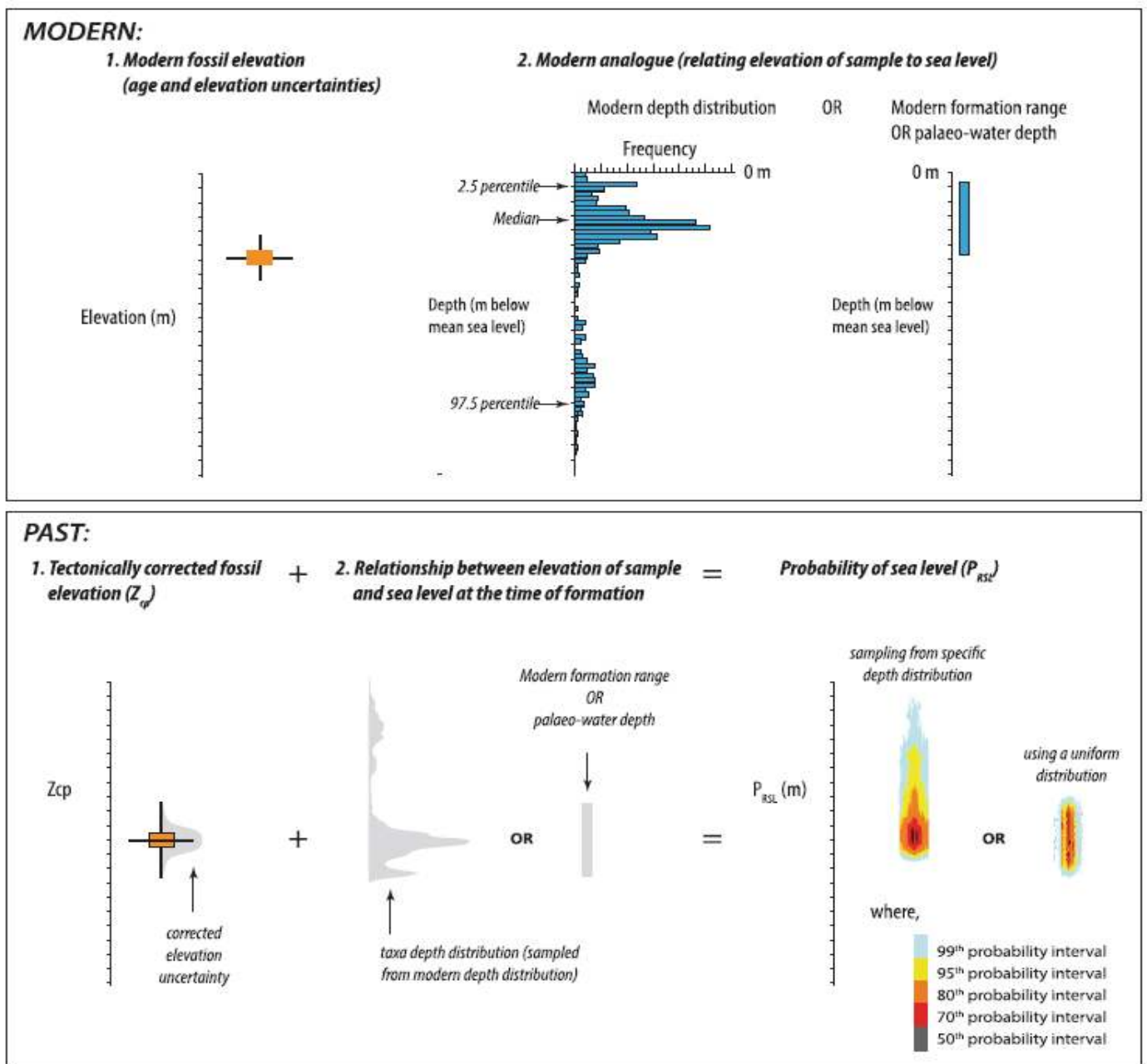

Figure 3.3 Schematic of relationship between, and uncertainty propagation for, the corrected coral position (Zcp) and the probability of sea level (P$_{RSL}$). Figure from (Hibbert et al., 2018).

o **Data Reliability Screen & Progradation Treatment**

To ensure the quality of each sample, we further apply several reliability screens to remove the unqualified records, which are given in the middle panel of Figure 3.2. Another complication is the problem associated with lateral reef progradation (Woodroffe and Webster, 2014) results from the reef that have adopted catch-up mode (shallow specie coral is 'catching up' with the sea-level rise, hence, which will be found below its normal living depth) replaced by deep tolerant species up core in the same core. But with the reef migrates upslope to a new position, the crest/shallower species will be found again, which forms the 'replicate' group in H18 dataset. We treat this problem by averaging each replicate sample group's age and *Zcp* using a weighted average method, which is then processed using the same approach introduced below.

o **Reconstructed Probability of Sea Level (P$_{RSL}$)**

Instead of assuming a normally distributed growth depth like L14 ($\delta\xi_d/2$ in equation [3.1]), H18 uses a Monte-Carlo approach of 350,000 simulations to extract a probability maximum sea level (P$_{RSL}$) associated with each sea-level indicator corrected position (*Zcp*) and depth-habitat relationship with 1-, 2-, 3- sigma uncertainties (68%, 95%, 99% probability interval). A schematic of this procedure is shown in the bottom panel of Figure 3.3, two different representative relationships between sample and sea level height result in different representations of uncertainty range (e.g., a typical 'bullseye' uncertainty range for coral record, see the bottom panel of Figure 3.3).

3.4 Earth Model Searching

Given the global ice model (either the ANU ice model or ice model defined in step 3.6), the Earth-model parameters (including the thickness of elastic lithosphere, and upper and lower mantle viscosity) is determined by forward modelling through a suite of Earth-parameter space (~4500 Earth models, a full list of tested Earth-model parameters is given in Table 3.1) to fit the selected observed far-field RSL dataset (i.e., L14 or H18). The goodness of fit for each Earth model is estimated using a bins-analysis method that estimates the variance (i.e., misfit) within each bin of time slice:

$$\Psi_k^2 = \frac{1}{N} \sum_{n\in[n_{min},n_{max}]} \sqrt{\frac{L_{n,n+0.5}}{L_{Min}}} \times \frac{1}{L_{n,n+0.5}} \sum_{m=1}^{M} \left[\left(H_n^{n+0.5}(t) \frac{S_{obs}^m(\omega,t) - S_{pred}^m(\omega,t)}{\sigma^m} \right)^2 \right] \quad [3.2]$$

where $H_n^{n+0.5}(t)$ is the Heaviside step function, given by:

$$H_n^{n+0.5}(t) = \begin{cases} 1, & t \in [n, n+0.5) \\ 0, & t \notin [n, n+0.5) \end{cases} \quad [3.3]$$

Ψ_k^2 is the variance value for k-th Earth model (k=1…K); each record $S_{obs}^m(\omega, t)$ is assigned into a specific time bin $[n, n+0.5)$ based on their age t; N indicates the number of bins (n=n_{min}, n_{min} + 0.5, n_{min} + 1…n_{max}); $L_{n,n+0.5}$ is the sample size of the records within the time interval from n to n+0.5 ka; L_{Min} is the overall minimum sample size; S_{obs}^m and S_{pred}^m t are the m-th observed/predicted (m=1…M) RSL values; σ^m means one standard deviation (SD) error of m-th observation (for H18 dataset where error is asymmetric, we use an averaged one SD error). The advantage of this method, compared to a commonly-used variance function, is it avoids the final variance value being over-dependent on specific data that has extensive sample size (e.g., the Holocene sample size, ~200, compared to late glacial period sample size, ~20) by balancing the variance for each 0.5 ka time. The optimum Earth model is defined as the Earth model that produces the lowest variance value, which is used to calculate GIA signal and correct the observed RSL dataset (section 3.5.1) or predict last deglacial global sea-level rise signatures.
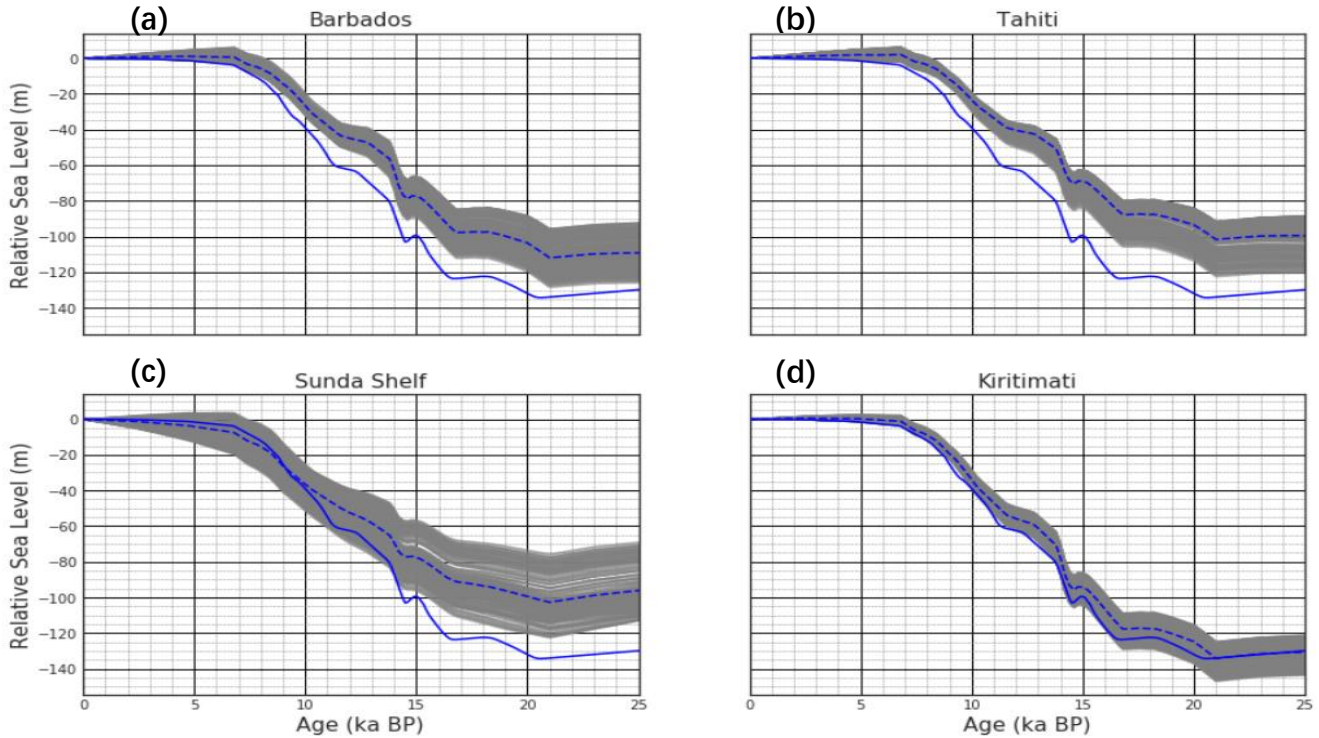

Figure 3.4 An example of Earth model impacts on RSL prediction and GIA signal calculation based on ANU ice model. The grey lines indicate RSL predictions for a set of 254 different Earth parameters (lithosphere thickness, upper and lower mantle viscosity). The blue dashed and solid lines represent the mean curve of 254 predicted RSL curve and reference eustatic curves estimated by (Lambeck et al., 2014). The sites' names are shown as the subtitle of each plot.

The spatio-temporal-varying GIA correction uncertainty is calculated by exploring 254 Earth parameters' impact on the magnitude of GIA signal $S_{k,GIA}(\omega, t)$ in equation [3.2], which assumed to be the Gaussian. We do not consider the uncertainty associated with the ice model because of the 'missing ice' problem and the poorly-known last deglaciation global ice history. An example of the GIA impacts for four far-field locations is shown in Figure 3.4 where significant sensitivity to Earth parameters can be found at all sites, which are associated with different effects described within GIA model (e.g., Barbados is sensitive to the peripheral bulge dynamic, Tahiti and Sunda Shelf are more sensitive to ocean syphoning and continental levering effects). The GIA correction uncertainties are then introduced into the total RSL vertical uncertainties when estimating the ESL function (introduced in section 3.5.1 below) by adding which in quadrature to the uncertainties of paleo sea-level height.

Table 3.1 List of Tested Earth Models

Lithospheric Thickness (km)	Upper-Mantle Viscosity (10^{21} Pa s)	Lower-Mantle Viscosity (10^{21} Pa s)
40, 50, 60, 65, 72, 80, 90, 95, 100, 105, 110, 120, 130, 140	0.05, 0.07, 0.085 0.1, 0.125, 0.15, 0.2, 0.25, 0.3, 0.35, 0.4, 0.45, 0.475, 0.5, 0.525, 0.55, 0.575, 0.6, 0.625, 0.65, 0.7 1, 1.5, 3	1, 1.5, 2, 3, 5, 7 10, 15, 20, 30, 40, 50, 70, 100

3.5 Determining Global Ice Volume History

3.5.1 *Determining ESL Signal from Observational RSL Records*

In principle, the observed relative sea level $S(\omega, t)$ at location ω and time t can be written as:

$$S(\omega, t) = ESL(t) + S_{GIA}(\omega, t) \quad [3.4]$$

where $ESL(t)$ is the ESL signal that represents the global ice volume (or ice-volume equivalent sea level; ESL) at specific time t; $S_{GIA}(\omega, t)$ indicates all GIA-induced spatio-temporal relative sea-level change

signals (see section 2.1.2), including the gravitationally consistent geoid variation, solid Earth deformation corresponds to changing surface load and time-varying ocean area. Hence, a series of underlying observed global ice volume history data points (i.e., $ESL(t)$ in equation [3.4]) can be obtained through using GIA modelling approach to remove the GIA signal $S_{GIA}(\omega, t)$ from the observed RSL data.

For L14 dataset, the GIA signal $S_{GIA}(\omega, t)$ and global ESL function $ESL(t)$ are estimated by replicating the original methodologies introduced in Lambeck et al. (2014). Based on this study, we calculate the $S_{GIA}(\omega, t)$ and $ESL(t)$ for our newly-formed H18 dataset through the following an adapted iterative procedures: (*i*) Start with ANU ice model, invert H18 dataset for Earth rheology parameter; (*ii*) Using optimum Earth model obtained in step *i* to correct the GIA signal for H18 dataset; (*iii*) Reconstruct the underlying ESL function by a trans-dimensional partition modelling approach (described below), yielding a different global ice volume history; (*iv*) Distribute the ice mass/volume difference to either AIS or North America Ice Sheet (NAIS) by tuning the ANT20/NA43c model for a better fit of H18 dataset (denoted as Antarctic/North American scenarios for late LGM sea-level drop) guided by published information, which forms a new AIS/NAIS model for H18 dataset; (*v*) Repeat step *i-iv* but start with the new ice model obtained in step *iv* until converge (*vi)* Combine the final AIS/NAIS model (denoted as ANT20_H18/NA43c_H18) with its optimum Earth model to separate ESL signal for H18 dataset. For the first iteration, we adopt a conservative data-quality criterion of $\left| (S_{obs} - S_{pred})/\sigma_{obs} \right| > 50$ to filter out the possible outliers for a further examination. Only the data that causes noisy signal in data interpolation (described in section 3.5.3) or incompatible with other close observations (close in both location and time) are they rejected. We do not consider a further sophisticated approach such as incorporating reef morphology or sediment stratigraphy information, which may increase the overall quality of H18 dataset and its corresponding ice model since it is currently outside of the scope of this study. In total, 120 records out of 1594 observations have been exclude.

3.5.2 *GIA Modelling Software*

All GIA modelling presented in this study was performed with the *CALSEA* software package developed by the ANU group (Lambeck et al., 2003, Purcell et al., 2016). This software package obtains solutions to the sea-level equation of Farrell and Clark (1976) and includes subsequent refinements of time-varying

ocean function (Johnston, 1993, Lambeck et al., 2003) and rotational feedback (Mitrovica and Wahr, 2011, Mitrovica et al., 2005). For the GIA model used in this study, the Earth is represented by a spherically symmetric, self-gravitating Maxwell body comprising three layers: an elastic lithosphere, and a uniform viscosity upper and lower mantle extending to 670 km and from 670 km to the core-mantle boundary, respectively. The elastic and density structure of the Earth is derived from the seismic study of Dziewonski and Anderson (1981). The ice sheet grounding line (i.e., the location where ice starts to float, which determines the boundary of ice loading transitions to water loading in GIA modelling) is determined by nine iterations of governing sea-level equation (see section 2.1.2) to provide a sub-centimetre converge at all points on the globe.

While performing GIA modelling, the following assumptions are made:

1. The total mass of water in the Earth system is conserved through time.
2. Water is contained entirely in the ice sheets and ocean basins (i.e., a closed sea-level budget that do not consider the water exchange between groundwater and ocean in GIA modelling).
3. The exchange of water load takes place entirely between the ice sheets and ocean basins and complete instantaneously.
4. No other non-GIA-related contributions to sea-level change, such as mantle dynamic topography, tectonic signatures, sedimentation and ocean steric expansion (these effects were considered when reconstructing the observed RSL dataset on different time-scales; e.g., mantle dynamic topography is important on $\sim 10^6$ yr time scale but less important on millennial time scale).

3.5.3 *Reconstructing Underlying Time Series*

A time-series of the ESL signal with stochastic noise for H18 dataset were obtained by applying the GIA correction to observed RSL records described in section 3.5.1. In order to reconstruct the underlying ESL signal within this noisy time series, we use a recently published Bayesian trans-dimensional partition (i.e., changepoint) modelling approach that allows arbitrary errors in both x (i.e., Age) and y (i.e., ESL) variables using a newly derived integrated likelihood function introduced in Sambridge (2016). This approach solves the inverse problem using the reversible jump Markov chain Monte Carlo (McMC) algorithm to generate an ensemble of solutions with variable numbers of partitions to sample the Bayesian posterior probability

density function (PDF) defined by the product of a likelihood and a prior PDF (Denison et al., 2002, Gallagher et al., 2011). At each step of the Markov chain, a perturbation is made to the current curve by randomly choosing the following perturbation classes:

1. A 'Birth' Step: Create an additional control node (i.e., add one more partition) randomly
2. A 'Death' Step: Delete a random interior control node
3. Randomly move the x coordinate of a chosen control node
4. Randomly move the y coordinate of a chosen control node

For each perturbation class, the proposed model will be accepted/rejected with a probability according to the Metropolis-Hasting rule (Metropolis et al., 1953, Hastings, 1970, see details in Gallagher et al., 2009, Sambridge et al., 2006). This largely avoids the need to impose artificial constraints on model complexity (e.g., only a maximum number of partitions is required). The underlying 'denoised' ESL time series and its gradient are then obtained as the mean of the ensembles collected from the second half of 10^6 runs of Markov chain. The uncertainty estimates are obtained from the probability density function for the entire time signal as well as from the location of the partitions, which indicate abrupt changes in gradient.

Compared with the 'y error only' approach used in Lambeck et al. (2014), this approach provides several benefits: (*i*) Avoid some extraneously complex details (see Figure 7 of Sambridge 2016); (*ii*) The curve is better constrained with lower uncertainty (see Figure 8 of Sambridge 2016); (*iii*) Better detection of data discontinuities.

3.6 Global Ice Model Set Up

The problem of setting up a global ice model consistent with the last deglacial global sea-level budget is greatly complicated by determining where to assign the 'missing ice'. Because the deglaciation history of Eurasia Ice Sheet is relatively well-constrained (Simms et al., 2019) and mountain glaciers are too small to balance the 'missing ice', the most possible regions for distributing 'missing ice' are North America and Antarctica (Lambeck et al., 2014). Since key content of this study is the AIS models' sea-level signatures, our strategy is to assign the required ice volume to NAIS by proportionally scaling the NAIS model within

ice-sheet boundary in each time slice to fit the observed global ice volume function either from the H18 dataset (which is estimated in section 3.5) or the L14 dataset (which is given in Lambeck et al. 2014). Because this is not an ice-physically consistent method, the rescaled NAIS model can only use to produce far-field sea-level predictions, which is not sensitive to the near-field ice-sheet geometry, rather than a realistic rebound model or a glacio-geological consistent model.

As the volume of 'missing ice' is time-dependent, in order to ensure the global ice volume represented in the global ice-sheet model constantly equals the global ice volume function estimated from observed sea-level records (i.e., a persistent closed sea-level budget), the NAIS ice model needs to be scaled using a time-varying rescaling factor $\beta_1(t)$ given by:

$$\beta_1(t) = \frac{\text{ESL}_{obs}(t) - \text{ESL}_{other}(t)}{\text{ESL}_{NAIS}(t)} \quad [3.5]$$

thus, the tuned NAIS ice volume function $\text{TI}_{NAIS}(\omega, t)$ is:

$$\text{TI}_{NAIS}(\omega, t) = I_{NAIS}(\omega, t) \times \beta_1(t) \quad [3.6]$$

where $\text{ESL}_{obs}(t)$ is observed ESL function derived from sea-level observations, $\text{ESL}_{other}(t)$ is the ESL function of all other regions' ice models (i.e., AIS, EIS, BIS, other mountain glaciers); $I_{NAIS}(\omega, t)$ is the original NAIS ice function introduced in Lambeck et al. (2017). The most prominent problem of this approach is that after the cease of NAIS deglaciation at mid-Holocene (~7.5 ka BP), there is nowhere to assign the ~4 m of 'missing ice'. This can greatly contaminate the RSL prediction result due to the sudden collapse of tuned NAIS model, accordingly, we only calculate the variance of each ice model between 21 to 8 ka BP.

Chapter 4 Results and Analysis

4.1 Antarctic Ice Models

Figure 4.2 and Figure S2 gives the goodness of fit for each selected AIS model at different time slices compared to the glacio-geological dataset (including marine geological/geophysical data on paleo grounded ice extent and terrestrial evidence of former ice sheet height), the location of which is shown in Figure 4.1. Because of the temporally sparse observational evidences in Antarctica, all observational constraints are assigned to four different time slices (20, 15, 10, 5 ka BP) with no consideration of age uncertainties. A positive misfit indicates thicker ice predicted by the model, and a negative value indicates thinner ice. When the observational data is a range constraint with upper and lower limits of ice height difference (IHD; the ice height difference between paleo and present ice sheets), if the prediction is outside range, the misfit is defined as the difference between the prediction and closer boundary constraint (i.e., upper or lower limit that closer to prediction). If the model prediction at a data site satisfies the limiting data (i.e., upper/lower limit), a zero misfit is assumed. Each model was plotted along with two possible scenarios of reconstructed
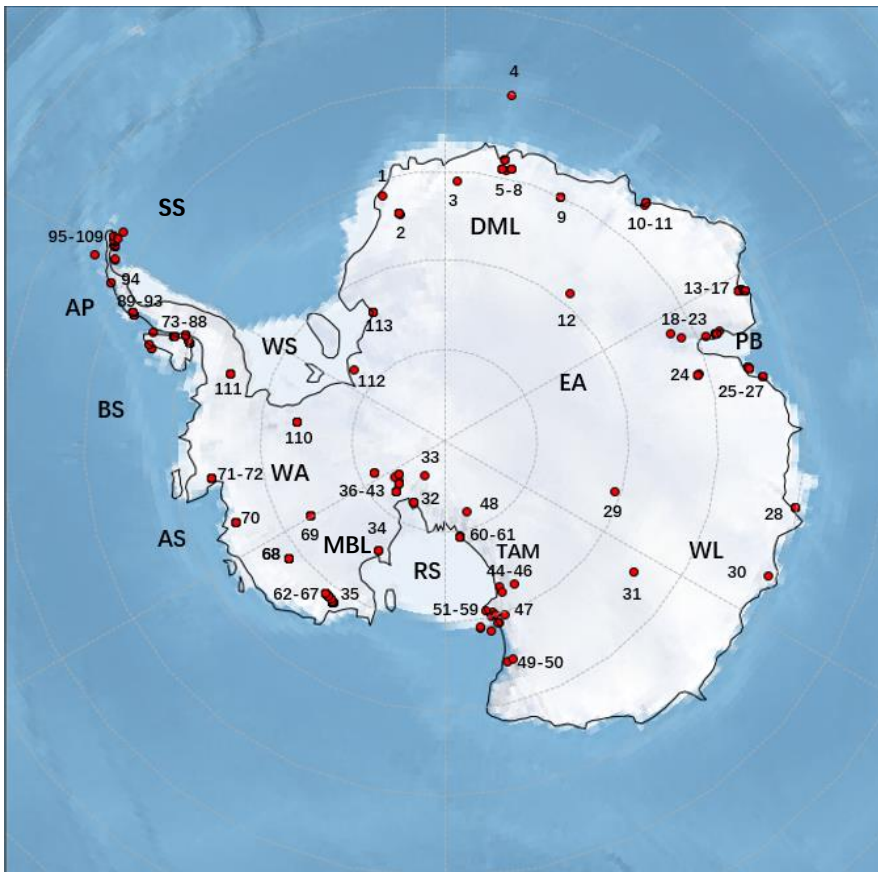

Figure 4.1 Map of Antarctica, showing present day grounding line and observational site location. Numbers refer to the observational site location used in this study (data from Bentley et al., 2014, Whitehouse et al., 2012a). DML = Dronning Maud Land; EA = East Antarctica; PB = Prydz Bay; WL = Wikes Land; TAM = Transantarctic Mountains; RS = Ross Sea; WA = West Antarctica, MBL = Marie Byrd Land, AS = Amundsen Sea; BS = Bellingshausen Sea; AP = Antarctic Peninsula; WS = Weddell Sea, SS = Scotia Sea.
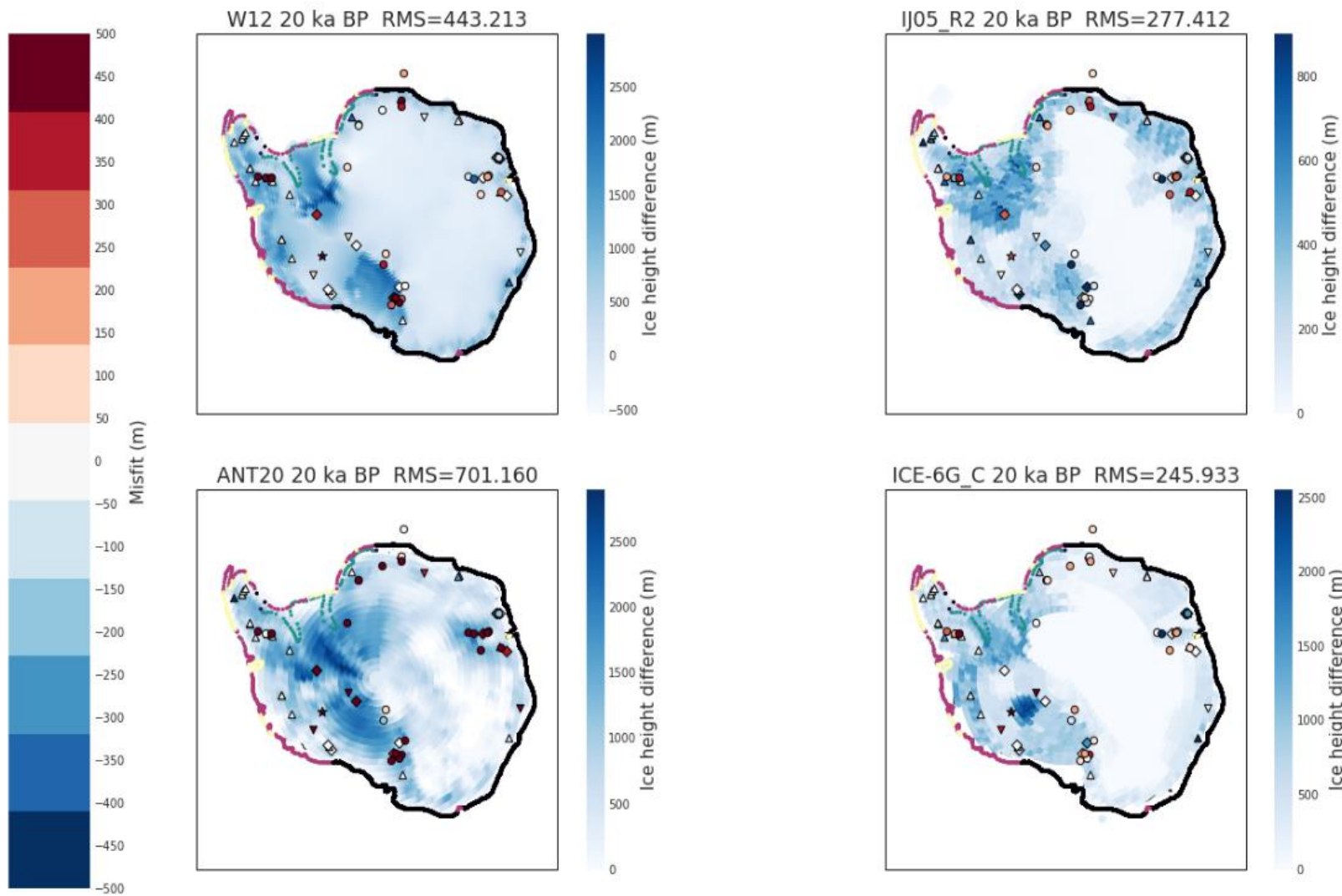
Figure 4.2 Comparison of the four ice models with observational constraints. The subtitle gives the model name, time slice and total root mean square (RMS) value. Figure background is the model's ice height difference (IHD, note the different models have different colour-bar scale). The points on the margins are the reconstructed AIS ice grounding line at 20 ka BP, note that there are two possible scenarios for Weddell Sea (shown in purple and blue-green), and the level of uncertainty of grounding line positions is indicated by the following colours: black (speculative), yellow (measured), purple and green (inferred). Points shown above background are observational data corresponding to site number (Figure 3.). Circles are data sites with absolute (or close to absolute) values, up and down-triangles are minimum and maximum limiting data respectively, rhombus are range data (i.e., contains upper and lower limits) and stars are approximate value. If model reconstructions at a data site satisfies one of these limiting data then a zero misfit is assumed. Positive misfit means model value is larger than observation (i.e., red indicates that model predicted ice height difference are too thick).

paleo ice grounding line position based on two plausible geological interpretations (Bentley et al., 2014).

4.1.1 *Ice Models Configuration at LGM*

The configuration of the four AIS models shows large variability in terms of locality and magnitude of ice melt across the different solutions. For the W12 and IJ05_R2 models, the majority of ice loss occurred in coastal areas of the Weddell Sea (WS) and Ross Sea (RS) sectors. The ANT20 model also has major ice loss in these two sectors but most of the melt occurred inland. ICE-6G_C has a rather distinctive ice-sheet configuration, where the largest ice melt does not occur in the marine-grounded area. Instead, ICE-6G_C predicts the most ice melt occurred at Marie Byrd Land where large GIA uplift rate is currently observed (Argus et al., 2014, Martín-Español et al., 2016), with no ice thickness variation at inland East Antarctica where there are no observational IHD records. ANT20 and IJ05_R2 have significant ice loss in Prydz Bay in East Antarctica with little ice melt near the Bellingshausen Sea and the Amundsen Sea. However, W12 and ICE6G_C present an opposite trend, with most of the ice loss occurring at the Bellingshausen Sea.

Around much of Antarctica where the grounding line was close to the continental shelf break at LGM, all AIS models show good agreement with the geologically based grounding line reconstruction. The most contradictory spatial extent implied by two scenarios of ice grounding line occurs in the Weddell Sea embayment where whether the grounding line extended to the continental shelf is contentious due to the poorly-constrained and debated retreat history (Hillenbrand et al., 2014; Figure 4.2). The W12 model is consistent with the scenario that grounding line did not extend to the continental shelf but the northern margin of Berkner Island at the LGM (blue-green line in Figure 4.2), which is consistent with the glaciological flowline modelling results (Whitehouse et al., 2017). The other three models, however, agree with the more extensive grounding line scenario (purple and yellow line; Bentley et al., 2014) that the ice sheet had retreated from the shelf edge after the LGM (Figure 4.2), which is more consistent with marine geological data (Hillenbrand et al., 2014).

4.1.2 *Models Fit to Glacio-Geological Dataset*

In Figure 4.2 and Figure S2 we plot the spatial IHD misfit for each AIS model within each subplot. The overall goodness of fit of each AIS model is represented by root mean square (RMS) value estimated by:

$$RMS = \sqrt{\frac{1}{M} \sum_{m=1}^{M} \left(IHD_{predicted}^{m} - IHD_{observed}^{m} \right)^2} \qquad [4.1]$$

where $IHD_{predicted}^m$ and $IHD_{observed}^m$ indicate predicted and observed IHD value for mth (m=1…M) record. The RMS values for each time slice are shown in the subtitle of each plot in Figures 4.2 and S2, and the RMS value for each Antarctic sector (based on modern Antarctic drainage system; Zwally et al., 2012) in different time slices are shown in Figure 4.3.

As the ANT20 model does not attempt to fit the observational constraints, it has the largest averaged RMS value of 573 over the four-time slices compared to the other three models (272 for W12, 237 for IJ05_R2 and 214 for ICE-6G_C) constrained by observations. Large misfits in the ANT20 model are found in the WS and RS, where ANT20 predicts several hundred metres thicker ice sheets at the LGM. The other three models show overall good agreements with the observational constraints, the only significant misfit is W12 predicts a much thicker ice sheet in the Antarctic Peninsula sector at the LGM, which largely results from its 20-km resolution which cannot resolve the bedrock topography or ice-sheet flow trajectories in this region.
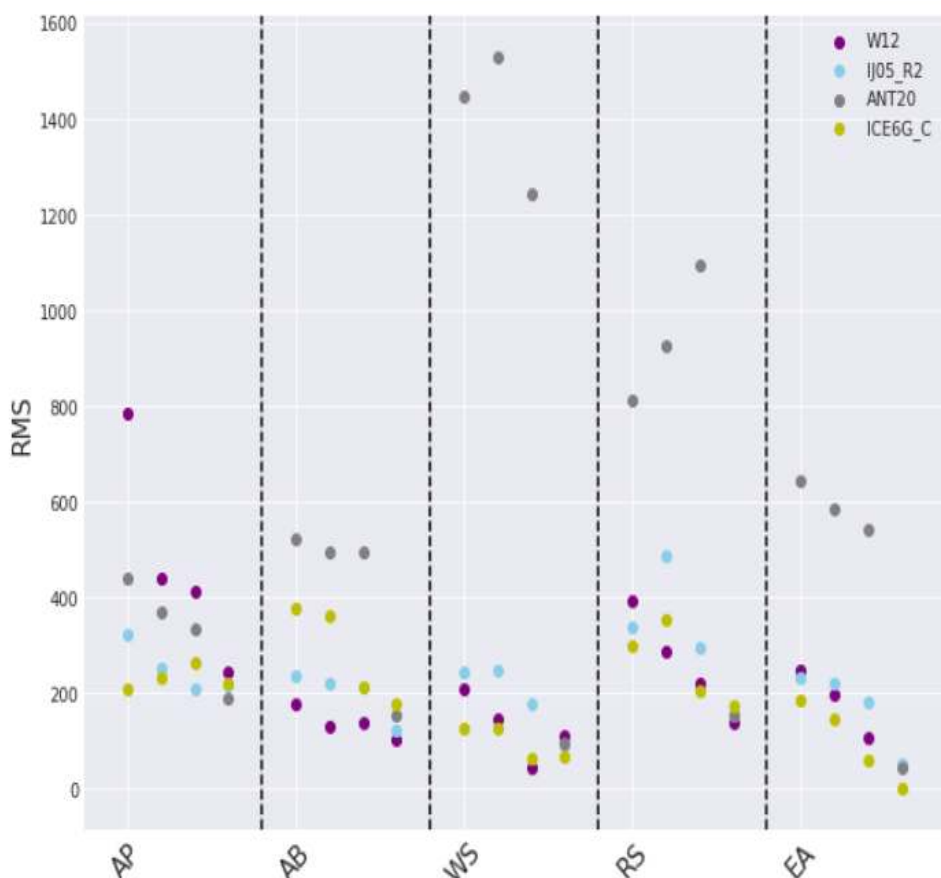

Figure 4.3 Overall model misfit (root mean square, RMS) for different Antarctic sectors at four time slices. The name of sector is shown on the bottom of the plot, with the different sectors are divided by black dash lines. For each sector, points from left to right refer to RMS result at 20, 15, 10, 5 ka BP time slices respectively. The sectors are: AP = Antarctic Peninsula, AB = Amundsen and Bellingshausen Sea, WS = Weddell Sea, RS = Ross Sea, EA= East Antarctica.

4.1.3 *Ice Models Deglaciation Histories*

Figure 4.4 illustrates the eustatic sea level change due to the four deglaciation histories of AIS models adopted in this study, which are slightly different compared to the original publications since floating ice volume is not included. The ANT20 model suggests a much larger Antarctic contribution to post-LGM sea-level rise of ~28 m compared to the other three ice models constrained by glacio-geological evidence, which suggests an at least ~15 m 'missing ice' imposed by the different AIS models at the LGM. Apart from that, there are large variabilities regarding the timing and magnitude of AIS melting across different reconstructions. During the late glacial period from 20 to 15 ka BP, only W12 shows a high melting rate of ~1 m/ka, which is incompatible with the nearly zero ice melt predicted by ANT20/ICE-6G_C and a slow ice gain in IJ05_R2. W12 has a smooth and gradual profile of deglaciation, whereas the other three models all contain a period of rapid ice-sheet melt. ICE-6G_C predicts large ice losses corresponding to two major meltwater pulse events occurring at 11.5 and 14.5 ka BP (Meltwater Pulse 1B and 1A; Fairbanks, 1989), whereas, the most prominent episode of ice melting for ANT20 and IJ05_R2 occurred much later at 9 and 7.5 ka BP respectively, coinciding with Meltwater Pulse 1C (Liu et al., 2004) and catastrophic rise event 3 (Blanchon and Shaw, 1995).
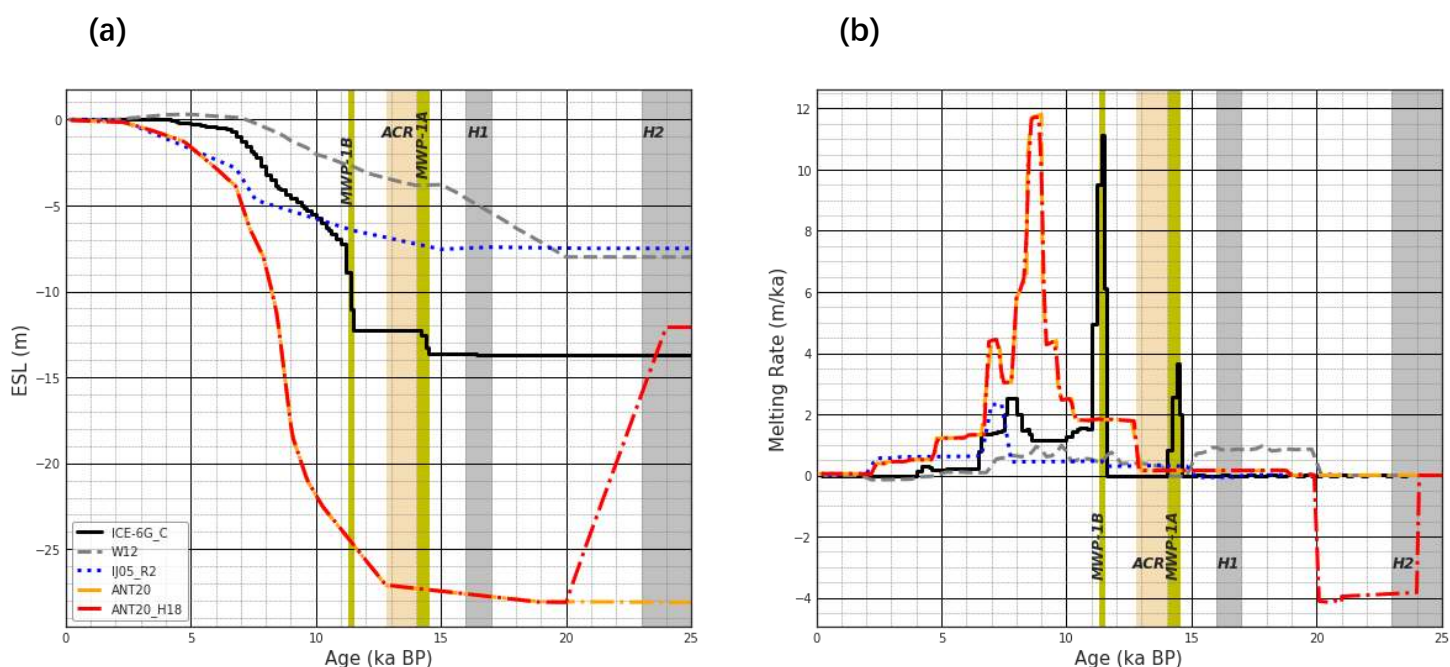

Figure 4.4. Comparison of AIS models' deglaciation history: ICE6G_C (black; Argus et al., 2014), W12 (grey; Whitehouse et al., 2012a), IJ05_R2 (blue; Ivins et al., 2013), ANT20/ANT20_H18 (orange/red; Lambeck et al., 2014). (a) Antarctic contribution to post-LGM global sea-level rise. (b) Antarctic ice melting rate (this study), the green vertical bar is the timing of MWP-1A and MWP-1B, grey bars are Heinrich Events H1, H2, yellow bar stands for Antarctic Cold Reversal (Parrenin et al., 2007). Note the results presents here are slightly different compared to original publication because the floating ice terms have not been included.

The newly-formed ANT20_H18/NA43c_H18 ice models (see section 3.5.1), corresponding to two scenarios that Antarctica/North America is responsible for the rapid global sea-level drop during the late LGM (approximately 25 to 20 ka BP) revealed by the new observations from the Great Barrie Reef (GBR; Webster et al., 2018, Yokoyama et al., 2018), is given in Figure 4.4/S1. Both of these scenarios present a ~15 m global sea-level drop, comparing to the Antarctic scenario that experienced a gradual ice-sheet growth of ~4 m/ka from 24 to 20 ka BP, the North American scenario indicates a rapid ~15 m ESL ice volume increase between 22 to 21 ka BP.

4.2 Observational Sea Level Datasets

In the upper panel of Figure 4.5, we plot the age distribution of two observational far-field RSL datasets. A total number of 952 and 1474 observations are included in the L14 and H18 datasets dating up to 25 ka BP. By including new observations from Noggin Pass and Hydrographer's Passage, Great Barrier Reef (GBR), the H18 dataset provides a significantly higher temporal resolution during the late glacial period, which reveals a rapid sea-level drop during 25 to 20 ka BP (Figure 4.5 c). This indicates that during the late LGM the cryosphere was much more dynamic than previously thought (Yokoyama et al., 2018), possibly, this can be attributed to a growth spurt in one or more ice sheets (Whitehouse, 2018a). Apart from this, H18 presents a much noisier sea-level variation signal during Holocene, which is most likely due to the ocean syphoning effect, which may dominate Holocene RSL variation signals in some intermediate-field records in the Caribbean region such as Barbados and Belize (Monacci et al., 2009, Wooller et al., 2009). Hence, the H18 dataset is more sensitive to the Earth rheology compared to L14. The geographical distributions of the two datasets are given in Figure 4.5 b, many of the observations adopted in L14 and H18 are identical. The major difference between these two datasets are: (*i*) H18 covers more intermediate-field records in the Caribbean region; (*ii*) H18 has ~100 more observations than L14 in New Zealand, most of which relate to Holocene sea-level change; (*iii*) L14 has more observations from East Asia sediment records, dating from late glacial period to late Holocene; (*iv*) H18 does not include the most complete coral record in the L14 dataset (Kiritimati Atoll; Woodroffe et al., 2012).

The noisiest observation cluster for H18 occurs between 15 to 14 ka BP, where the observations from Tahiti (Deschamps et al., 2012) are significantly lower compared to records from Sunda Shelf (Hanebuth et al., 2009, Hanebuth et al., 2000) and Barbados (Abdul et al., 2016, Fairbanks, 1989). This is largely because the Tahiti records are collected from drill cores in a prograding reef setting, which results in shallow water species that adopt the catch-up mode replaced by deep tolerant species up-core in the same core. As a result, there are large uncertainties associated with Tahiti records. However, since the inclusion of the Tahiti record
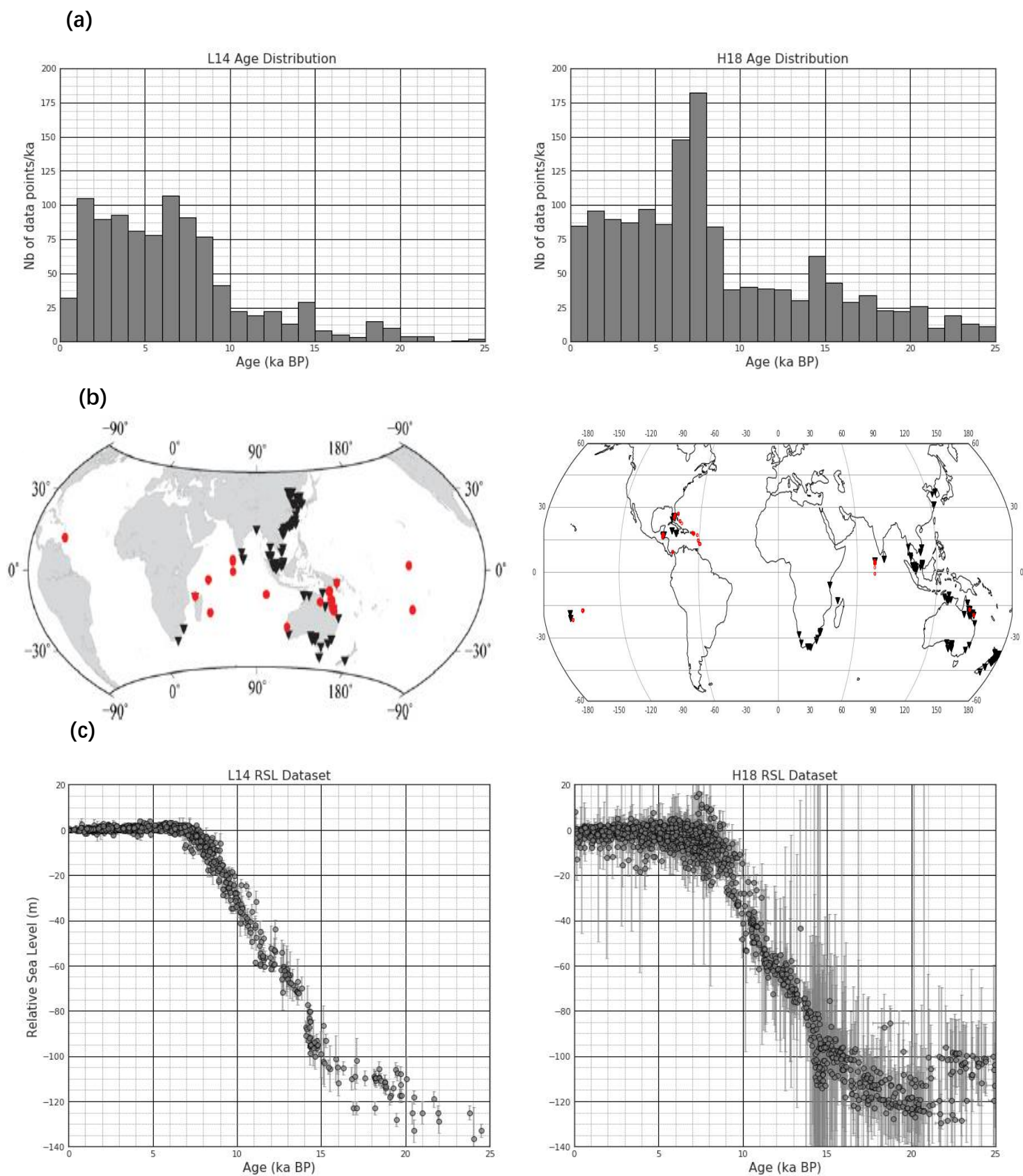
(a)

(b)

(c)

Figure 4.5 Spatio-temporal distribution of two far-field sea-level datasets for the past 25 ka. The left and right column of figures are for the L14 and H18 dataset, respectively. (a) Time distribution of the two datasets. (b) Geographical distribution of far-field coral (red dots) and sediments/other records (black triangles) for two datasets. (c) Paleo RSL-age relationship of two datasets with 2σ uncertainties, for L14 dataset, age uncertainties are inclusive in vertical uncertainties in a quadratic term. The black triangles for the H18 dataset in (b) also include some coral records with poorly-known depth-habitat range. The left Figure of (b) is from Lambeck et al., (2014).

yielded nearly-identical results, and other records during this period are within the uncertainty range of the Tahiti records, we retain the Tahiti records to achieve a higher spatio-temporal resolution.

Because of the sophisticated methodology used to construct the H18 dataset, it is more representative of the complicated nature of coral's depth-habitat relationship. And correspondingly, H18 presents much larger vertical uncertainties than L14, which results from the elusive depth-habitat distribution or facies formation range, but also from including the GIA correction uncertainties (see Figure 3.3 and 3.4). The original paleo RSL uncertainty provided in the H18 dataset, as well as the GIA correction uncertainty, are both strongly asymmetric. However, integrated implementation of asymmetric error propagation in GIA modelling requires a comprehensive investigation, which is not supported by the current version of GIA software and out of the scope of this study. Therefore, we assume all errors to be Gaussian (as presented in Figure 4.5).

4.3 Global Ice Volume History

4.3.1 *Mantle Rheology for H18 Dataset*

The resulting variance (Ψ^2) values (equation [3.2]) for two late LGM rapid ice-sheet growth scenarios are presented in Figure 4.6, which are generated by combining two ice model scenarios with a suite of Earth parameters. The minimum Ψ^2 value of 22.4/21.1 for the NAIS/AIS scenario corresponds to ~10.4/10 of commonly-used chi-square misfit (χ^2) estimates given by:

$$\chi^2 = \frac{1}{M} \sum_{m=1}^{M} \left(\frac{S_{obs}^m(\omega, t) - S_{pred}^m(\omega, t)}{\sigma^m} \right)^2 \quad [4.2]$$

where M is the number of RSL observations, $S_{obs}^m(\omega, t)$, $S_{pred}^m(\omega, t)$ and σ_m are the prediction, observation and vertical uncertainty of m-th RSL record at location ω and time t respectively. These χ^2 values are larger than the ~3 chi-square misfit achieved by fitting the L14 dataset with the ANU ice model (Lambeck et al., 2014) even considering the uncertainties are considerably larger in the H18 dataset, which is mostly due to either the different sea-level reconstruction methods adopted for the H18 and L14 (which is used to constrain the ANU ice model) datasets or the much noisier RSL signal presented in the H18 dataset (see Figure 4.5 c). A careful reassessment of each observational record may lead to a significant variance reduction. However, as to the former problem, each ice model needs to be adjusted for the ice volume history constrained by the both near-field and far-field sea-level reconstruction using identical methods to those used to develop H18, which is much more arduous but could possibly be a new clue to re-examine
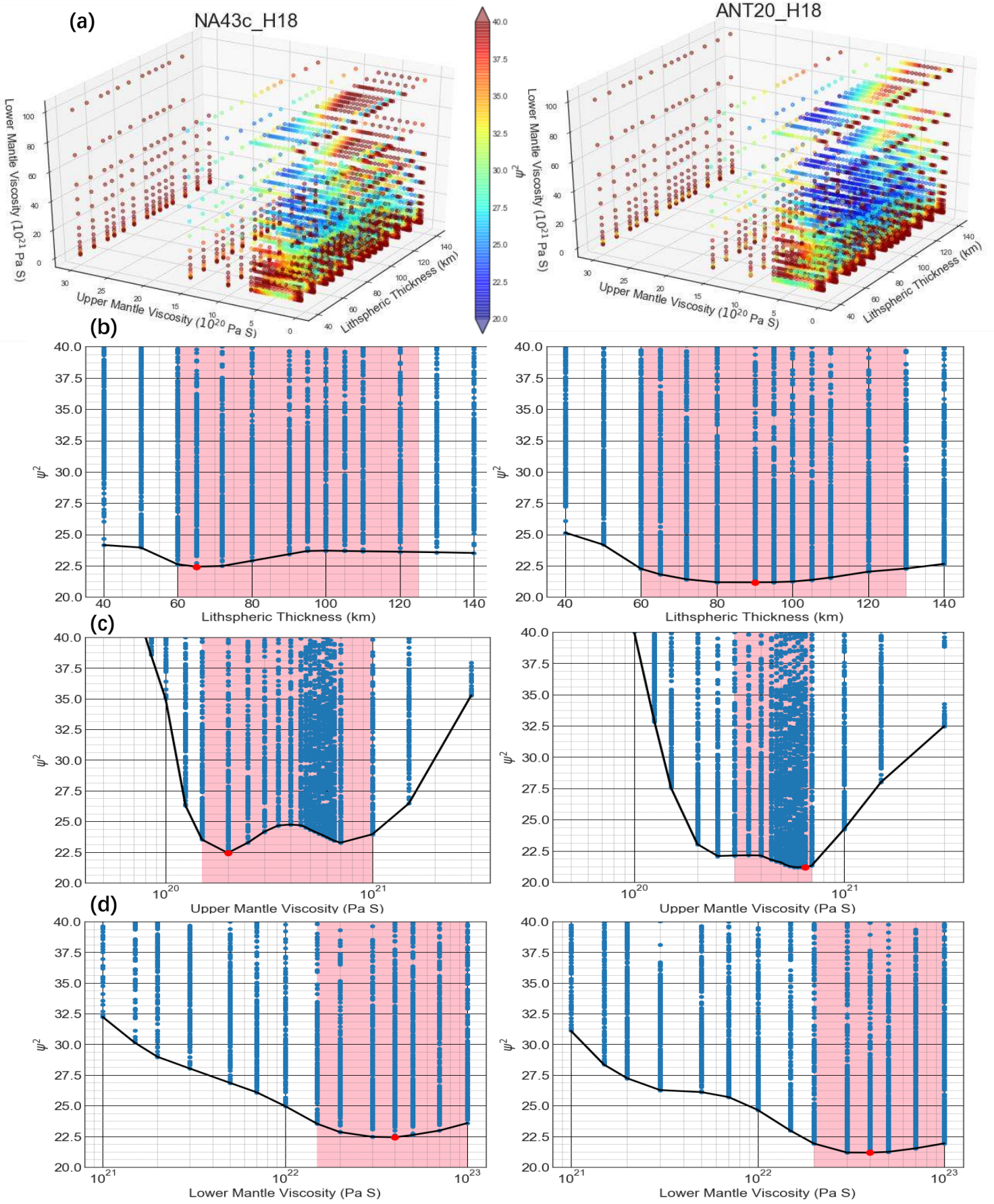
Figure 4.6 Earth-parameter solution for two late LGM rapid ice growth scenarios. The left/right column corresponds to the North America/Antarctica scenario. (a) 3D scatter plots of the variance values. (b,c,d) The variance value as a function of lithospheric thickness, upper and lower Mantle viscosity. The blue points are the tested Earth parameters. The black line indicates the minimum variance function and the red dot indicates the minimum value. The red bands indicate 95% confidence interval.

ice volume changes in the LGM and investigating the 'missing ice' problem.

The confidence interval for Earth parameters across the searching space is estimated using the statistics:

$$\Phi^2 = \frac{1}{M} \sum_{m=1}^{M} \left(\frac{S_{pred*}^m - S_{pred,k}^m}{\sigma^m} \right)^2 \quad [4.3]$$

where $S_{pred,k}^m$ are predicted RSL value for m-th observation and k-th Earth model; S_{pred*}^m is the counterpart corresponding to the Earth model with lowest Ψ_k^2 value. The 95% confidence intervals are defined by the contour of $\Phi^2 = 2$. The distributions of Ψ_k^2 value for two scenarios show a similar subset of best-fitting Earth parameters (Figure 4.6 a) with weak dependence upon the lithospheric thickness and a strong dependence upon upper-mantle viscosity. The best-fitting Earth model (red dot in Figure 4.6) for the NAIS/AIS scenario has a lithospheric thickness of 70/90 km, an upper mantle of $2/6.5 \times 10^{20}$ Pa S, and an upper mantle of 4×10^{20} Pa S. The NAIS scenario's 95% confidence interval points to a large range between $1\text{-}10 \times 10^{20}$ Pa S with two local minima occurring between $2\text{-}4 \times 10^{20}$ Pa S and $7\text{-}10 \times 10^{20}$ Pa S. Due to the large sampling gap between $7\text{-}10 \times 10^{20}$ Pa S upper-mantle viscosity, this local minimum can potentially be equally satisfactory as the current best-fitting model, indicating a common two-minima problem in GIA modelling (e.g., Lambeck et al., 2014). In contrast, the AIS scenario is more robust since there is only one global minimum occurring within the area of high sampling density with a much narrower 95% confidence interval. However, as the Ψ_k^2 difference between these two scenarios is indistinguishable (22.4 vs. 21.1) for choosing a preferable scenario to determine the global ice volume history, we construct the underlying ESL signal for both scenarios, which is given below.

4.3.2 *Post-LGM Global Ice Volume History*

Given the best-fitting Earth-parameters (Figure 4.6) and ice model (Figure 4.4 and S1) corresponding to two late glacial rapid ice growth scenarios, the individual ESL estimate for each observed sea-level record along with the denoised ESL time series are plotted in first and second columns of Figure 4.8. The third column is the counterpart for the GIA corrected L14 dataset generated by replicating the original method introduced in Lambeck et al. (2014). All three ESL functions are generated using geographically well-spaced observations with appropriate corrections for isostatic effects. However, there are some observable disparities between these three results due to the different paleo sea-level reconstruction methods in conjunction with different ice and Earth models (section 4.1 and 4.2). A full discussion of these disparities will be covered in section 5.1. We adopt the Antarctic scenario ESL function as a preferable solution for

H18 dataset for further investigation on its consistency with different AIS models' predictions for the following reasons:

1. During the late LGM, the rapid increase in ice volume from ~25 ka observed in the Antarctic scenario ESL function is more chronologically consistent with the age for Heinrich event 2 (~25 ka; Grousset et al., 2000, Vidal et al., 1999) compared to the North American scenario, which indicates a more oscillatory variation that has no corresponding paleoclimate correlation.

2. The Antarctic scenario presents a clearer ESL signal during the late glacial period between 20 to ~16.5 ka BP. Compared to the results of Lambeck et al. (2014) that indicates a rapid sea-level rise from ~16.5 ka BP, the Antarctic scenario ESL curve shows a more gradual sea-level rise signal from ~17.1 ka BP (see Figure 4.7 for the locations of abrupt gradient change). This shows greater consistency with Heinrich event 1 at about 17 ka BP, which marks the point of which full deglaciation kicked in as the pace of Northern Hemisphere insolation and atmospheric carbon dioxide levels increased rapidly (Yokoyama et al., 2018). In comparison, the North American scenario has noisy and, to some extent, artificial oscillations during this period that is not supported by paleoclimatic evidence.

3. The locations of changepoints (i.e., ages where rates of sea-level change change abruptly) for two scenarios are shown in Figure 4.7. For the Antarctic scenario, each cluster of changepoints is nearly normally distributed with a clear peak. In contrast, the North American scenario shows unconvincingly large frequencies at ~8 and ~9 ka BP, corresponding to an abrupt sea-level rise during this period, which may be consistent with the Meltwater Pulse 1C (Liu et al., 2004) but the magnitude of sea-level rise (above 50 m/ka) is still unrealistic.

4. The Antarctic scenario presents a slightly better fit to the H18 dataset with a lower Ψ_k^2 value and a unique global minimum (Figure 4.6).
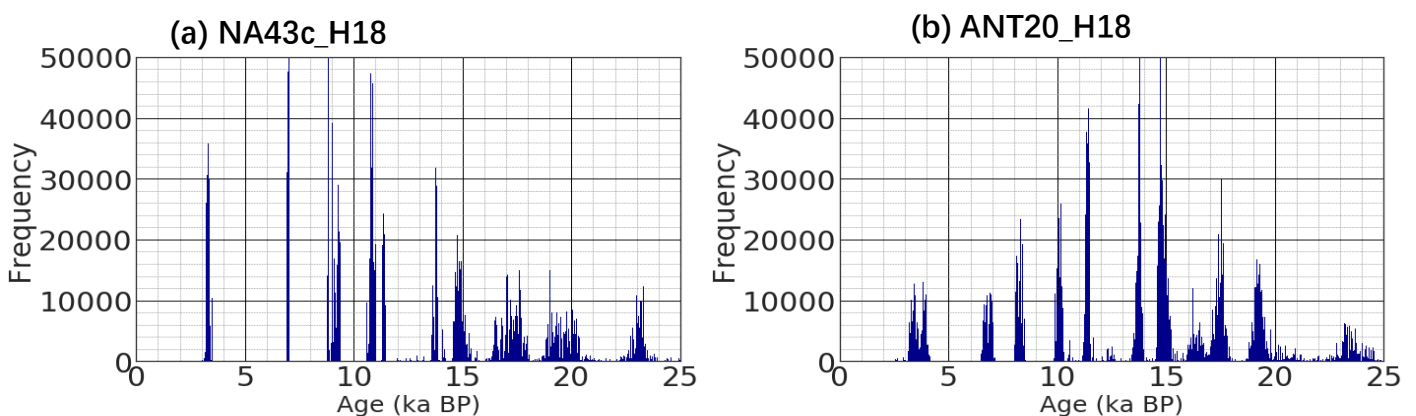

Figure 4.7 Comparison of partition modelling results for the location of gradient changepoints. The location of gradient changepoints indicate the possible timing of abrupt sea-level changes, which is generated by the second half of 1,000,000 Markov chain Monte Carlo runs. (a) NAIS scenario, corresponds to the first column of Figure 4.8; (b) AIS scenario, the second column of Figure 4.8
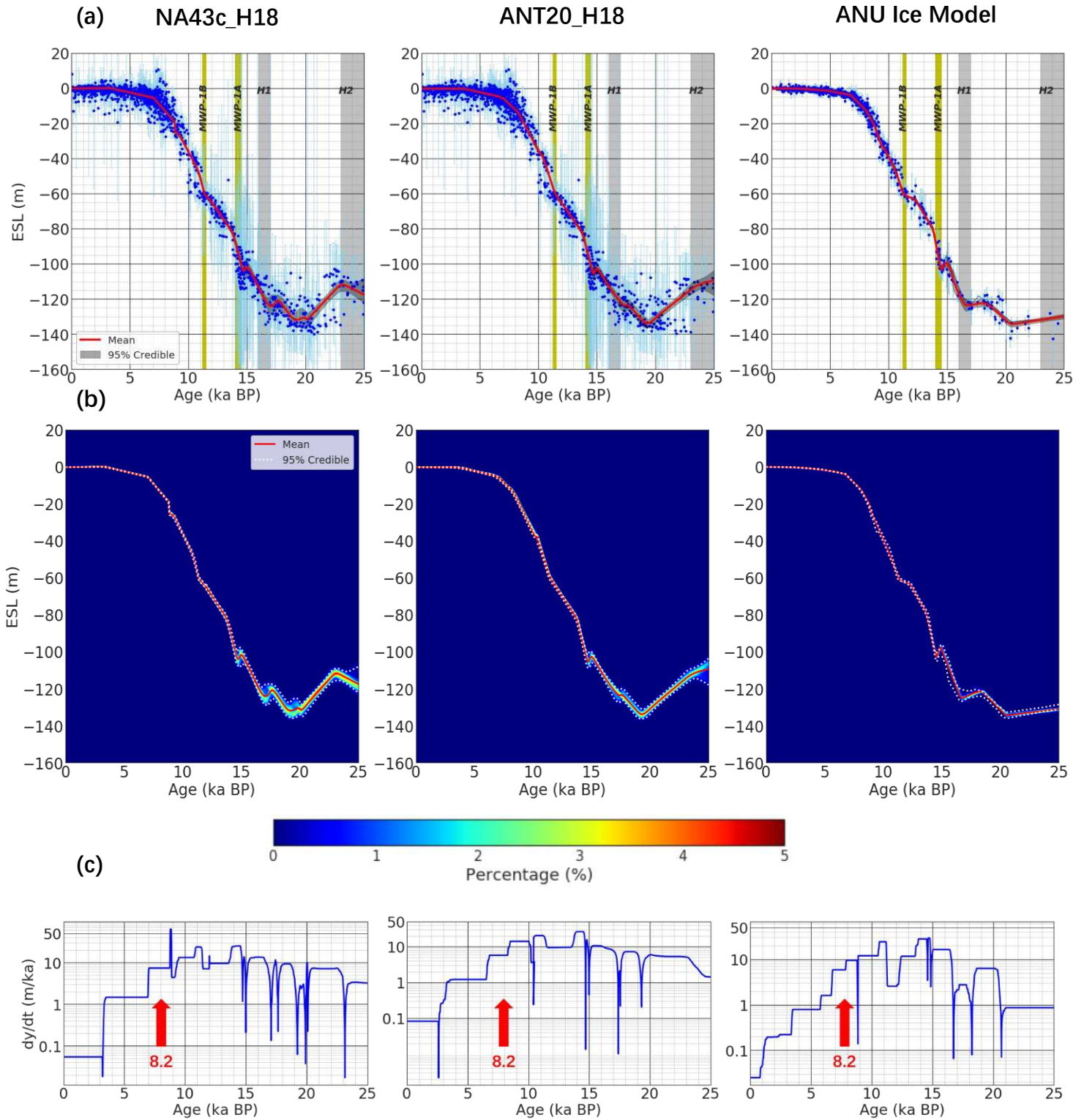
Figure 4.8 Solutions for the global ice volume function (i.e., ESL function). Each column corresponds to one ice model, the first two columns use the H18 observational RSL dataset with the adjusted NAIS/AIS models within the ANU global ice model, and the third uses the L14 dataset with the original ANU ice model. (a) Individual ESL signal estimates (blue error bars with 2 σ uncertainties) and the denoised time series (red line) with 95% confidence interval, the vertical green bars indicate the timing of MWP1A and MWP-1B, the grey bars indicate the timing of Heinrich Events H1 and H2. (b) Ensemble density of each solution, the running mean path is shown as the red line. The 95% confidence intervals are shown as white dotted lines. (c) Sea-level change rate obtained from the denoised time series, red arrows indicate the timing of 8.2 cooling event in Northern Hemisphere.

4.3.3 *Rescaled North American Ice Models*

As described in section 3.6, in order to ensure a closed global sea-level budget, the original NA43c model is rescaled to compensate for the 'missing' ice volume caused by replacing the ANT20/ANT20_H18 model (i.e., the AIS model for the L14/H18 dataset, Figure 4.4) with three different AIS models (W12, IJ05_R2 and ICE-6G_C). The L14 and H18 ESL functions for the 'missing ice' and rescaled NAIS models are given in the left and right panels of Figure 4.9. We do not rescale the NAIS model to fit the new ESL curve described above after 20 ka BP since during this period the NA43c model is well-constrained by near-field observations and GPS observations (Lambeck et al., 2017). In this case, the only difference between the ice model adopted for different observational RSL datasets is the volume of 'missing ice' between 25 to 20 ka BP when ANT20 predicts a uniform Antarctic ice volume but ANT20_H18 predicts a gradual ice volume gain. Observably, although the overall trend for all NAIS models is similar, the adjusted models contain at least ~15 m sea-level equivalent ice volume larger than the original NA43c model, which are greatly outside of the commonly-used ~5 m uncertainty range for NAIS models (Simms et al., 2019). Additionally, the maximum 'missing ice' volume for each adjusted model occurred at different times due to detailed
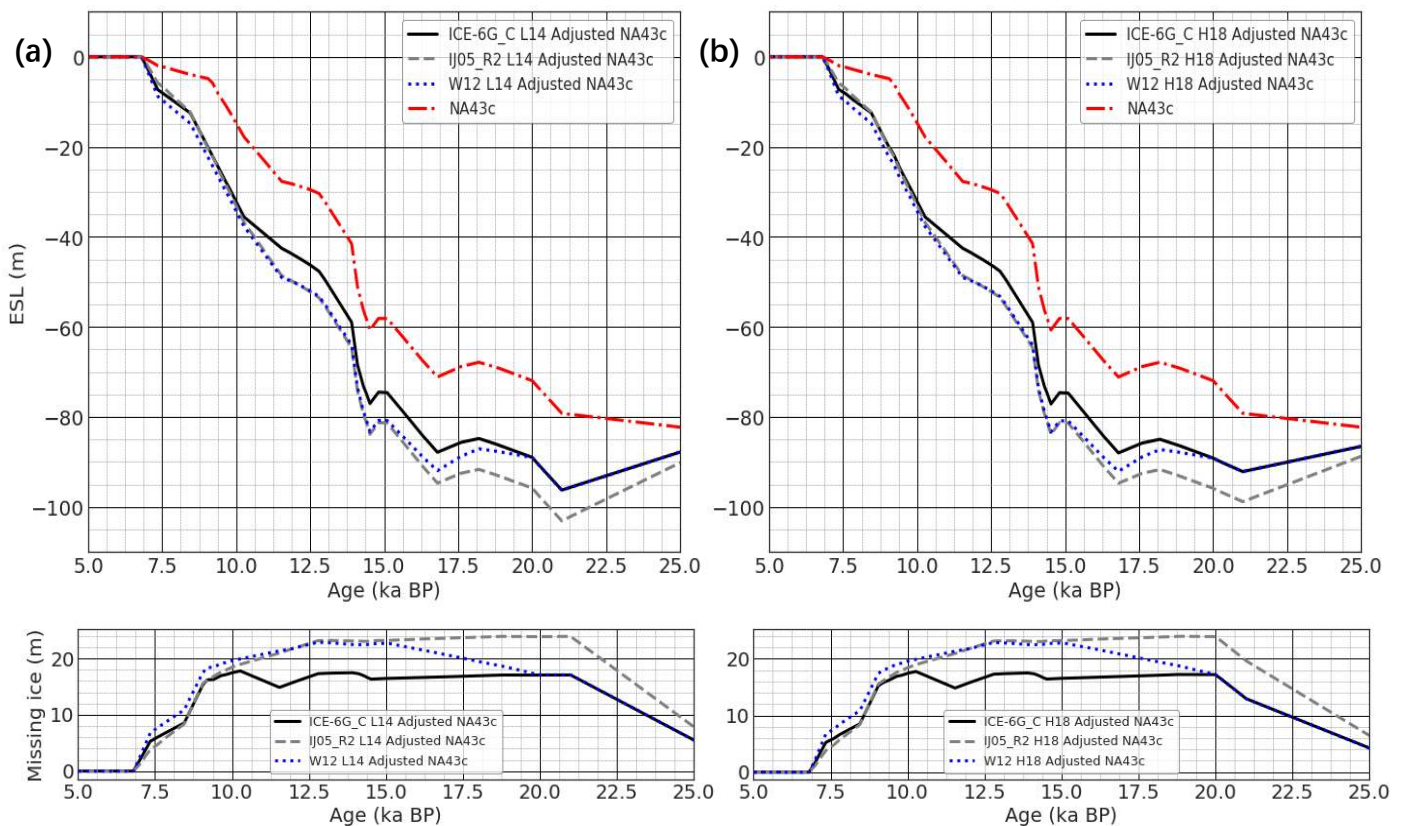

Figure 4.9 The adjusted North American deglaciation model according to two observational datasets and three Antarctic deglaciation models. The upper panel is the adjusted North American deglaciation history, the lower panel indicates the enlarged ice amount for each Antarctic ice model (i.e., 'missing ice' amount). (a) W12 (blue line), IJ05_R2 (grey line) and ICE-6G_C (blue line) adjusted North American ice sheet model for L14 dataset; (b) same as (a) but is adjusted for H18 dataset.

differences in deglaciation history, specifically, occurring at 13, 13.5 and 21.5 ka BP for W12, ICE-6G_C and IJ05_R2, respectively.

4.4 Mantle Rheology for AIS Models

Table 4.1 List of Best-fitting Earth Parameters for each ice model and dataset

	Lithospheric Thickness (km)		Upper-Mantle Viscosity (10^{20} Pa S)		Lower-Mantle Viscosity (10^{21} Pa S)		Lowest Ψ^2 (21 to 8 ka BP)	
	L14	H18	L14	H18	L14	H18	L14	H18
W12	60# [40,90]*	60 [40, 130]	3.5 [2, 6.5]	4.75 [3, 6.5]	20 [10, 50]	20 [15, 30]	8.45+	21.37
IJ05_R2	50 [40,90]	60 [40, 130]	3 [2, 6.25]	4 [2.5, 6.5]	30 [15, 70]	30 [15, 40]	7.57	20.20
ICE-6G_C	60 [40,90]	60 [40, 130]	3.5 [2, 6.5]	5.25 [3, 6.5]	30 [15, 70]	20 [15, 40]	8.34	19.92
ANT20/ ANT20_H18	65 [50,110]	60 [50, 140]	4.75 [2.5, 7]	6.5 [3, 7]	70 [20, 100]	40 [20, 100]	8.33	19.38

\# indicates the best-fitting Earth parameter

* indicates the corresponding 95% confidence interval

\+ indicates the lowest variance value corresponding to the best-fitting Earth parameters

The best-fitting Earth-parameters with corresponding 95% confidence intervals for each global ice model to fit L14/H18 observational dataset are given in Table 4.1 (full solutions for Earth-parameter searching like Figure 4.6 are shown in Figure S3). All ice models are able to achieve relatively good agreement with the far-field sea-level observations, which are most sensitive to the global ice volume history (identical for all ice models adopted for each RSL dataset) on millennial time scales rather than the origin of ice sheets that caused the sea-level rise. Surprisingly, IJ05_R2 shows a conspicuously better fit to the L14 dataset with the lowest variance value of 7.57, which is around 10% lower than fits of ~8.35 achieved by the other three ice models. However, caution must be used to examine whether this 10% Ψ^2 improvement is attributed to better fit to observations with inappropriately small uncertainties (see section 4.5.2). The best-fitting solution to the H18 dataset is attained using the ANT20_H18 model, similarly, showing a ~10% Ψ^2 improvement compared to other ice models. A noteworthy point is that, both of the best-fitting models indicate nearly no ice mass loss occurring between 20 to 15 ka BP, showing good consistency with studies of till provenance and the orientations of geomorphic features on Ross Sea (Anderson et al., 2014) and terrestrial and marine data on Weddell Sea (Hillenbrand et al., 2014, Hillenbrand et al., 2012). Although ICE-6G_C does not achieve best-fit to either one observational dataset, it does produce reasonably good fits to both observational datasets possibly because it also has no ice mass loss before 15 ka BP. As the only

model that predicts a significant ice melt during the late glacial period (i.e., 20-15 ka BP), W12 has the highest misfit compared to both datasets adopted in this study, which means the deglaciation history of W12 during this period is inconsistent with the far-field sea- level observations.

The two observational datasets show good agreements in terms of the best-fitting Earth parameters, which are all well within the 95% confidence intervals constrained by two datasets. The best-fitting lithospheric thickness for all ice models are almost identical to ~60 km, the 95% confidence interval of the H18 dataset has lower resolution compared to the L14 dataset. This is because H18 contains more records from midocean small islands that have little resolution for the thickness of the lithosphere (Figure 4.5; Lambeck et al., 2014). Likewise, there are only small differences between the lower mantle viscosity obtained from H18 and L14. The largest discrepancy between the two datasets is the viscosity of upper mantle where H18 prefers a higher viscosity than L14. This discrepancy is strongly related to the sea-level reconstruction method, because the H18 dataset relies on the empirically-derived coral depth-habitat distribution that predicts a shallower paleo sea level (see the median value of PRSL in the upper panel of Figure 3.3) compared to method adopted in the L14 dataset that assumes a normally distributed depth-habitat within the growth range (i.e., $\delta\xi_d/2$ in equation [3.1]). And hence, under the same amount of water load, a more viscos upper mantle is preferable for these shallower paleo sea-level observations in H18.

Another intriguing feature is that the best-fitting upper-mantle viscosity increases with the Antarctic contribution to post-LGM sea-level rise. For IJ05_R2/W12, which contains ~8 m ESL at the LGM, the best-fitting upper-mantle viscosity is relatively low at $3/3.5 \times 10^{20}$ Pa S and $4/4.75 \times 10^{20}$ Pa S for L14 and H18 dataset. Conversely, ANT20, which predicts much larger Antarctic ice volume at the LGM, shows a more viscous upper mantle of 4.75 and 6.5×10^{20} Pa S for L14 and H18 respectively. A possible explanation for this feature is that a larger Antarctic post-LGM sea-level rise contribution leads to a larger ocean load imposed on the regions where most observational records are located, such as Caribbean, GBR and South Asia (Figure 4.12). In order to provide better fitting to these observations, a more viscous upper-mantle viscosity is required to balance the increased ocean load.

These results are consistent with the preferred 'high' viscosity solution of Lambeck et al. (2014) which yielded a lithospheric thickness of 50 km, upper/lower mantle viscosity of 1.5×10^{20} Pa S/70×10^{21} Pa S. The reason for the slightly higher upper-mantle viscosity is possibly due to the exclusion of Holocene sea-level records after 8 ka BP. Similarly, the results of this study shows good consistency with the global-scale Earth model (VM5a) by Argus et al. (2014) that predicts a elastic lithospheric thickness of 60 km, upper-

mantle viscosity of 5 × 10²⁰ Pa S and averaged lower mantle viscosity of ~2.5 × 10²¹ Pa S. The one magnitude higher lower-mantle viscosity produced in this study can be possibly attributed to the relatively higher lower-mantle viscosity (relative to global average) in the East-South Asia, Australia and the Caribbean regions, where most of the records collected from, revealed by a recent study of inversion of laterally heterogeneous viscosity model using ICE-6G_C global ice model (Li et al., 2018).

4.5 Sea-Level Predictions & Misfits
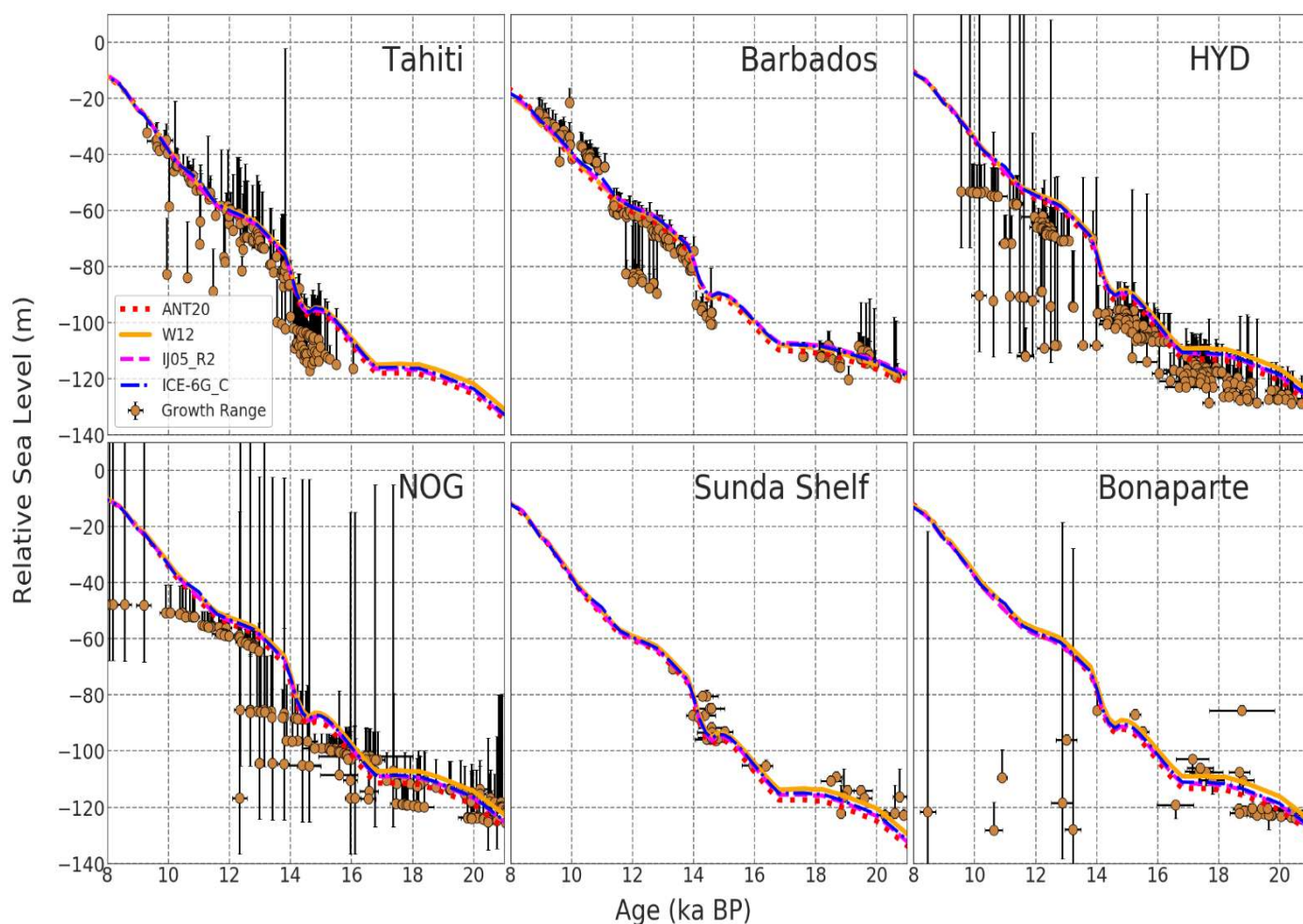
Figure 4.10 The sea-level predications by ice models for L14 dataset with corresponding best-fitting Earth models for selected sites. The growth ranges showing here are from the original publication. The horizontal error bars are 2 σ uncertainties for age estimations from the literature. HYD = Hydrographer's Passage, NOG = Noggin Pass, both from Great Barrier Reef.

4.5.1 *Sea-Level Predictions on specific sites*

A comparison between sea-level predictions, generated by combining the L14/H18 ice models with their best-fitting Earth models (Table 4.1), and original records' tectonically corrected elevations and growth

ranges are given in Figure 4.10/S4 for the six most complete RSL records: Tahiti (Bard et al., 1996, Bard et al., 2010, Deschamps et al., 2012), Barbados (Abdul et al., 2016, Bard et al., 1990, Fairbanks et al., 2005, Peltier and Fairbanks, 2006), Hydrographer's Passage and Noggin Pass from Great Barrier Reef (Yokoyama et al., 2018), Sunda Shelf (Hanebuth et al., 2009, Hanebuth et al., 2000) and Bonaparte Gulf (Ishiwa et al., 2016, Nicholas et al., 2014, Yokoyama et al., 2001, Yokoyama et al., 2000). As mentioned in the last section, the Earth model is like a 'regulator' to balance the different ocean loading imposed by different AIS deglaciation models, far-field sea-level observations are not sensitive to the Antarctic contribution to post-LGM sea-level rise. For example, ANT20 (with 28 m ESL at the LGM; red dotted line in Figure 4.11) yields similar RSL predictions to IJ05_R2 (with only 7.5 m ESL at the LGM) with subtle disparities. The only distinct feature is that W12 (solid orange line in Figure 4.11) predicts a higher RSL between 20-15 ka BP, which correlates to the high ice loss rate within this period predicted by W12.

4.5.2 *Sea-Level Prediction Misfits on Specific Periods*

The misfits between modelled and observed RSL at different time slices are shown in Figure 4.11, we calculate the χ^2 misfits (equation [4.2]) for each 1 ka time interval to investigate the goodness of fit for each AIS model in specific time slices. There are four bars within each 1 ka time interval, indicating each AIS model's misfit in this 1 ka time interval. For the L14 dataset, there are two groups that present an anomalously large misfit occurring between 20-19 and 12-11 ka BP. The large χ^2 misfit between 20-19 ka BP can also be observed in the H18 dataset shown in the right panel of Figure 4.11, which is due to the discrepancies between Barbados, Bonaparte Gulf and GBR observations (Figure 4.10 and 4.8 a). Within this time interval, records from Barbados and Noggin Pass indicate a ~10 m lower RSL compared to records
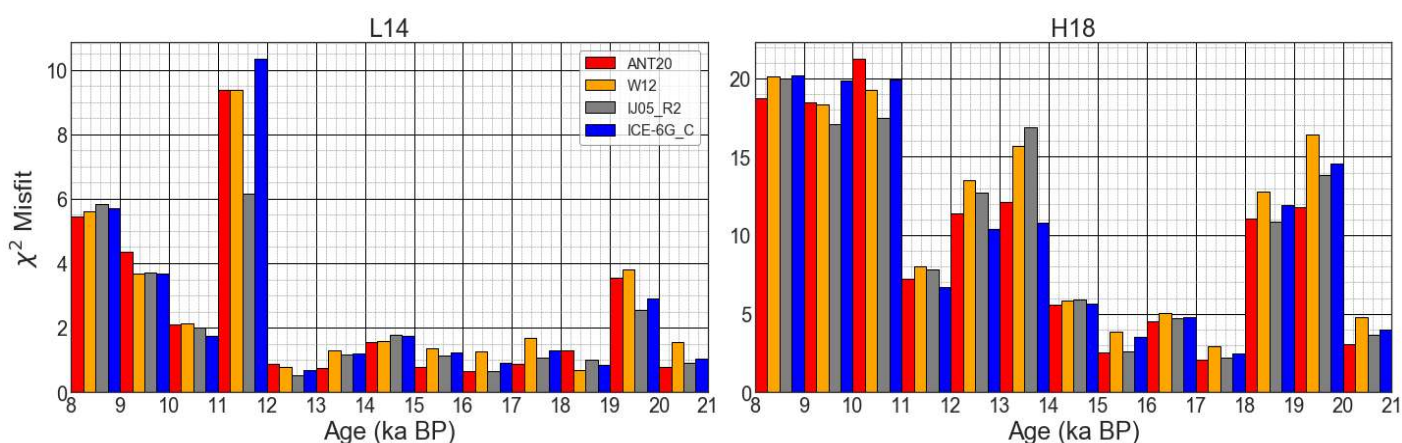

Figure 4.11 A bar plot shows the χ^2 misfits of modelled sea-level predictions by different Antarctic deglaciation models with corresponding best-fitting Earth models. Each four bars from left to right in different colour is a group of chi-square misfit for four Antarctic ice models (red: ANT20, orange: W12, grey: IJ05_R2, blue: ICE-6G_C) comparing to the observations within each 1 ka time interval from 8 to 21 ka BP. The left and right panel correspond to different RSL observational datasets.

from the Bonaparte Gulf and Hydrographer's Passage, which might be indicative of additional processes like tectonic-caused displacement in Barbados (Bard et al., 2010) or different local ecological controls on two GBR sites (since these two GBR sites are 500 km away from each other, difference of GIA effect on these two sites are relatively small). However, the large misfits observed in L14 during 12-11 ka BP is not consistent with the results produced by the H18 dataset, which show a comparatively lower misfit. The majority of the misfit for L14 dataset is due to four sediment records from the Comoro Archipelago (western Indian Ocean; Zinke et al., 2003) with relatively low 1σ RSL uncertainties between 0.5 and 2 m. In comparison, RSL predictions during this period show good agreement with the H18 dataset that incorporates geographically well-distributed data from Tahiti, GBR, New Zealand (Ota et al., 1991), East China (Liu et al., 2010) and also the Comoro Archipelago, but the assigned 1σ uncertainties for which are all ~3 m in the H18 dataset. If the latter uncertainty estimates are more accurate, the L14 χ^2 misfits for this period will be reduced to ~1 level. Similar to the results given in Lambeck et al. (2014), excluding the Comoro Archipelago observations from the analysis does not lead to a different best-fitting Earth model or a different order of Ψ^2 misfits from different AIS models. The only difference is the 10% Ψ^2 improvement achieved by IJ05_R2 (Table 4.1) reduces to 5%.
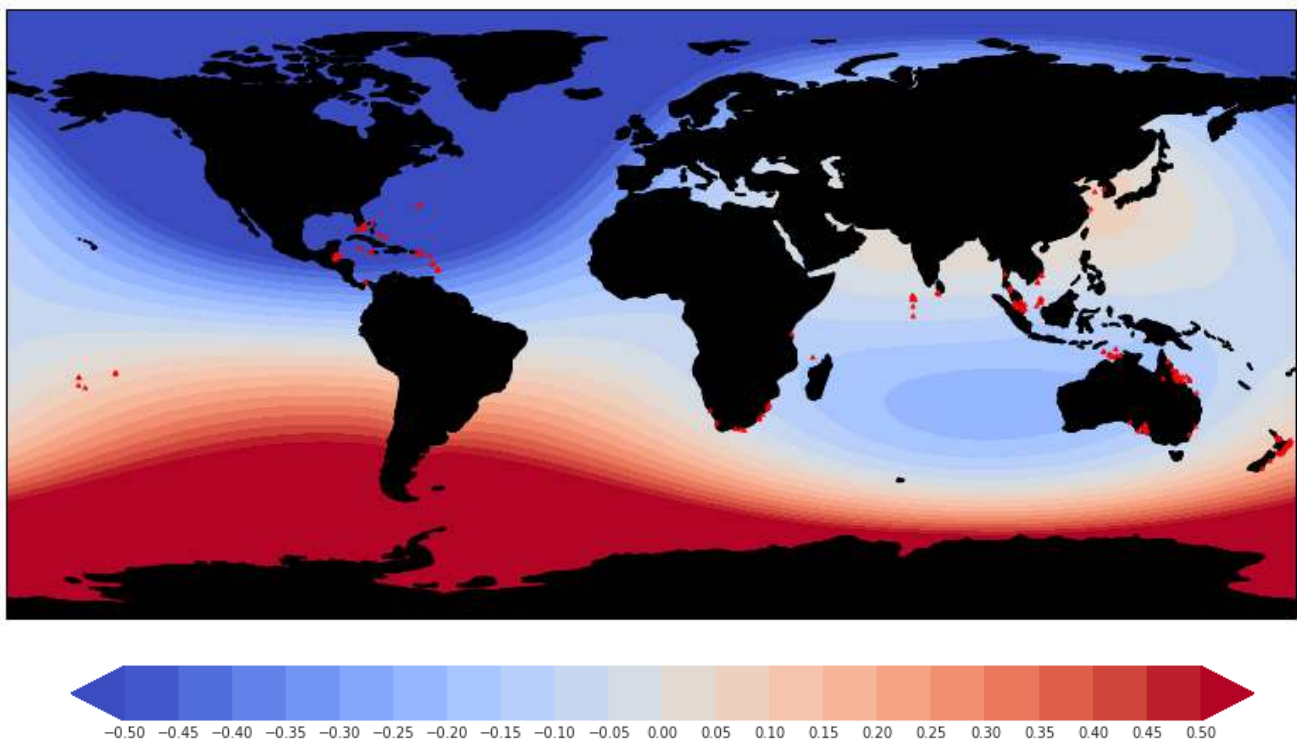

Figure 4.12 Difference between the normalized North American Ice Sheet and West Antarctic Ice Sheet (WAIS) sea-level fingerprint. A region with positive value indicates ice loss originated from NAIS will rise more local RSL than WAIS and vice versa. Red triangles indicate the observational sites in the H18 dataset.

W12 shows considerably higher misfit between 20-15 ka BP (orange bars in Figure 4.11) for both observational datasets. This large misfit is majorly attributed to the disagreements with the records from the Bonaparte Gulf, Barbados and GBR, where W12 predicts a higher RSL during 20-15 ka BP (Figure 4.10 and S4), which is due to the meltwater redistribution trend differs between the NAIS and West Antarctic Ice Sheet (WAIS; where most of Antarctic ice mass loss originated from, see Figure 4.2). Figure 4.12 shows the difference between normalized meltwater fingerprint of the NAIS and WAIS. Compared to the NAIS, the same amount of ice melting in WAIS will cause a higher local sea-level rise in most of the regions where sea-level records are located (blue area in Figure 4.12). This confirms that the significant ice mass loss during this period predicted by W12 is responsible for the overestimations of the far-field RSL and large misfits. Therefore, during this period, AIS cannot have a significant retreat phase. Instead, a stable or an advanced phase is more preferable by the far-field sea-level observations. This suggests far-field sea-level observations have the ability to distinguish large discrepancies in melting rate between different AIS models and can provide some critical information on the validity of different Antarctic deglaciation histories in some specific periods.

Another evidence for this ability can be observed from the χ^2 misfit results from the beginning of the Bølling-Allerød interstadial (14.7 ka BP; Cronin, 1999) to the end of MWP-1B (~10.3 ka BP, see Figure 4.8 c) when global sea-level rose rapidly. As the only model that predicts a distinctly larger Antarctic contribution to MWP-1A and MWP-1B, the ICE-6G_C model produces the best fit (8.0 χ^2 misfit compared to 10.3, 10.6 and 8.8 for W12, IJ05_R2 and ANT20) to the geographically well-distributed observations in the H18 dataset from Barbados, Tahiti, GBR, Sunda Shelf, New Zealand, East China, Yellow Sea China (Kim and Kennett, 1998), Comoro Archipelago and Vietnam Shelf (Hanebuth et al., 2009, Michelli, 2008) for this period. This improvement in χ^2 misfit is not observable for the L14 dataset because the L14 dataset has not been updated for including the extensive high-quality records from GBR. After the inclusion of GBR records to the L14 dataset (using the same sea-level reconstruction method as L14), the ICE-6G_C also shows the best fit (10.1 χ^2 misfit compared to 11.2, 10.8 and 10.8 for W12, IJ05_R2 and ANT20) during this period. Therefore, this suggests that a larger Antarctic contribution to both MWP events is preferred by far-field sea-level observations, which is consistent with previous GIA fingerprinting studies (Clark et al., 2009, Clark et al., 2002), Antarctic GIA analysis (Bassett et al., 2007), climatic/ocean circulation modelling study (Golledge et al., 2014, Weaver et al., 2003) and Antarctic ice-rafted debris records (Weber et al., 2014).

Because our method is only sensitive to large discrepancies in ice melting rate, the overall gradual ice melting rate predicted by ANT20 and IJ05_R2 between 20-10 ka BP cannot provide information on the Antarctic deglaciation history or their validities although they are both in good agreement with far-field sea-level observations. After the beginning of Holocene (~11.2 ka BP) the χ^2 misfits show a clear increasing trend due to the much noisier ESL signal in both of the L14 and H18 datasets although conservative estimates of observational accuracies have been made for the L14 dataset. This is because following the decay of continental ice sheets during MWP events, our oversimplified 1-D radially stratified Earth model cannot fully capture the collapse of peripheral bulges during Holocene since the mantle viscosity underneath these regions are not identical as the mid-ocean island and continent-ocean margin regions where most of the sea-level records are located. Therefore, we are not able to distinguish whether the rate of ~12 m/ka Antarctic ice mass loss predicted by the ANT20 model during 8-9 ka is realistic.

Chapter 5 Discussions

5.1 Implications on the Last Deglacial Global Ice Volume History

In this study, we adopt a new global far-field sea-level dataset (H18) that incorporates most of the recently-discovered high-quality records based on a more sophisticated sea-level reconstruction methodology. Since this dataset has just been published, currently, there is no consensus on whether this empirically-derived reconstruction method is accurate or suitable for secondary modelling studies. We made the first attempt to use this dataset in a GIA modelling study and proved this dataset is accurate and useful for generating meaningful results.

By using an adapted GIA modelling and McMC approach, we reconstructed the underlying ESL history for the H18 dataset. The result is based on geographically well-spaced observations corrected for isostatic contributions, the new ESL curve yields several different features compared to the original study (Lambeck et al., 2014):

1. During the late LGM, by incorporating extensive observations from two sites in GBR, the new ESL curve presents a period of ice growth of ~25 m ESL from 25 ka BP, showing good consistency with the Heinrich events H2 (Marcott et al., 2011). In comparison, due to the lack of temporal resolution during this period, the original ESL curve shows an approximately constant or slowly increasing ice volume. This large disparity illustrates the cryosphere is much more dynamic than previously thought, and hence, pointing out the great importance of scientific ocean drilling in understanding past sea-level/ice-volume variation and global climate change (Yokoyama et al., 2019b).

2. The two ESL curves present a similar lowest value of ~134 m, corresponding to ~52 × 10^6 km^3 more grounded ice than today. However, a ~10 ka discrepancy exists regarding the time of reaching this lowest ESL value. Compared to the original ESL curve which reaches a low ESL value at ~29 ka BP with a 8-ka period of nearly constant global ice volume, the new ESL curve reaches its lowest value at 19.3 ka BP with a short duration, which agrees well with the timing suggested by a recent study analysing sea-level records from the Bonaparte Gulf (Ishiwa et al., 2019), indicating the continental ice sheets are likely never to have reached isostatic equilibrium.

3. Following the global sea-level minimum, there is a short-lived global sea-level rise of ~10-15 m between ~19.3-17.8 and ~20.5-18 ka BP for the new and original ESL curves respectively. The evidence used to construct the new ESL curve is the sediment records from the Bonaparte Gulf (Ishiwa

et al., 2016) and coral records from GBR, which leads to a shorter ~600-year period of near-constant sea level from ~17.8 to 17.2 ka BP. After this short period, the new ESL curve presents a more gradual global sea-level rise at an average rate of ~9 m/ka from ~17 to 15 ka BP, which coincides with the Heinrich event H1 (about 17 ka BP) that marks the end of glacial conditions associated with increased North Hemisphere insolation and atmospheric carbon dioxide levels (Huybers, 2006). In contrast, due to the low temporal resolution, the sea-level rise in the original ESL curve occurred substantially later than the H1 event at ~16.5 ka BP with a more rapid rate of ~12 m/ka.

4. From ~15 to 14.5 ka BP, there is a rapid global sea-level fall at a rate of ~10 m/ka presented in the original ESL curve based on ~10 observational data points. This oscillation is thought to be caused by the rapid growth of the NAIS during this period (Lambeck et al., 2017; see Figure 4.9), which does not always agree with other NAIS modelling studies (e.g., Gregoire et al., 2012, Tarasov et al., 2012). Our new ESL curve is based on two-times more RSL observations and yields a smaller oscillation during the same period, indicating that a global sea-level oscillation likely occurred before MWP-1A. However, the question remains: (*i*) Whether the NAIS is the only ice sheet that responsible for this oscillation? (*ii*) What is the real magnitude of this event? (*iii*) Are there some climatic/glaciological explanations for this event?

5. Because the new McMC algorithm adopted in this study takes into account the uncertainties in chronology, the new ESL curve shows a relatively slower rate of sea-level rise of ~30 m/ka during MWP-1A with a slightly longer 800 yr duration from ~14.6 to 13.8 ka BP. The starting time of MWP-1A in our new curve is in good agreement with the results from Tahiti/Sunda Shelf records analysis (Deschamps et al., 2012) and a probability analysis study (Stanford et al., 2011), coinciding well with the start of Bølling-Allerød warming. And this ~800 yr duration for MWP-1A is consistent with a study of NAIS ice area-volume analysis (Carlson and Clark, 2012).

6. From the end of MWP-1A to the onset of MWP-1B (at ~11.7 ka BP), our new ESL curve shows less structure compared to the original ESL curve (e.g., a slow-down of global sea-level rise is not observable during Younger Dryas), possibly due to the inclusion of more records with larger RSL assigned within the H18 dataset and the parsimonious nature of Bayesian Inference (see Sambridge et al., 2006), which means given support from data (i.e., large enough data uncertainty), simpler solutions are always preferred over more complex ones (see an example using original McMC algorithm without considering dating uncertainties to interpolate H18 dataset in Figure S5, which also cannot capture the detailed structure during this period). In order to get the full structure of ESL variation during this period, a careful reassessment of each observational record in H18 to remove low-quality data is required.

7. A nearly-uniform period of global sea-level rise during ~11.3-8.2 can be observed in both ESL curves at an average rate of 15 m/ka. The two ESL curves are in good agreement in terms of the onset of MWP-1B at the beginning of Holocene and after the end of Younger Dryas when there is a rapid acceleration in global sea-level rise rate (~11.3 ka BP; Cronin et al., 2007). Comparing to the original ESL curve our result suggests a longer duration of ~1,000 yr from 11.3 to 10.3 ka BP. However, due to the noisy ESL signal during this period (Figure 4.7 a), this longer duration for MWP-1B is still ambiguous.

During the mid-to-late Holocene, the H18 dataset does not lead to a different ESL curve. Both ESL curves show a reduced sea-level rise rate at 8.2 ka BP (from ~15 m/ka to ~6 m/ka), which corresponds to a Northern Hemisphere cooling event documented by Greenland and Arctic ice core data (Alley et al., 1997). However, this reduced rate of sea-level rise seems contradictory to previous climatic studies that suggest this cooling event is caused by the catastrophic drainage of proglacial lakes Agassiz and Ojibway (Barber et al., 1999) or Laurentide ice saddle collapse (Matero et al., 2017). Possibly, this is because, as mentioned above, our McMC method cannot capture the sea-level variation over a transient period of several centuries. Global sea-level rise rate prior to 8.2 ka event could be smaller than the long-term average rate of ~15 m/ka, which is supported by a climatic study (Törnqvist and Hijma, 2012) which suggests global sea-level rise rate between 8.54-8.20 ka is 3.0 ± 1.2 m and an analysis of sea-level records from Mississippi Delta suggesting global sea-level rose at a rate of 1.5 ± 0.7 from 8.3 to 8.2 ka BP (Li et al., 2012).

Following the final phase of NAIS melting at ~7 ka BP, the rate of sea-level rise dropped to ~1 m/ka at 6.7 ka BP, which lasts until 4.2 ka BP when global mean sea-level was nearly identical to present. Because all other major ice sheets decayed before ~7 ka BP (Figure 3.1), a highly-disputed problem is whether Antarctica can be the reservoir responsible for the ~4 m sea-level rise during the late Holocene. Considering W12 is the only AIS model that predicts no Antarctic contribution to mid-late Holocene sea-level rise, and most of the W12 IHD predictions are lower than the observational constraints at 5 ka BP (Figure S4 d), especially at the highly dynamic Ross Sea sector. Antarctica is likely to contribute at least some of the mid-late Holocene sea-level rise, which is consistent with recent Weddell Sea field observations (Johnson et al., 2019) that shows a significant ice retreating between ~7.5-6 ka BP and far-field sea-level record interpretations (Yokoyama et al., 2019a) that suggests late Holocene sea-level rise is originated from Antarctica and/or Greenland ice sheets.

In this study, we do not attempt to adjust the regional ice-sheet models to follow the new ESL curve in the

last 20 ka since this would require a comprehensive reanalysis for reconciling the ice volume constrained by far-field observations with the ice-sheet volume and geometry constrained by near-field observations. But as illustrated above, the newly-incorporated RSL records have revealed a much more dynamic cryospheric environment during the late glacial period, which is needed to be concerned about while building new ice models. Future work should focus on providing applicable climate-change or ice-sheet dynamic theories for explaining rapid sea-level variations without clear changes shown in oxygen isotope (Johnsen, 1999) and carbon dioxide concentration records and investigating the indications of the discrepancy between the newly-discovered 19.3 ka BP global sea-level minimum with the commonly-used timing (21-20 ka BP) of the LGM.

5.2 Implications on Solid Earth Rheology

By fitting ice model to a more sophisticated taxa-based coral depth-habitat relationships introduced in Hibbert et al. (2016), we find a slightly higher value of best-fitting upper-mantle viscosity for all AIS models (Table 4.1; section 4.4). This is because, in H18, most of the coral taxa show their P_{RSL} at a depth 20-30% shallower than the depth assumed in L14 (see taxa-based coral depth distributions in Hibbert et al., (2018) Figure 3), which can be regarded as systematic errors under the same amount of water load. We show that a $\sim 1.25 \times 10^{20}$ Pa S more viscous upper mantle can effectively balance these systematic errors. However, because currently, the upper-mantle viscosity is poorly-constrained, we are not able to justify whether the more viscous upper mantle revealed by H18 is more accurate than the lower viscosity upper mantle revealed
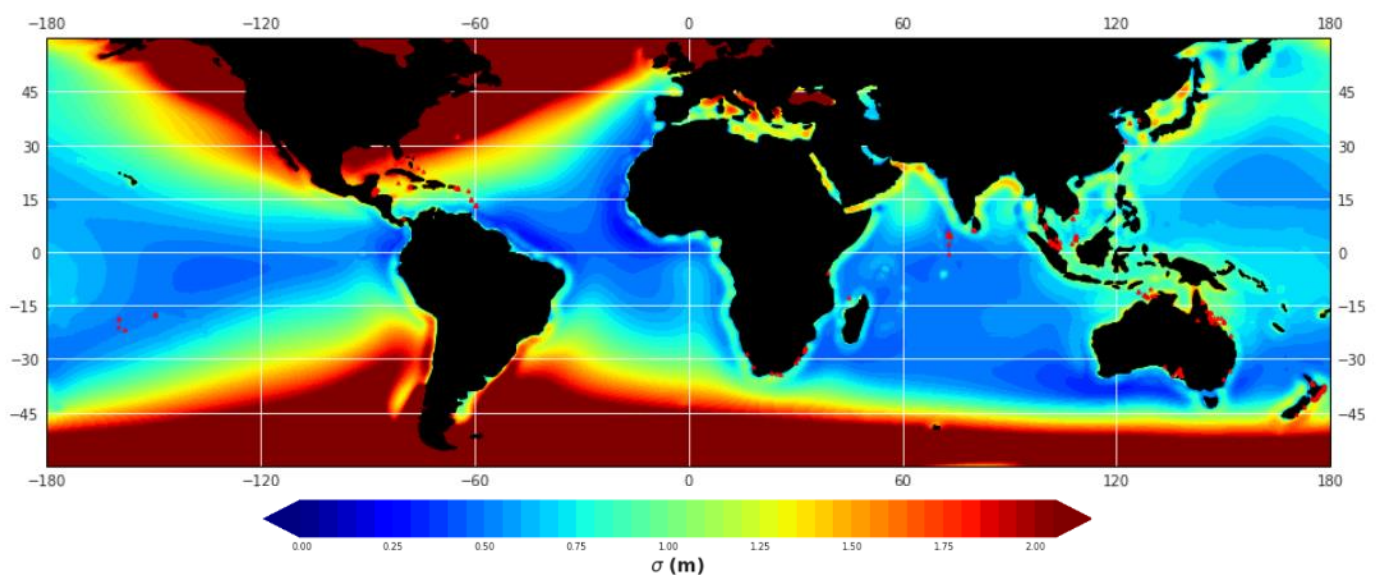
Figure 5.1 A map showing the averaged standard deviation between sea-level predictions by four Antarctic ice sheet models with corresponding best-fitting Earth models between 21 to 8 ka BP. Red dots indicate the observational site incorporated in H18 dataset.

by L14. A similar ambiguity is the different upper-mantle models can also balance the different water load imposed by different AIS models. Therefore, far-field RSL observations show low sensitivities to the Antarctic contribution to post-LGM sea-level rise. This low sensitivity is illustrated in Figure 5.1, in most of the far-field regions, the averaged standard deviation between the sea-level predictions generated by 4 AIS models (with their corresponding best-fitting Earth models) between 21 to 8 ka BP is lower than 1m. Although the intermediate-field regions like Florida and Virgin Islands show a higher sensitivity, the mantle viscosity underneath these regions is complicated due to the transition between continental to oceanic rheology, which is not representative to the rheology of most far-field sites.

In order to improve the understanding of the validity of paleo sea-level reconstruction methods and provide information on whether Antarctica can hold some of the 'missing ice' at the LGM, independent constraints on the upper mantle viscosity beneath continent-ocean margin regions with relatively higher sensitivity on AIS deglaciation history (e.g., South Asia, GBR, Bonaparte Gulf and New Zealand, Figure 5.1), are urgently needed. However, due to the lack of present-day GIA uplift signals (the most direct observations to constrain the upper mantle viscosity), this condition is currently extremely hard to achieve in these mid-to-low latitude regions. Earth interior material properties underneath these regions can only be inferred from seismic imaging and experimental-based studies which are associated with great complexity and uncertainty. Arguably, a possible way to investigate the upper-mantle viscosity is from the analysis of three-dimensional shear wave velocity structure. Although there is no direct physical correspondence between shear velocity and mantle viscosity, laboratory studies suggest the variation in upper mantle viscosity is majorly controlled by temperature (Faul and Jackson, 2005, Hirth and Kohlstedt, 2003), which can be possibly inferred from shear velocity (see an example of formulation in Ivins and Sammis, 1995). Wu et al. (2012) have performed this method in a similar way to provide some meaningful results in Laurentia and Fennoscandia. Similarly, this method has succeeded in inferring the spatial variation in upper mantle viscosity beneath Antarctica (Whitehouse et al., 2019). Thus, future work should focus on applying this method for the regions mentioned above to provide insights on upper mantle viscosity. If the mantle viscosity can be constrained, the method introduced in this study can largely determine the Antarctic contribution to post-LGM sea-level rise and improve the understanding of the 'missing ice' problem. Put simply in words, for the ocean-continent margin and mid-ocean island regions, the more viscous the upper mantle is the more ice Antarctica can hold at the LGM.

5.3 Implications on Antarctic Deglaciation History

Currently, including 4 AIS models adopted in this study, most of Antarctic ice models assume a stable ice volume through the whole late glacial period (i.e., ~25-17 ka BP). However, by analyzing the far-field sea-level observations, we confirm a dynamic cryospheric environment during the late glacial period as proposed by several recent studies (e.g., Carlson et al., 2018, Yokoyama et al., 2018). Unlike ice-sheet retreat, the mechanisms that responsible for an ice-sheet growth spurt has not received enough attention, especially for Antarctica due to the cold and dry geographical environment. But as the solar insolation in Southern Hemisphere showed an increasing trend between ~30-19 ka BP (Huybers, 2006), it is possible for AIS to grow through gaining more snowfall towards the timing of global sea-level minimum at 19.3 ka BP discovered in this study. A recent study of Frieler et al. (2015) proposed a possible mechanism for Antarctica to growth with increasing accumulation during the warm period, which suggests that 1 °C temperature increase in Antarctica will lead to a $5 \pm 1\%$ of the increase in continental-scale ice accumulation rate. Following reconstruction of West Antarctica surface temperature from analysis of deep borehole and ice-
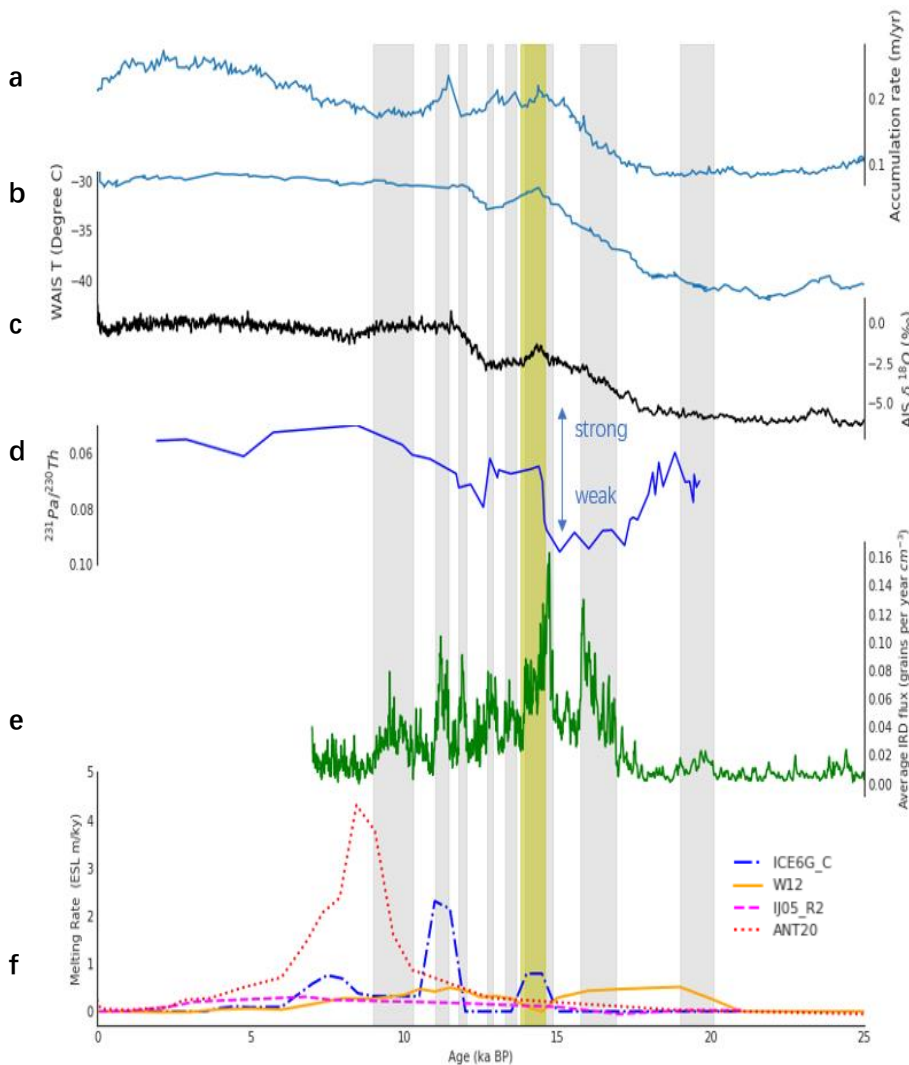
Figure 5.2 Proxy records of oceanic and Antarctic climate change during last deglaciation. (a) Accumulate rate from the West Antarctic Ice Sheet Divide core (Fudge et al., 2016) (b) Reconstructed West Antarctic surface temperature (Cuffey et al., 2016). (c) averaged $\delta^{18}O$ of five Antarctic ice core: EDML, DF, EDC, TAL, WDC (Buizert et al., 2018), (d) Atlantic Meridional Overturning Circulation (AMOC) strength derived from $^{231}Pa/^{230}Th$ ratio from ODP site 1063, 172, 33° 41′ N, 57° 37′ (Böhm et al., 2015). (e) stacked ice-rafted debris (IRD) flux from two core sites: MD07-3133, MD07-3134 (Weber et al., 2014). (f) Ice melting rates calculated for the Weddell Sea and Antarctic Peninsula sectors of each of the four Antarctic ice models based on model drainage system (Zwally et al., 2012). Grey vertical bars are the inferred Antarctic ice discharge events inferred from IRD flux, yellow bar is the duration of MWP-1A discovered in this study.

core data (Figure 5.2 b; Cuffey et al., 2016), West Antarctica reached its lowest surface temperature at ~22 ka BP followed by a period of sustained surface temperature rise of 2 °C until ~20 ka BP. Because temperature is the main factor that determines the ice sheets' regime of ablation or accumulation, an elevated temperature will increase the net accumulation rate at a temperature lower than -15 °C (Oerlemans, 1991). This indicates that it is possible for Antarctica to have an ice-sheet growth during this 2-ka time interval, and hence, Antarctica can responsible for part of the rapid global sea-level drop during between 23 to 19.3 ka BP (Figure 4.8). Restricted by the intensive ice coverage, currently, the most 'direct' paleo observations to Antarctic ice-sheet variation during the Last Deglaciation come from two Scotia Sea ice-rafted debris records (IRD; Weber et al., 2014) that provide a continuous signal of Antarctic ice-sheet dynamic and variability (especially for Weddell Sea and Antarctic Peninsula sectors due to the near location and the direction of Antarctic Circumpolar Current). It is noteworthy that there is a small peak of IRD flux occurred between ~20 to 19 ka BP, which corroborates to the timing of global sea-level minimum. This peak might indicate a warmer, wetter and more dynamic period with a larger rate of ice accumulation/ablation and ice throughflow. As shown in this study, far-field sea-level observations reveal that Antarctica cannot have a significant ice mass loss between 20-15 ka BP. Consequently, it is likely for Antarctica to have a larger accumulation rate (relative to ice ablation rate), which can partly responsible for the global sea-level minimum during this period. But the ambiguity for this inference is the suggested increase in snowfall is not documented in the West Antarctic Ice Sheet Divide core (WDC, Figure 5.2 a; Fudge et al., 2016).

In comparison, the mechanism for AIS to grow between 20 to 15 ka BP is more traceable and appeared to be corroborated by some paleo proxy data. As shown in Figure 5.2 (b), the surface temperature in West Antarctica increased from -42 °C at 20 ka BP to ~-34 °C at 15 ka BP, which led to an approximately doubled ice accumulation rate of 0.4 m/yr at the West Antarctica documented by the WDC (Figure 5.2 a). Meanwhile, a proxy for Atlantic Meridional Overturning Circulation (AMOC) strength (Pa/Th, Figure 5.2 d; Böhm et al., 2015) suggests a slowdown in overturning between ~17 to 15 ka BP, which would result in heat accumulating the in the Southern Ocean (i.e., the bi-polar seesaw mechanism, Broecker, 1991). This slowly heat accumulation can possibly stabilize the Antarctic ice sheets within a relatively short time interval through thinning the ice shelf to reduce buttressing and allow ice shelf acceleration (Greene et al., 2018). Taken together with far-field sea-level analysis, Antarctica should experience a warming and highly dynamic period between ~16.9 to 15.8 ka BP, when IRD flux reached a second-highest value, with no significant ice mass loss. Probably, during this period, the increased ice accumulation rate could enable Antarctica to have a gradual growth, which is in agreement with the prediction of IJ05_R2 (which shows a

slow ice-sheet growth from ~17-16 ka BP, magenta line in Figure 5.2 f). Between ~15.8-14.8 ka BP, the West Antarctic ice accumulation rate reached a high value of ~0.2 m/yr. Combining this with the relatively low IRD deposition (representing the low ice discharge) during this period it is conceivable for AIS to have a growth spurt, which may partly responsible for the global sea-level oscillation before MWP-1A (see Figure 4.8), indicating a good agreement with the far-field sea-level signals.

After ~3-ka period of sustained atmospheric (revealed by a stack of five Antarctic ice-core $\delta^{18}O$ records, Figure 5.2 c) and oceanic warmth (slowdown of AMOC), the Antarctic cryospheric system is likely to attain a threshold at ~14.6 ka BP. Following this threshold, the highest recorded IRD flux occurred at ~14.4 ka BP with no significant increase in ice accumulation rate, which is most likely correspondence to an event of rapid Antarctic ice mass loss. Although the Antarctic contributions to the global sea-level rise during MWP-1A is still debated, climatic modelling studies do provide some plausible mechanisms for Antarctica to melt rapidly during MWP-1A through rapid thermal erosion at ice grounding line (e.g., Golledge et al., 2014). This is in good agreement with our analysis that a larger Antarctic contribution to MWP-1A is preferred by observational sea-level records. In contrast to the identifiable correlation between the IRD flux and ice accumulation rate during MWP-1A, the interpretation of Antarctic contributions to MWP-1B is much more ambiguous due to the lower IRD flux with high ice accumulation rate. In order to have a plausible interpretation of a large Antarctic contribution to MWP-1B, a sophisticated climatic investigation, especially the oceanic effect, is needed, which is out of the scope of this study.

Overall, our results from the far-field sea-level analysis is well-reconciled with some simplified proxy-based interpretations on Antarctic paleoenvironment. However, due to the complicated Antarctic cryospheric system, we cannot consider any ambiguities associated with each proxy such as the possible nonlinear relationship between IRD flux and change in ice thickness (Schoof, 2007). Future studies should explore the possible mechanism for AIS to grow rapidly and find the corresponding field evidence, if it is possible, a late glacial period AIS growth spurt will provide vital clues to close the global sea-level budget.

Chapter 6 Conclusions

The primary objective of this research was to investigate the Antarctic contribution to post-LGM global sea-level rise by comparing different commonly-used Antarctic deglaciation models induced global sea-level variation signatures to the high-quality far-field sea-level datasets. This was achieved by: (*i*) Select the high-quality Antarctic deglaciation models: IJ05_R2, W12, ICE-6G_C, ANT20 (most commonly-used ice models in GIA modelling); (*ii*) Select & Build up high-quality far-field observational RSL datasets: a widely-used L14 dataset and a newly-formed H18 dataset that incorporates most recently published sea-level records based on more sophisticated sea-level reconstruction method; (*iii*) Use GIA modelling approach to remove the isostatic contributions within each RSL record, and McMC algorithm to reconstruct the underlying 'denoised' ESL time series for each observational dataset; (*iv*) Combine each AIS model with the ANU ice model's non-Antarctic part to set up its corresponding global ice model, the total ice volume of which follows the ESL curve obtained above (with 'missing ice' assigned to the North America Ice Sheet); (*v*) Search best-fitting Earth model for each global ice model through forward modelling of ~4500 Earth models to fit either the L14 or H18 dataset; (*vi*) Calculate the global sea-level variation by combining the global ice models with their corresponding best-fitting Earth model for L14 and H18. The conclusions of this research are as follows:

1. Given the best-fitting Earth model, all AIS models selected in this study are able to achieve a relatively good fit with the far-field observations, and hence, showing low sensitivity to Antarctic post-LGM ESL contribution. In order to determine the Antarctic post-LGM ESL contribution, independent constraints on Earth rheology (e.g., from seismic imaging and experimental-based studies) in the regions like the mid-ocean island and continent-ocean margin (e.g., from seismic imaging and experimental-based studies), are urgently needed.

2. Far-field sea-level observations are more sensitive to the discrepancy in the ice melting rates between different AIS models. By comparing different AIS models' χ^2 misfit in some specific periods, far-field sea-level observations are able to provide some critical information on the validity of Antarctic deglaciation history. Examples are the considerably higher χ^2 misfit produced by W12 compared to both observational sea-level datasets indicates the significant ice mass loss predicted by W12 during ~20-15 ka is most likely incorrect, thus, during this time interval, Antarctica cannot make a significant contribution to the global sea-level rise. As well as during ~15-11 ka BP, far-field sea-level records

shows a preference with ICE-6G_C, which is the only model with a distinct contribution to MWP-1A and MWP-1B, showing good consistency with the much more dynamic cryospheric environment revealed by the new global ice volume history reconstruced from the H18 dataset.

3. In general, IJ05_R2 and ANT20 model achieve the best fit to the L14 and H18 datasets, but due to the gradual ice sheet variation trend predicted by these two models, far-field sea-level records cannot yield distinct indications of the best-fit of these two models.

4. Currently, there is no consensus on whether the taxa-based sea-level reconstruction method adopted in the H18 dataset can be used in GIA modelling. We made the first attempt to adopt this methodology in GIA modelling study and confirmed the validity of this method by producing some meaningful results.

5. Due to the incorporation of the recent far-field sea-level observational records from Great Barrier Reef, the H18-based newly-reconstructed ESL curve illustrates a much more dynamic cryospheric environment during the late glacial period of ~25-15 ka BP.

6. Taken together with the more dynamic Antarctic cryosphere with the proxy-based interpretation of Antarctic paleoclimate, it is possible for Antarctica to have one or more growth spurt during ~22 to 15 ka BP. But to confirm this inference, a plausible mechanism and corresponding Antarctic field evidence are required.

References

ABDUL, N., MORTLOCK, R., WRIGHT, J. & FAIRBANKS, R. 2016. Younger Dryas sea level and meltwater pulse 1B recorded in Barbados reef crest coral Acropora palmata. *Paleoceanography,* 31, 330-344.

ADHIKARI, S., IVINS, E. R., LAROUR, E., SEROUSSI, H., MORLIGHEM, M. & NOWICKI, S. 2014. Future Antarctic bed topography and its implications for ice sheet dynamics. *Solid Earth,* 5, 569-584.

AGASSIZ, L. 1840. Études sur les glaciers: Neuchâtel. *Jent et Gassmann, Soleure,* 144-146.

ALLEY, R. B., MAYEWSKI, P. A., SOWERS, T., STUIVER, M., TAYLOR, K. C. & CLARK, P. U. 1997. Holocene climatic instability: A prominent, widespread event 8200 yr ago. *Geology,* 25, 483-486.

ANDERSON, J. B., CONWAY, H., BART, P. J., WITUS, A. E., GREENWOOD, S. L., MCKAY, R. M., HALL, B. L., ACKERT, R. P., LICHT, K. & JAKOBSSON, M. 2014. Ross Sea paleo-ice sheet drainage and deglacial history during and since the LGM. *Quaternary Science Reviews,* 100, 31-54.

ANDREWS, J. T. 1992. A case of missing water. *Nature,* 358, 281.

ARGUS, D. F., PELTIER, W., DRUMMOND, R. & MOORE, A. W. 2014. The Antarctica component of postglacial rebound model ICE-6G_C (VM5a) based on GPS positioning, exposure age dating of ice thicknesses, and relative sea level histories. *Geophysical Journal International,* 198, 537-563.

BARBER, D. C., DYKE, A., HILLAIRE-MARCEL, C., JENNINGS, A. E., ANDREWS, J. T., KERWIN, M. W., BILODEAU, G., MCNEELY, R., SOUTHON, J. & MOREHEAD, M. D. 1999. Forcing of the cold event of 8,200 years ago by catastrophic drainage of Laurentide lakes. *Nature,* 400, 344.

BARD, E., HAMELIN, B., ARNOLD, M., MONTAGGIONI, L., CABIOCH, G., FAURE, G. & ROUGERIE, F. 1996. Deglacial sea-level record from Tahiti corals and the timing of global meltwater discharge. *Nature,* 382, 241.

BARD, E., HAMELIN, B. & DELANGHE-SABATIER, D. 2010. Deglacial meltwater pulse 1B and Younger Dryas sea levels revisited with boreholes at Tahiti. *Science,* 327, 1235-1237.

BARD, E., HAMELIN, B., FAIRBANKS, R. G. & ZINDLER, A. 1990. Calibration of the 14C timescale over the past 30,000 years using mass spectrometric U–Th ages from Barbados corals. *Nature,* 345, 405.

BARLETTA, V. R., BEVIS, M., SMITH, B. E., WILSON, T., BROWN, A., BORDONI, A., WILLIS, M., KHAN, S. A., ROVIRA-NAVARRO, M. & DALZIEL, I. 2018. Observed rapid bedrock uplift in Amundsen Sea Embayment promotes ice-sheet stability. *Science,* 360, 1335-1339.

BARR, I. D. & CLARK, C. D. 2011. Glaciers and climate in Pacific far NE Russia during the last glacial maximum. *Journal of Quaternary Science,* 26, 227-237.

BASSETT, S., MILNE, G., BENTLEY, M. & HUYBRECHTS, P. 2007. Modelling Antarctic sea-level data to explore the possibility of a dominant Antarctic contribution to meltwater pulse IA. *Quaternary Science Reviews,* 26, 2113-2127.

BENTLEY, M. J., COFAIGH, C. O., ANDERSON, J. B., CONWAY, H., DAVIES, B., GRAHAM, A. G., HILLENBRAND, C.-D., HODGSON, D. A., JAMIESON, S. S. & LARTER, R. D. 2014. A community-based geological reconstruction of Antarctic Ice Sheet deglaciation since the Last Glacial Maximum. *Quaternary Science Reviews,* 100, 1-9.

BENTLEY, M. J., FOGWILL, C. J., LE BROCQ, A. M., HUBBARD, A. L., SUGDEN, D. E., DUNAI, T. J. & FREEMAN, S. P. 2010. Deglacial history of the West Antarctic Ice Sheet in the Weddell Sea embayment: Constraints on past ice volume change. *Geology,* 38, 411-414.

BLANCHON, P. & SHAW, J. 1995. Reef drowning during the last deglaciation: evidence for catastrophic sea-level rise and ice-sheet collapse. *Geology,* 23, 4-8.

BOCKHEIM, J. G., WILSON, S. C., DENTON, G. H., ANDERSEN, B. G. & STUIVER, M. 1989. Late quaternary ice-surface fluctuations of Hatherton Glacier, Transantarctic Mountains. *Quaternary Research,* 31, 229-254.

BöHM, E., LIPPOLD, J., GUTJAHR, M., FRANK, M., BLASER, P., ANTZ, B., FOHLMEISTER, J., FRANK, N., ANDERSEN, M. & DEININGER, M. 2015. Strong and deep Atlantic meridional overturning circulation during the last glacial cycle. *Nature,* 517, 73.

BRIGHAM-GRETTE, J., GUALTIERI, L. M., GLUSHKOVA, O. Y., HAMILTON, T. D., MOSTOLLER, D. & KOTOV, A. 2003. Chlorine-36 and 14C chronology support a limited last glacial maximum across central Chukotka, northeastern Siberia, and no Beringian ice sheet. *Quaternary Research,* 59, 386-398.

BROECKER, W. S. 1991. The great ocean conveyor. *Oceanography,* 4, 79-89.

BUIZERT, C., SIGL, M., SEVERI, M., MARKLE, B. R., WETTSTEIN, J. J., MCCONNELL, J. R., PEDRO, J. B., SODEMANN, H., GOTO-AZUMA, K. & KAWAMURA, K. 2018. Abrupt ice-age shifts in southern westerly winds and Antarctic climate forced from the north. *Nature,* 563**,** 681.

CARLSON, A. E. & CLARK, P. U. 2012. Ice sheet sources of sea level rise and freshwater discharge during the last deglaciation. *Reviews of Geophysics,* 50.

CARLSON, A. E., DUTTON, A., LONG, A. J. & MILNE, G. A. 2019. PALeo constraints on SEA level rise (PALSEA): Ice-sheet and sea-level responses to past climate warming. *Quaternary Science Reviews,* 212**,** 28-32.

CARLSON, A. E., TARASOV, L. & PICO, T. 2018. Rapid Laurentide ice-sheet advance towards southern last glacial maximum limit during marine isotope stage 3. *Quaternary Science Reviews,* 196**,** 118-123.

CARON, L., MéTIVIER, L., GREFF-LEFFTZ, M., FLEITOUT, L. & ROUBY, H. 2017. Inverting Glacial Isostatic Adjustment signal using Bayesian framework and two linearly relaxing rheologies. *Geophysical Journal International,* 209**,** 1126-1147.

CELSIUS, A. 1743. Anmärkning om vatnets förminskande så i Östersiön som Vesterhafvet, Kongl. *Swenska Wetenskaps Academiens Handlingar,* 4**,** 33–50.

CHENG, H., EDWARDS, R. L., SHEN, C.-C., POLYAK, V. J., ASMEROM, Y., WOODHEAD, J., HELLSTROM, J., WANG, Y., KONG, X. & SPöTL, C. 2013. Improvements in 230Th dating, 230Th and 234U half-life values, and U–Th isotopic measurements by multi-collector inductively coupled plasma mass spectrometry. *Earth and Planetary Science Letters,* 371**,** 82-91.

CHINA, N. 2018. Typhoon Mangkhut has caused 5.2 billion RMB economic loss. *Beijing Youth Daily*, 19 September 2018.

CLARK, P. U., DYKE, A. S., SHAKUN, J. D., CARLSON, A. E., CLARK, J., WOHLFARTH, B., MITROVICA, J. X., HOSTETLER, S. W. & MCCABE, A. M. 2009. The last glacial maximum. *science,* 325**,** 710-714.

CLARK, P. U., MITROVICA, J., MILNE, G. & TAMISIEA, M. 2002. Sea-level fingerprinting as a direct test for the source of global meltwater pulse IA. *Science,* 295**,** 2438-2441.

CLARK, P. U. & TARASOV, L. 2014. Closing the sea level budget at the Last Glacial Maximum. *Proceedings of the National Academy of Sciences,* 111**,** 15861-15862.

COLHOUN, E., MABIN, M., ADAMSON, D. & KIRK, R. 1992. Antarctic ice volume and contribution to sea-level fall at 20,000 yr BP from raised beaches. *Nature,* 358**,** 316.

CRONIN, T. M. 1999. *Principles of paleoclimatology*, Columbia University Press.

CRONIN, T. M., VOGT, P., WILLARD, D., THUNELL, R., HALKA, J., BERKE, M. & POHLMAN, J. 2007. Rapid sea level rise and ice sheet response to 8,200-year climate event. *Geophysical Research Letters,* 34.

CUFFEY, K. & PATERSON, W. 2010. The physics of glaciers, xii, 693 pp. Butterworth-Heinemann/Elsevier, Amsterdam, the Netherlands, Boston, USA.

CUFFEY, K. M., CLOW, G. D., STEIG, E. J., BUIZERT, C., FUDGE, T., KOUTNIK, M., WADDINGTON, E. D., ALLEY, R. B. & SEVERINGHAUS, J. P. 2016. Deglacial temperature history of West Antarctica. *Proceedings of the National Academy of Sciences,* 113**,** 14249-14254.

DE BOER, B., STOCCHI, P. & VAN DE WAL, R. 2014. A fully coupled 3-D ice-sheet-sea-level model: algorithm and applications. *Geoscientific Model Development,* 7**,** 2141-2156.

DE BOER, B., STOCCHI, P., WHITEHOUSE, P. L. & VAN DE WAL, R. S. 2017. Current state and future perspectives on coupled ice-sheet–sea-level modelling. *Quaternary Science Reviews,* 169**,** 13-28.

DE GEER, G. 1896. Om Skandinaviens geografiska utveckling efter istiden.

DENISON, D. G., HOLMES, C. C., MALLICK, B. K. & SMITH, A. F. 2002. *Bayesian methods for nonlinear classification and regression*, John Wiley & Sons.

DENTON, G. H. 1991. Cainozoic history of the Antarctic ice sheet. *Geology of Antarctica***,** 365-433.

DENTON, G. H. & HUGHES, T. J. 2002. Reconstructing the Antarctic ice sheet at the Last Glacial Maximum. *Quaternary Science Reviews,* 21**,** 193-202.

DESCHAMPS, P., DURAND, N., BARD, E., HAMELIN, B., CAMOIN, G., THOMAS, A. L., HENDERSON, G. M., OKUNO, J. I. & YOKOYAMA, Y. 2012. Ice-sheet collapse and sea-level rise at the Bølling warming 14,600 years ago. *Nature,* 483**,** 559.

DZIEWONSKI, A. M. & ANDERSON, D. L. 1981. Preliminary reference Earth model. *Physics of the earth and planetary interiors,* 25**,** 297-356.

EATON, D. W., DARBYSHIRE, F., EVANS, R. L., GRüTTER, H., JONES, A. G. & YUAN, X. 2009. The elusive lithosphere–

asthenosphere boundary (LAB) beneath cratons. *Lithos,* 109**,** 1-22.

EKMAN, M. 2009. *The changing level of the Baltic Sea during 300 years: a clue to understanding the Earth*, Summer Institute for Historical Geophysics Åland Islands.

EVANS, E. P. 1887. The authorship of the glacial theory. *The North American Review,* 145**,** 94-97.

FAIRBANKS, R. G. 1989. A 17,000-year glacio-eustatic sea level record: influence of glacial melting rates on the Younger Dryas event and deep-ocean circulation. *Nature,* 342**,** 637.

FAIRBANKS, R. G., MORTLOCK, R. A., CHIU, T.-C., CAO, L., KAPLAN, A., GUILDERSON, T. P., FAIRBANKS, T. W., BLOOM, A. L., GROOTES, P. M. & NADEAU, M.-J. 2005. Radiocarbon calibration curve spanning 0 to 50,000 years BP based on paired 230Th/234U/238U and 14C dates on pristine corals. *Quaternary Science Reviews,* 24, 1781-1796.

FARRELL, W. & CLARK, J. A. 1976. On postglacial sea level. *Geophysical Journal of the Royal Astronomical Society,* 46**,** 647-667.

FAUL, U. H. & JACKSON, I. 2005. The seismological signature of temperature and grain size variations in the upper mantle. *Earth and Planetary Science Letters,* 234**,** 119-134.

FRIELER, K., CLARK, P. U., HE, F., BUIZERT, C., REESE, R., LIGTENBERG, S. R., VAN DEN BROEKE, M. R., WINKELMANN, R. & LEVERMANN, A. 2015. Consistent evidence of increasing Antarctic accumulation with warming. *Nature Climate Change,* 5**,** 348.

FUDGE, T., MARKLE, B. R., CUFFEY, K. M., BUIZERT, C., TAYLOR, K. C., STEIG, E. J., WADDINGTON, E. D., CONWAY, H. & KOUTNIK, M. 2016. Variable relationship between accumulation and temperature in West Antarctica for the past 31,000 years. *Geophysical Research Letters,* 43, 3795-3803.

GALLAGHER, K., BODIN, T., SAMBRIDGE, M., WEISS, D., KYLANDER, M. & LARGE, D. 2011. Inference of abrupt changes in noisy geochemical records using transdimensional changepoint models. *Earth and Planetary Science Letters,* 311**,** 182-194.

GALLAGHER, K., CHARVIN, K., NIELSEN, S., SAMBRIDGE, M. & STEPHENSON, J. 2009. Markov chain Monte Carlo (MCMC) sampling methods to determine optimal models, model resolution and model choice for Earth Science problems. *Marine and Petroleum Geology,* 26**,** 525-535.

GOLLEDGE, N., MENVIEL, L., CARTER, L., FOGWILL, C., ENGLAND, M., CORTESE, G. & LEVY, R. 2014. Antarctic contribution to meltwater pulse 1A from reduced Southern Ocean overturning. *Nature communications,* 5**,** 5107.

GOMEZ, N., LATYCHEV, K. & POLLARD, D. 2018. A Coupled Ice Sheet–Sea Level Model Incorporating 3D Earth Structure: Variations in Antarctica during the Last Deglacial Retreat. *Journal of Climate,* 31**,** 4041-4054.

GOMEZ, N., POLLARD, D. & MITROVICA, J. X. 2013. A 3-D coupled ice sheet–sea level model applied to Antarctica through the last 40 ky. *Earth and Planetary Science Letters,* 384**,** 88-99.

GOWAN, E. J., TREGONING, P., PURCELL, A., MONTILLET, J.-P. & MCCLUSKY, S. 2016. A model of the western Laurentide Ice Sheet, using observations of glacial isostatic adjustment. *Quaternary Science Reviews,* 139**,** 1-16.

GREENE, C. A., YOUNG, D. A., GWYTHER, D. E., GALTON-FENZI, B. K. & BLANKENSHIP, D. D. 2018. Seasonal dynamics of Totten Ice Shelf controlled by sea ice buttressing. *Cryosphere,* 12**,** 2869-2882.

GREGOIRE, L. J., PAYNE, A. J. & VALDES, P. J. 2012. Deglacial rapid sea level rises caused by ice-sheet saddle collapses. *Nature,* 487**,** 219.

GROUSSET, F. E., PUJOL, C., LABEYRIE, L., AUFFRET, G. & BOELAERT, A. 2000. Were the North Atlantic Heinrich events triggered by the behavior of the European ice sheets? *Geology,* 28**,** 123-126.

HALL, B. L. & DENTON, G. H. 1999. New relative sea-level curves for the southern Scott Coast, Antarctica: evidence for Holocene deglaciation of the western Ross Sea. *Journal of Quaternary Science,* 14**,** 641-650.

HALL, B. L., DENTON, G. H. & OVERTURF, B. 2001. Glacial Lake Wright, a high-level Antarctic lake during the LGM and early Holocene. *Antarctic Science,* 13**,** 53-60.

HANEBUTH, T., STATTEGGER, K. & BOJANOWSKI, A. 2009. Termination of the Last Glacial Maximum sea-level lowstand: The Sunda-Shelf data revisited. *Global and Planetary Change,* 66**,** 76-84.

HANEBUTH, T., STATTEGGER, K. & GROOTES, P. M. 2000. Rapid flooding of the Sunda Shelf: a late-glacial sea-level record. *Science,* 288**,** 1033-1035.

HASKELL, N. 1935. The motion of a viscous fluid under a surface load. *Physics,* 6**,** 265-269.

HASTINGS, W. K. 1970. Monte Carlo sampling methods using Markov chains and their applications.

HIBBERT, F., WILLIAMS, F., FALLON, S. & ROHLING, E. 2018. A database of biological and geomorphological sea-level

markers from the Last Glacial Maximum to present. *Scientific data,* 5**,** 180088.

HIBBERT, F. D., ROHLING, E. J., DUTTON, A., WILLIAMS, F. H., CHUTCHARAVAN, P. M., ZHAO, C. & TAMISIEA, M. E. 2016. Coral indicators of past sea-level change: A global repository of U-series dated benchmarks. *Quaternary Science Reviews,* 145**,** 1-56.

HILLENBRAND, C.-D., BENTLEY, M. J., STOLLDORF, T. D., HEIN, A. S., KUHN, G., GRAHAM, A. G., FOGWILL, C. J., KRISTOFFERSEN, Y., SMITH, J. A. & ANDERSON, J. B. 2014. Reconstruction of changes in the Weddell Sea sector of the Antarctic Ice Sheet since the Last Glacial Maximum. *Quaternary Science Reviews,* 100**,** 111-136.

HILLENBRAND, C.-D., MELLES, M., KUHN, G. & LARTER, R. D. 2012. Marine geological constraints for the grounding-line position of the Antarctic Ice Sheet on the southern Weddell Sea shelf at the Last Glacial Maximum. *Quaternary Science Reviews,* 32**,** 25-47.

HILLER, A., WAND, U., KäMPF, H. & STACKEBRANDT, W. 1988. Occupation of the Antarctic continent by petrels during the past 35 000 years: inferences from a 14 C study of stomach oil deposits. *Polar Biology,* 9**,** 69-77.

HIRTH, G. & KOHLSTEDT, D. 2003. Rheology of the upper mantle and the mantle wedge: A view from the experimentalists. *Inside the subduction Factory***,** 83-105.

HUGHES, A. L., GYLLENCREUTZ, R., LOHNE, Ø. S., MANGERUD, J. & SVENDSEN, J. I. 2016. The last Eurasian ice sheets–a chronological database and time-slice reconstruction, DATED-1. *Boreas,* 45**,** 1-45.

HUYBERS, P. 2006. Early Pleistocene glacial cycles and the integrated summer insolation forcing. *science,* 313**,** 508-511.

ISHIWA, T., YOKOYAMA, Y., MIYAIRI, Y., OBROCHTA, S., SASAKI, T., KITAMURA, A., SUZUKI, A., IKEHARA, M., IKEHARA, K. & KIMOTO, K. 2016. Reappraisal of sea-level lowstand during the Last Glacial Maximum observed in the Bonaparte Gulf sediments, northwestern Australia. *Quaternary International,* 397**,** 373-379.

ISHIWA, T., YOKOYAMA, Y., OKUNO, J. I., OBROCHTA, S., UEHARA, K., IKEHARA, M. & MIYAIRI, Y. 2019. A sea-level plateau preceding the Marine Isotope Stage 2 minima revealed by Australian sediments. *Scientific reports,* 9**,** 6449.

IVINS, E. R. & JAMES, T. S. 2005. Antarctic glacial isostatic adjustment: a new assessment. *Antarctic Science,* 17**,** 541-553.

IVINS, E. R., JAMES, T. S., WAHR, J., O. SCHRAMA, E. J., LANDERER, F. W. & SIMON, K. M. 2013. Antarctic contribution to sea level rise observed by GRACE with improved GIA correction. *Journal of Geophysical Research: Solid Earth,* 118**,** 3126-3141.

IVINS, E. R. & SAMMIS, C. G. 1995. On lateral viscosity contrast in the mantle and the rheology of low-frequency geodynamics. *Geophysical Journal International,* 123**,** 305-322.

JAKOBSSON, M., ANDREASSEN, K., BJARNADOTTIR, L. R., DOVE, D., DOWDESWELL, J. A., ENGLAND, J. H., FUNDER, S., HOGAN, K., INGOLFSSON, O. & JENNINGS, A. 2014. Arctic Ocean glacial history. *Quaternary Science Reviews,* 92**,** 40-67.

JAMIESON, T. F. 1865. On the history of the last geological changes in Scotland. *Quarterly Journal of the Geological Society,* 21**,** 161-204.

JOHNSEN, S. 1999. GRIP Oxygen Isotopes. *PANGAEA, doi,* 10.

JOHNSON, J. S., NICHOLS, K. A., GOEHRING, B. M., BALCO, G. & SCHAEFER, J. M. 2019. Abrupt mid-Holocene ice loss in the western Weddell Sea Embayment of Antarctica. *Earth and Planetary Science Letters,* 518**,** 127-135.

JOHNSTON, P. 1993. The effect of spatially non-uniform water loads on prediction of sea-level change. *Geophysical Journal International,* 114**,** 615-634.

KENDALL, R. A., MITROVICA, J. X. & MILNE, G. A. 2005. On post-glacial sea level–II. Numerical formulation and comparative results on spherically symmetric models. *Geophysical Journal International,* 161**,** 679-706.

KIM, J.-M. & KENNETT, J. P. 1998. Paleoenvironmental changes associated with the Holocene marine transgression, Yellow Sea (Hwanghae). *Marine Micropaleontology,* 34**,** 71-89.

LAMBECK, K. 1980. The Earth's Variable Rotation: Geophysical Causes and Consequences, 449 pp. Cambridge University Press, New York.

LAMBECK, K. 1993a. Glacial rebound of the British Isles—I. Preliminary model results. *Geophysical Journal International,* 115**,** 941-959.

LAMBECK, K. 1993b. Glacial rebound of the British Isles—II. A high-resolution, high-precision model. *Geophysical Journal International,* 115**,** 960-990.

LAMBECK, K., JOHNSTON, P., SMITHER, C. & NAKADA, M. 1996. Glacial rebound of the British Isles—III. Constraints on mantle viscosity. *Geophysical Journal International,* 125**,** 340-354.

LAMBECK, K. & NAKADA, M. 1990. Late Pleistocene and Holocene sea-level change along the Australian coast. *Palaeogeography, Palaeoclimatology, Palaeoecology,* 89, 143-176.

LAMBECK, K., PURCELL, A., FUNDER, S., KJæR, K. H., LARSEN, E. & MOLLER, P. 2006. Constraints on the Late Saalian to early Middle Weichselian ice sheet of Eurasia from field data and rebound modelling. *Boreas,* 35, 539-575.

LAMBECK, K., PURCELL, A., JOHNSTON, P., NAKADA, M. & YOKOYAMA, Y. 2003. Water-load definition in the glacio-hydro-isostatic sea-level equation. *Quaternary Science Reviews,* 22, 309-318.

LAMBECK, K., PURCELL, A. & ZHAO, S. 2017. The North American Late Wisconsin ice sheet and mantle viscosity from glacial rebound analyses. *Quaternary Science Reviews,* 158, 172-210.

LAMBECK, K., ROUBY, H., PURCELL, A., SUN, Y. & SAMBRIDGE, M. 2014. Sea level and global ice volumes from the Last Glacial Maximum to the Holocene. *Proceedings of the National Academy of Sciences,* 111, 15296-15303.

LAU, H., AUSTERMANN, J., MITROVICA, J., CRAWFORD, O., AL-ATTAR, D. & LATYCHEV, K. 2018. Inferences of Mantle Viscosity Based on Ice Age Data Sets: The Bias in Radial Viscosity Profiles Due to the Neglect of Laterally Heterogeneous Viscosity Structure. *Journal of Geophysical Research: Solid Earth,* 123, 7237-7252.

LI, T., WU, P., STEFFEN, H. & WANG, H. 2018. In search of laterally heterogeneous viscosity models of glacial isostatic adjustment with the ICE-6G_C global ice history model. *Geophysical Journal International,* 214, 1191-1205.

LI, Y.-X., TöRNQVIST, T. E., NEVITT, J. M. & KOHL, B. 2012. Synchronizing a sea-level jump, final Lake Agassiz drainage, and abrupt cooling 8200 years ago. *Earth and Planetary Science Letters,* 315, 41-50.

LIU, J., SAITO, Y., KONG, X., WANG, H., XIANG, L., WEN, C. & NAKASHIMA, R. 2010. Sedimentary record of environmental evolution off the Yangtze River estuary, East China Sea, during the last~ 13,000 years, with special reference to the influence of the Yellow River on the Yangtze River delta during the last 600 years. *Quaternary Science Reviews,* 29, 2424-2438.

LIU, J. P., MILLIMAN, J. D., GAO, S. & CHENG, P. 2004. Holocene development of the Yellow River's subaqueous delta, North Yellow Sea. *Marine geology,* 209, 45-67.

LLOYD, A. J. 2018. Seismic Tomography of Antarctica and the Southern Oceans: Regional and Continental Models from the Upper Mantle to the Transition Zone.

MACKINTOSH, A. N., VERLEYEN, E., O'BRIEN, P. E., WHITE, D. A., JONES, R. S., MCKAY, R., DUNBAR, R., GORE, D. B., FINK, D. & POST, A. L. 2014. Retreat history of the East Antarctic Ice Sheet since the last glacial maximum. *Quaternary Science Reviews,* 100, 10-30.

MARCOTT, S. A., CLARK, P. U., PADMAN, L., KLINKHAMMER, G. P., SPRINGER, S. R., LIU, Z., OTTO-BLIESNER, B. L., CARLSON, A. E., UNGERER, A. & PADMAN, J. 2011. Ice-shelf collapse from subsurface warming as a trigger for Heinrich events. *Proceedings of the National Academy of Sciences,* 108, 13415-13419.

MARTíN-ESPAñOL, A., KING, M. A., ZAMMIT-MANGION, A., ANDREWS, S. B., MOORE, P. & BAMBER, J. L. 2016. An assessment of forward and inverse GIA solutions for Antarctica. *Journal of Geophysical Research: Solid Earth,* 121, 6947-6965.

MARTINEC, Z., KLEMANN, V., VAN DER WAL, W., RIVA, R., SPADA, G., SUN, Y., MELINI, D., KACHUCK, S., BARLETTA, V. & SIMON, K. 2018. A benchmark study of numerical implementations of the sea level equation in GIA modelling. *Geophysical Journal International,* 215, 389-414.

MATERO, I., GREGOIRE, L., IVANOVIC, R., TINDALL, J. & HAYWOOD, A. 2017. The 8.2 ka cooling event caused by Laurentide ice saddle collapse. *Earth and Planetary Science Letters,* 473, 205-214.

MCCONNELL, R. K. 1968. Viscosity of the mantle from relaxation time spectra of isostatic adjustment. *Journal of Geophysical Research,* 73, 7089-7105.

MCKAY, N. P., OVERPECK, J. T. & OTTO-BLIESNER, B. L. 2011. The role of ocean thermal expansion in Last Interglacial sea level rise. *Geophysical Research Letters,* 38.

MENVIEL, L., TIMMERMANN, A., TIMM, O. E. & MOUCHET, A. 2011. Deconstructing the Last Glacial termination: the role of millennial and orbital-scale forcings. *Quaternary Science Reviews,* 30, 1155-1172.

METROPOLIS, N., ROSENBLUTH, A. W., ROSENBLUTH, M. N., TELLER, A. H. & TELLER, E. 1953. Equation of state calculations by fast computing machines. *The journal of chemical physics,* 21, 1087-1092.

MICHELLI, M. 2008. *Sea-level changes evolution and paleoceanography of coastal waters in SE-Vietnam since the mid-Holocene.* Christian-Albrechts Universität Kiel.

MILNE, G. A., DAVIS, J. L., MITROVICA, J. X., SCHERNECK, H.-G., JOHANSSON, J. M., VERMEER, M. & KOIVULA, H. 2001. Space-geodetic constraints on glacial isostatic adjustment in Fennoscandia. *Science,* 291, 2381-2385.

MILNE, G. A. & MITROVICA, J. X. 1996. Postglacial sea-level change on a rotating Earth: first results from a gravitationally self-consistent sea-level equation. *Geophysical Journal International,* 126**,** F13-F20.

MILNE, G. A. & MITROVICA, J. X. 1998. Postglacial sea-level change on a rotating Earth. *Geophysical Journal International,* 133**,** 1-19.

MITROVICA, J. & FORTE, A. 2004. A new inference of mantle viscosity based upon joint inversion of convection and glacial isostatic adjustment data. *Earth and Planetary Science Letters,* 225**,** 177-189.

MITROVICA, J. & MILNE, G. 2002. On the origin of late Holocene sea-level highstands within equatorial ocean basins. *Quaternary Science Reviews,* 21**,** 2179-2190.

MITROVICA, J. X. & WAHR, J. 2011. Ice age Earth rotation. *Annual Review of Earth and Planetary Sciences,* 39**,** 577-616.

MITROVICA, J. X., WAHR, J., MATSUYAMA, I. & PAULSON, A. 2005. The rotational stability of an ice-age earth. *Geophysical Journal International,* 161**,** 491-506.

MONACCI, N. M., MEIER-GRüNHAGEN, U., FINNEY, B. P., BEHLING, H. & WOOLLER, M. J. 2009. Mangrove ecosystem changes during the Holocene at Spanish lookout Cay, Belize. *Palaeogeography, Palaeoclimatology, Palaeoecology,* 280**,** 37-46.

MORELLI, A. & DANESI, S. 2004. Seismological imaging of the Antarctic continental lithosphere: a review. *Global and Planetary Change,* 42**,** 155-165.

MURRAY-WALLACE, C. V. & WOODROFFE, C. D. 2014. *Quaternary sea-level changes: a global perspective*, Cambridge University Press.

NAKADA, M., KIMURA, R., OKUNO, J., MORIWAKI, K., MIURA, H. & MAEMOKU, H. 2000. Late Pleistocene and Holocene melting history of the Antarctic ice sheet derived from sea-level variations. *Marine Geology,* 167**,** 85-103.

NAKADA, M., OKUNO, J. I. & IRIE, Y. 2017. Inference of viscosity jump at 670 km depth and lower mantle viscosity structure from GIA observations. *Geophysical Journal International,* 212**,** 2206-2225.

NANSEN, F. 1921. *The strandflat and isostasy*, I kommission hos J. Dybwad.

NICHOLAS, W., NICHOL, S., HOWARD, F., PICARD, K., DULFER, H., RADKE, L., CARROLL, A., TRAN, M. & SIWABESSY, P. 2014. Pockmark development in the Petrel Sub-basin, Timor Sea, Northern Australia: Seabed habitat mapping in support of CO2 storage assessments. *Continental Shelf Research,* 83**,** 129-142.

NIELD, G. A. 2014. The effect of late holocene ice-mass changes on glacial isostatic adjustment in West Antarctica.

NIELD, G. A., WHITEHOUSE, P. L., KING, M. A., CLARKE, P. J. & BENTLEY, M. J. 2012. Increased ice loading in the Antarctic Peninsula since the 1850s and its effect on glacial isostatic adjustment. *Geophysical Research Letters,* 39.

NIELD, G. A., WHITEHOUSE, P. L., VAN DER WAL, W., BLANK, B., O'DONNELL, J. P. & STUART, G. W. 2018. The impact of lateral variations in lithospheric thickness on glacial isostatic adjustment in West Antarctica. *Geophysical Journal International,* 214**,** 811-824.

NIESSEN, F., HONG, J. K., HEGEWALD, A., MATTHIESSEN, J., STEIN, R., KIM, H., KIM, S., JENSEN, L., JOKAT, W. & NAM, S.-I. 2013. Repeated Pleistocene glaciation of the East Siberian continental margin. *Nature Geoscience,* 6**,** 842.

OERLEMANS, J. 1991. The role of ice sheets in the Pleistocene climate. *Norsk Geologisk Tidsskrift,* 71**,** 155-161.

OTA, Y., HULL, A. G. & BERRYMAN, K. R. 1991. Coseismic uplift of Holocene marine terraces in the Pakarae River area, eastern North Island, New Zealand. *Quaternary Research,* 35**,** 331-346.

PARRENIN, F., BARNOLA, J.-M., BEER, J., BLUNIER, T., CASTELLANO, E., CHAPPELLAZ, J., DREYFUS, G., FISCHER, H., FUJITA, S. & JOUZEL, J. 2007. The EDC3 chronology for the EPICA Dome C ice core. *Climate of the Past,* 3**,** 485-497.

PELTIER, W. 1974. The impulse response of a Maxwell Earth. *Reviews of Geophysics,* 12**,** 649-669.

PELTIER, W. 2004. Global glacial isostasy and the surface of the ice-age Earth: the ICE-5G (VM2) model and GRACE. *Annu. Rev. Earth Planet. Sci.,* 32**,** 111-149.

PELTIER, W., ARGUS, D. & DRUMMOND, R. 2015. Space geodesy constrains ice age terminal deglaciation: The global ICE-6G_C (VM5a) model. *Journal of Geophysical Research: Solid Earth,* 120**,** 450-487.

PELTIER, W. & FAIRBANKS, R. G. 2006. Global glacial ice volume and Last Glacial Maximum duration from an extended Barbados sea level record. *Quaternary Science Reviews,* 25**,** 3322-3337.

PURCELL, A. 2017. Applying Lessons from Glacial Isostatic Adjustment Analysis to the Antarctic Ice Sheet. *IMAS Future Sea Levels and Coastal Impacts Workshop*

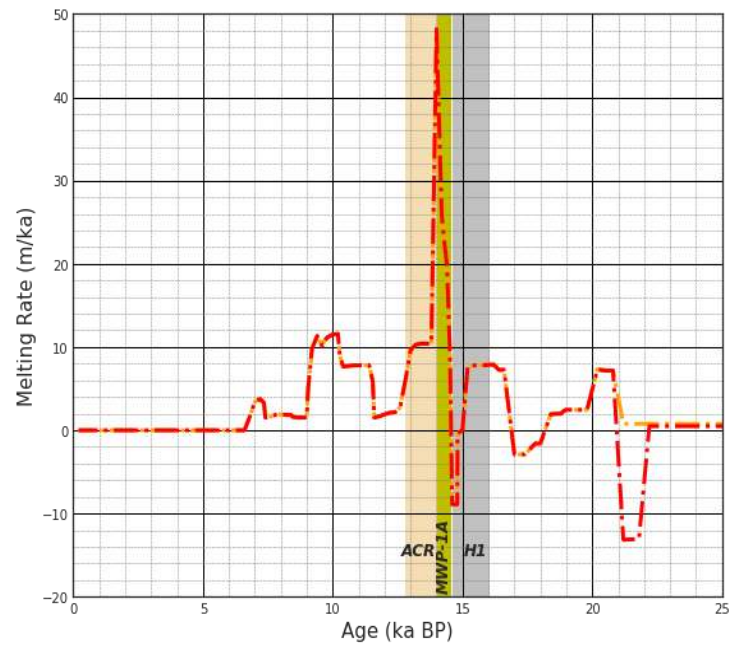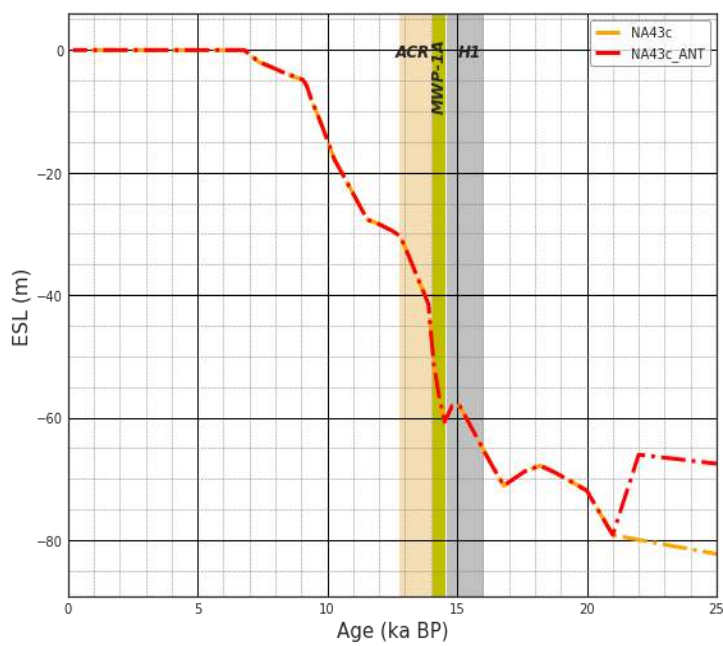PURCELL, A., TREGONING, P. & DEHECQ, A. 2016. An assessment of the ICE6G_C (VM5a) glacial isostatic adjustment

model. *Journal of Geophysical Research: Solid Earth,* 121**,** 3939-3950.

RANALLI, G. & FISCHER, B. 1984. Diffusion creep, dislocation creep, and mantle rheology. *Physics of the earth and planetary interiors,* 34**,** 77-84.

REIMER, P. J., BAILLIE, M. G., BARD, E., BAYLISS, A., BECK, J. W., BLACKWELL, P. G., RAMSEY, C. B., BUCK, C. E., BURR, G. S. & EDWARDS, R. L. 2009. IntCal09 and Marine09 radiocarbon age calibration curves, 0–50,000 years cal BP. *Radiocarbon,* 51**,** 1111-1150.

REIMER, P. J., BARD, E., BAYLISS, A., BECK, J. W., BLACKWELL, P. G., RAMSEY, C. B., BUCK, C. E., CHENG, H., EDWARDS, R. L. & FRIEDRICH, M. 2013. IntCal13 and Marine13 radiocarbon age calibration curves 0–50,000 years cal BP. *Radiocarbon,* 55**,** 1869-1887.

ROOT, B., TARASOV, L. & VAN DER WAL, W. 2015. GRACE gravity observations constrain Weichselian ice thickness in the Barents Sea. *Geophysical Research Letters,* 42**,** 3313-3320.

RUDDIMAN, W. F. 2001. *Earth's Climate: past and future,* Macmillan.

RUTT, I. C., HAGDORN, M., HULTON, N. & PAYNE, A. 2009. The Glimmer community ice sheet model. *Journal of Geophysical Research: Earth Surface,* 114.

SAMBRIDGE, M. 2016. Reconstructing time series and their uncertainty from observations with universal noise. *Journal of Geophysical Research: Solid Earth,* 121**,** 4990-5012.

SAMBRIDGE, M., GALLAGHER, K., JACKSON, A. & RICKWOOD, P. 2006. Trans-dimensional inverse problems, model comparison and the evidence. *Geophysical Journal International,* 167**,** 528-542.

SCHOOF, C. 2007. Ice sheet grounding line dynamics: Steady states, stability, and hysteresis. *Journal of Geophysical Research: Earth Surface,* 112.

SHENNAN, I. 1986. Flandrian sea-level changes in the Fenland. II: Tendencies of sea-level movement, altitudinal changes, and local and regional factors. *Journal of Quaternary Science,* 1**,** 155-179.

SHEPHERD, A., IVINS, E., RIGNOT, E., SMITH, B., VAN DEN BROEKE, M., VELICOGNA, I., WHITEHOUSE, P., BRIGGS, K., JOUGHIN, I. & KRINNER, G. 2018. Mass balance of the Antarctic ice sheet from 1992 to 2017. *Nature,* 558**,** 219-222.

SIMMS, A. R., LISIECKI, L., GEBBIE, G., WHITEHOUSE, P. L. & CLARK, J. F. 2019. Balancing the last glacial maximum (LGM) sea-level budget. *Quaternary Science Reviews,* 205**,** 143-153.

SMALL, D., BENTLEY, M. J., JONES, R. S., PITTARD, M. L. & WHITEHOUSE, P. L. 2019. Antarctic ice sheet palaeo-thinning rates from vertical transects of cosmogenic exposure ages. *Quaternary Science Reviews,* 206**,** 65-80.

SPADA, G., BARLETTA, V. R., KLEMANN, V., RIVA, R., MARTINEC, Z., GASPERINI, P., LUND, B., WOLF, D., VERMEERSEN, L. & KING, M. 2011. A benchmark study for glacial isostatic adjustment codes. *Geophysical Journal International,* 185**,** 106-132.

SPADA, G. & STOCCHI, P. 2006. *The sea level equation, theory and numerical examples,* Aracne Editrice.

STANFORD, J. D., HEMINGWAY, R., ROHLING, E. J., CHALLENOR, P. G., MEDINA-ELIZALDE, M. & LESTER, A. J. 2011. Sea-level probability for the last deglaciation: A statistical analysis of far-field records. *Global and Planetary Change,* 79**,** 193-203.

STOCKER, T. 2014. *Climate change 2013: the physical science basis: Working Group I contribution to the Fifth assessment report of the Intergovernmental Panel on Climate Change,* Cambridge University Press.

STONE, J. O., BALCO, G. A., SUGDEN, D. E., CAFFEE, M. W., SASS, L. C., COWDERY, S. G. & SIDDOWAY, C. 2003. Holocene deglaciation of Marie Byrd land, west Antarctica. *Science,* 299**,** 99-102.

SUGDEN, D. E., BALCO, G., COWDERY, S. G., STONE, J. O. & SASS III, L. C. 2005. Selective glacial erosion and weathering zones in the coastal mountains of Marie Byrd Land, Antarctica. *Geomorphology,* 67**,** 317-334.

TARASOV, L., DYKE, A. S., NEAL, R. M. & PELTIER, W. R. 2012. A data-calibrated distribution of deglacial chronologies for the North American ice complex from glaciological modeling. *Earth and Planetary Science Letters,* 315**,** 30-40.

TöRNQVIST, T. E. & HIJMA, M. P. 2012. Links between early Holocene ice-sheet decay, sea-level rise and abrupt climate change. *Nature Geoscience,* 5**,** 601.

TUSHINGHAM, A. M. & PELTIER, W. 1992. Validation of the ICE-3G Model of Würm-Wisconsin Deglaciation using a global data base of relative sea level histories. *Journal of Geophysical Research: Solid Earth,* 97**,** 3285-3304.

VAN DE PLASSCHE, O. 2013. *Sea-level Research: a Manual for the Collection and Evaluation of Data: a Manual for the Collection and Evaluation of Data,* Springer.

VIDAL, L., SCHNEIDER, R., MARCHAL, O., BICKERT, T., STOCKER, T. & WEFER, G. 1999. Link between the North and South

Atlantic during the Heinrich events of the last glacial period. *Climate Dynamics,* 15, 909-919.

WAHR, J. & ZHONG, S. 2012. Computations of the viscoelastic response of a 3-D compressible Earth to surface loading: an application to Glacial Isostatic Adjustment in Antarctica and Canada. *Geophysical Journal International,* 192, 557-572.

WEAVER, A. J., SAENKO, O. A., CLARK, P. U. & MITROVICA, J. X. 2003. Meltwater pulse 1A from Antarctica as a trigger of the Bølling-Allerød warm interval. *Science,* 299, 1709-1713.

WEBER, M., CLARK, P., KUHN, G., TIMMERMANN, A., SPRENK, D., GLADSTONE, R., ZHANG, X., LOHMANN, G., MENVIEL, L. & CHIKAMOTO, M. 2014. Millennial-scale variability in Antarctic ice-sheet discharge during the last deglaciation. *Nature,* 510, 134.

WEBSTER, J. M., BRAGA, J. C., HUMBLET, M., POTTS, D. C., IRYU, Y., YOKOYAMA, Y., FUJITA, K., BOURILLOT, R., ESAT, T. M. & FALLON, S. 2018. Response of the Great Barrier Reef to sea-level and environmental changes over the past 30,000 years. *Nature Geoscience,* 11, 426.

WHITEHOUSE, P. 2018a. Ancient ice sheet had a growth spurt. Nature Publishing Group.

WHITEHOUSE, P. L. 2018b. Glacial isostatic adjustment modelling: historical perspectives, recent advances, and future directions. *Earth surface dynamics.,* 6, 401-429.

WHITEHOUSE, P. L., BENTLEY, M. J. & LE BROCQ, A. M. 2012a. A deglacial model for Antarctica: geological constraints and glaciological modelling as a basis for a new model of Antarctic glacial isostatic adjustment. *Quaternary Science Reviews,* 32, 1-24.

WHITEHOUSE, P. L., BENTLEY, M. J., MILNE, G. A., KING, M. A. & THOMAS, I. D. 2012b. A new glacial isostatic adjustment model for Antarctica: calibrated and tested using observations of relative sea-level change and present-day uplift rates. *Geophysical Journal International,* 190, 1464-1482.

WHITEHOUSE, P. L., BENTLEY, M. J., VIELI, A., JAMIESON, S. S., HEIN, A. S. & SUGDEN, D. E. 2017. Controls on last glacial maximum ice extent in the Weddell Sea embayment, Antarctica. *Journal of Geophysical Research: Earth Surface,* 122, 371-397.

WHITEHOUSE, P. L., GOMEZ, N., KING, M. A. & WIENS, D. A. 2019. Solid Earth change and the evolution of the Antarctic Ice Sheet. *Nature communications,* 10, 503.

WOLSTENCROFT, M., KING, M. A., WHITEHOUSE, P. L., BENTLEY, M. J., NIELD, G. A., KING, E. C., MCMILLAN, M., SHEPHERD, A., BARLETTA, V. & BORDONI, A. 2015. Uplift rates from a new high-density GPS network in Palmer Land indicate significant late Holocene ice loss in the southwestern Weddell Sea. *Geophysical Journal International,* 203, 737-754.

WOODROFFE, C. D., MCGREGOR, H. V., LAMBECK, K., SMITHERS, S. G. & FINK, D. 2012. Mid-Pacific microatolls record sea-level stability over the past 5000 yr. *Geology,* 40, 951-954.

WOODROFFE, C. D. & WEBSTER, J. M. 2014. Coral reefs and sea-level change. *Marine Geology,* 352, 248-267.

WOODWARD, R. S. 1888. *On the Form and Position of the Sea Level: With Special References to Its Dependence on Superficial Masses Symmetrically Disposed about a Normal to the Earth's Surface*, US Government Printing Office.

WOOLLER, M. J., BEHLING, H., GUERRERO, J. L., JANTZ, N. & ZWEIGERT, M. E. 2009. Late Holocene hydrologic and vegetation changes at Turneffe Atoll, Belize, compared with records from mainland Central America and Mexico. *Palaios,* 24, 650-656.

WU, P. & PELTIER, W. 1984. Pleistocene deglaciation and the Earth's rotation: a new analysis. *Geophysical Journal International,* 76, 753-791.

WU, P. & VAN DER WAL, W. 2003. Postglacial sealevels on a spherical, self-gravitating viscoelastic earth: effects of lateral viscosity variations in the upper mantle on the inference of viscosity contrasts in the lower mantle. *Earth and Planetary Science Letters,* 211, 57-68.

WU, P., WANG, H. & STEFFEN, H. 2012. The role of thermal effect on mantle seismic anomalies under Laurentia and Fennoscandia from observations of Glacial Isostatic Adjustment. *Geophysical Journal International,* 192, 7-17.

YOKOYAMA, Y., DE DECKKER, P., LAMBECK, K., JOHNSTON, P. & FIFIELD, L. K. 2001. Sea-level at the Last Glacial Maximum: evidence from northwestern Australia to constrain ice volumes for oxygen isotope stage 2. *Palaeogeography, Palaeoclimatology, Palaeoecology,* 165, 281-297.

YOKOYAMA, Y. & ESAT, T. M. 2011. Global climate and sea level: Enduring variability and rapid fluctuations over the past 150,000 years. *Oceanography,* 24, 54-69.

YOKOYAMA, Y., ESAT, T. M., THOMPSON, W. G., THOMAS, A. L., WEBSTER, J. M., MIYAIRI, Y., SAWADA, C., AZE, T.,

MATSUZAKI, H. & OKUNO, J. I. 2018. Rapid glaciation and a two-step sea level plunge into the Last Glacial Maximum. *Nature,* 559, 603.

YOKOYAMA, Y., HIRABAYASHI, S., GOTO, K., OKUNO, J. I., SPROSON, A. D., HARAGUCHI, T., RATNAYAKE, N. & MIYAIRI, Y. 2019a. Holocene Indian Ocean sea level, Antarctic melting history and past Tsunami deposits inferred using sea level reconstructions from the Sri Lankan, Southeastern Indian and Maldivian coasts. *Quaternary Science Reviews,* 206, 150-161.

YOKOYAMA, Y., LAMBECK, K., DE DECKKER, P., JOHNSTON, P. & FIFIELD, L. K. 2000. Timing of the Last Glacial Maximum from observed sea-level minima. *Nature,* 406, 713.

YOKOYAMA, Y., PURCELL, A. & ISHIWA, T. 2019b. Gauging Quaternary Sea Level Changes Through Scientific Ocean Drilling. *Oceanography,* 32, 64-71.

ZINKE, J., REIJMER, J., THOMASSIN, B., DULLO, W.-C., GROOTES, P. & ERLENKEUSER, H. 2003. Postglacial flooding history of Mayotte lagoon (Comoro archipelago, southwest Indian Ocean). *Marine Geology,* 194, 181-196.

ZWALLY, H. J., GIOVINETTO, M. B., BECKLEY, M. A. & SABA, J. L. 2012. Antarctic and Greenland drainage systems, GSFC cryospheric sciences laboratory. *Available at icesat4. gsfc. nasa. gov/cryo_data/ant_grn_drainage_systems. php. Accessed March,* 1, 2015.

Appendices

Figure S1 Comparison of NAIS models' deglaciation history: (a) North American contribution to post-LGM global sea-level rise. (b) NAIS ice melting rate, the green vertical bar is the timing of MWP-1A, grey bar is Heinrich Event 1 (H1), yellow bar stands for Antarctic Cold Reversal (Parrenin et al., 2007).

(a)

W12 20 ka BP RMS=443.213

IJ05_R2 20 ka BP RMS=277.412

ANT20 20 ka BP RMS=701.160

ICE-6G_C 20 ka BP RMS=245.933

(b)
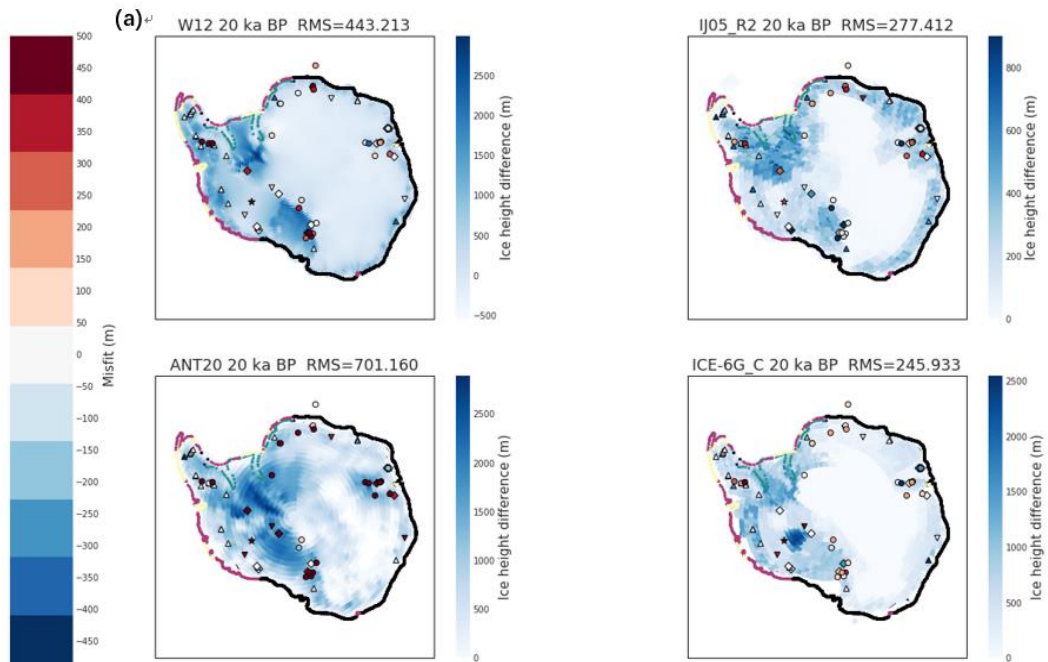
Figure S2 (a) Four models' comparison with observational constraints. Subtitle contains the model name, time slice and total RMS value. Figure background is the model's ice height difference (IHD: different models have different colourbar scales). The surrounding points are reconstructed AIS grounding line at 20 ka BP that contains two possible scenarios for Weddell Sea (shown in purple and green), the level of uncertainty of grounding line positions is indicated by colour: black (speculative), yellow (measured), purple and green (inferred). Points shown above background are observational data corresponding to site number (Figure 4.1). Circles are data sites with absolute (or close absolute) value, up and down-triangles are minimum and maximum limiting data, rhombus are range data (i.e., contains upper and lower limits) and stars are approximate value. If model reconstructions at a data site satisfies one of these limiting data then a zero misfit is assumed. Positive misfit means model value is larger than observation. (b) IHD at 113 observation sites (see Figure 4.1) at 20 ka BP. Up and down-triangle are minimum and maximum limiting data, squares are absolute data. The vertical lines and text are the sector of data on the right side.

Glacio-Geological Data Comparison

(b)

W12 15 ka BP RMS=261.410

IJ05_R2 15 ka BP RMS=329.422

ANT20 15 ka BP RMS=780.817

ICE-6G_C 15 ka BP RMS=276.444

Glacio-Geological Data Comparison

(c)

W12 10 ka BP RMS=259.946

IJ05_R2 10 ka BP RMS=215.939

ANT20 10 ka BP RMS=686.542

ICE-6G_C 10 ka BP RMS=192.349

Misfit (m)

Ice height difference (m)

Glacio-Geological Data Comparison

(d)

W12 5 ka BP RMS=126.647

IJ05_R2 5 ka BP RMS=127.111

ANT20 5 ka BP RMS=127.252

ICE-6G_C 5 ka BP RMS=141.599
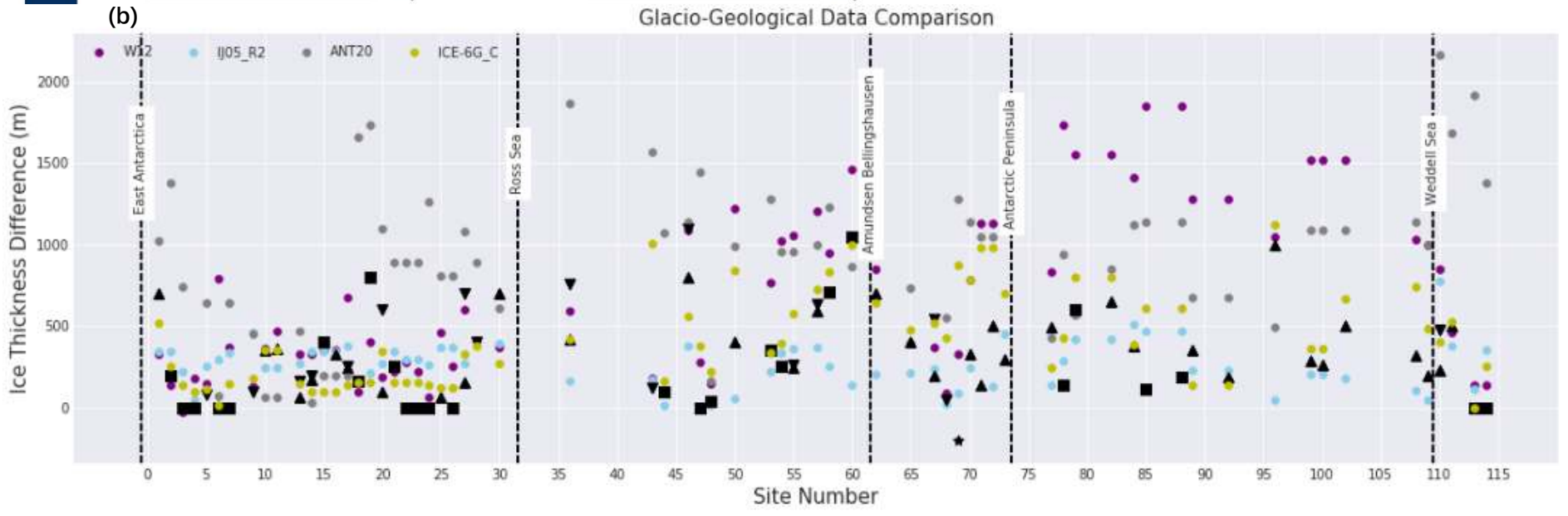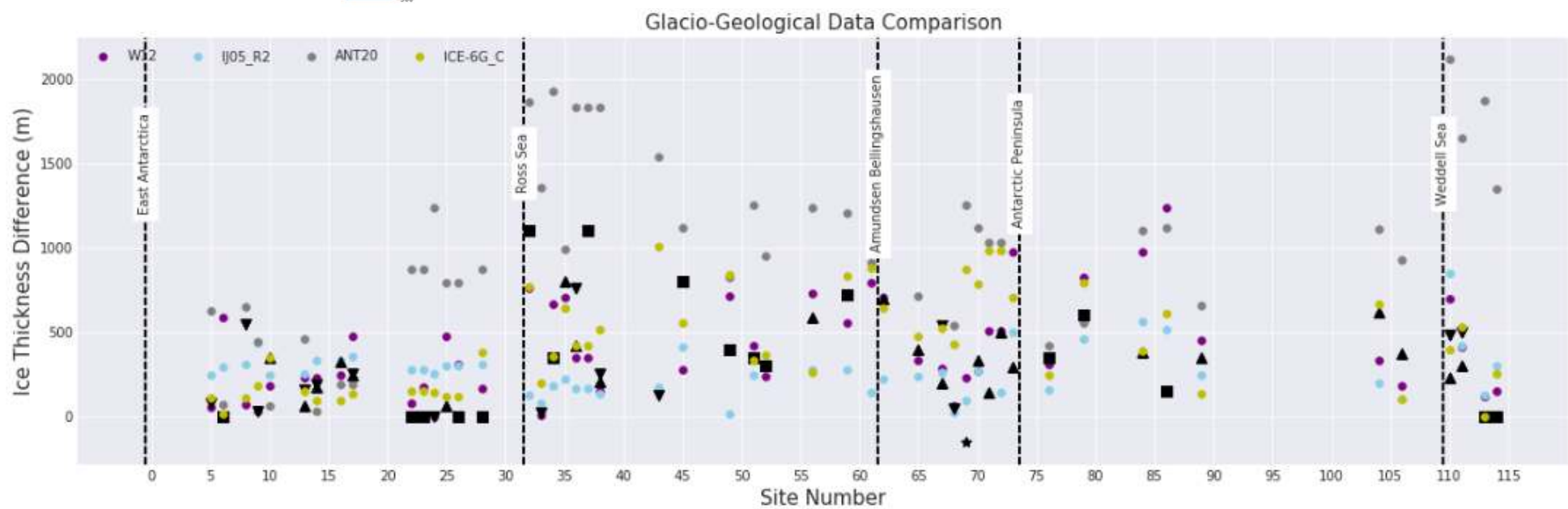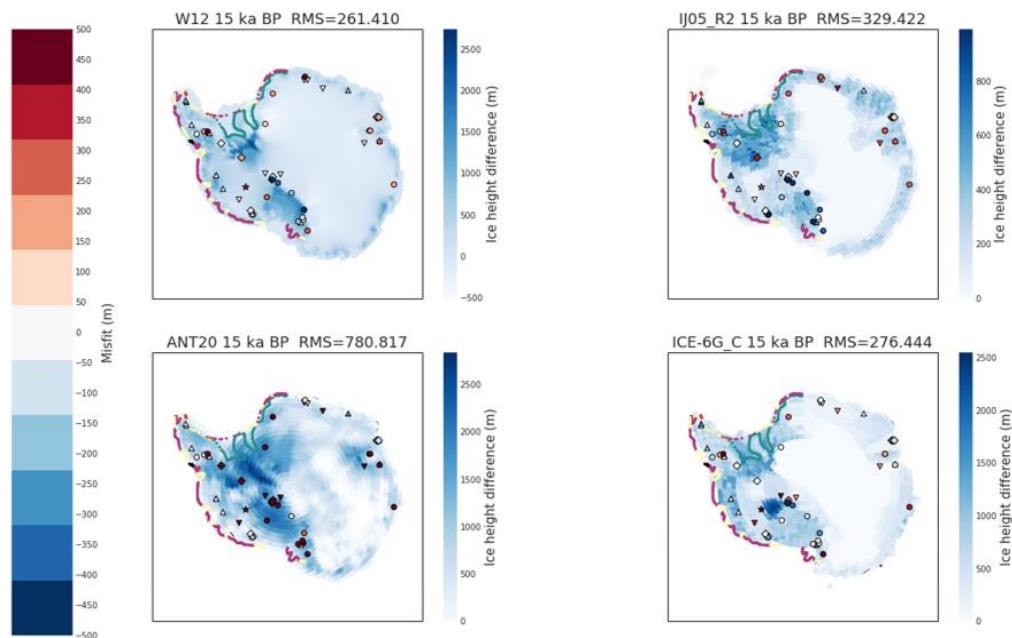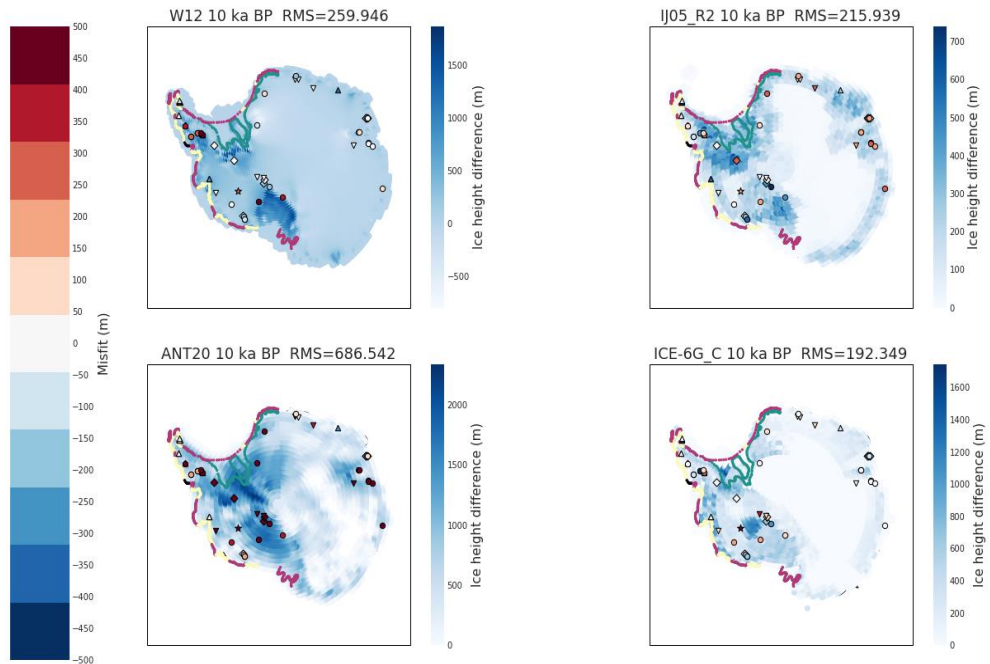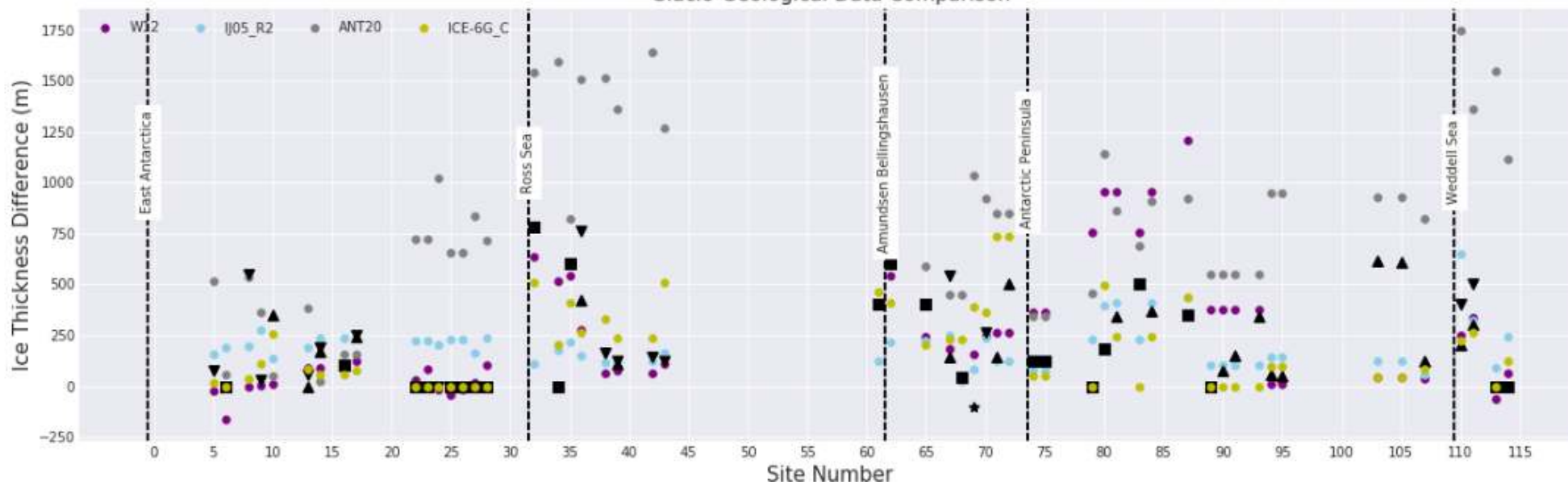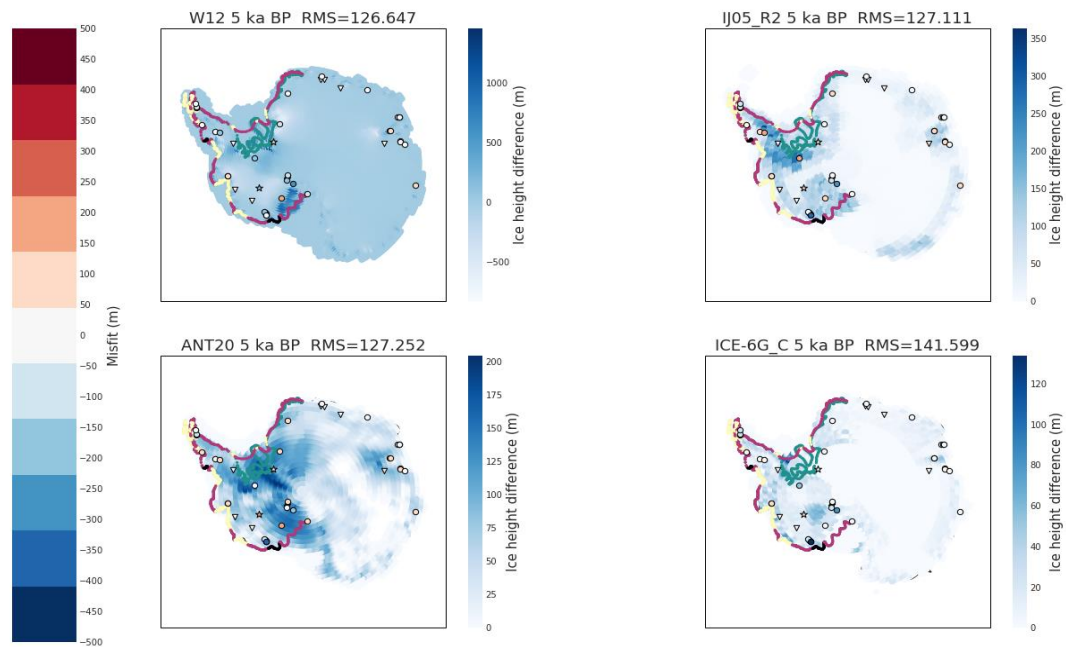
Glacio-Geological Data Comparison
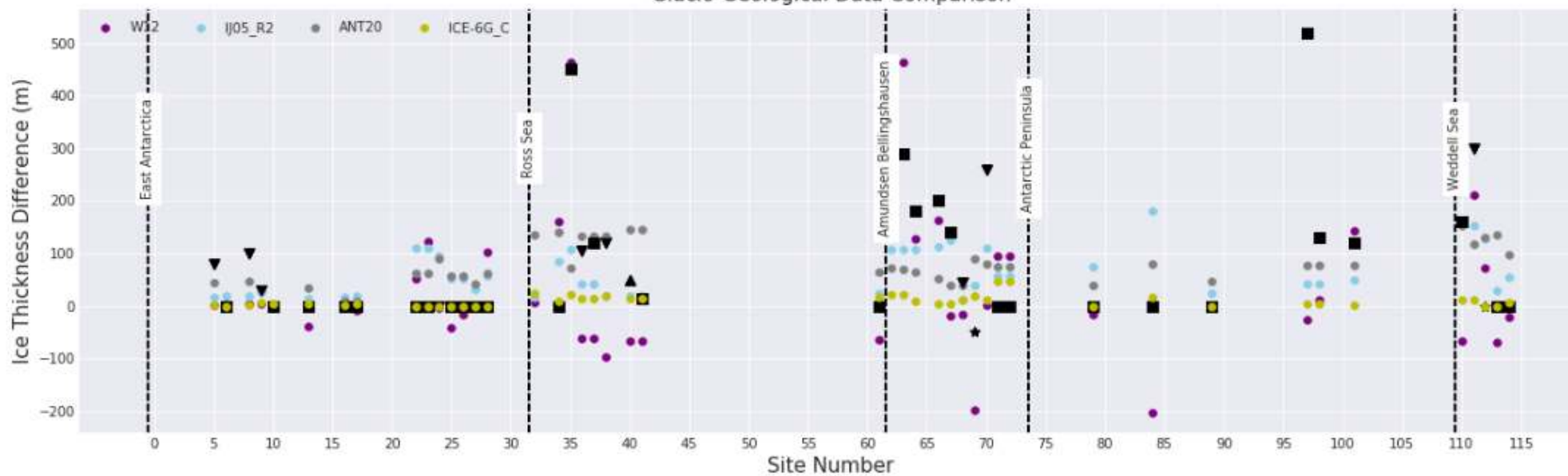
Fitting L14 Dataset
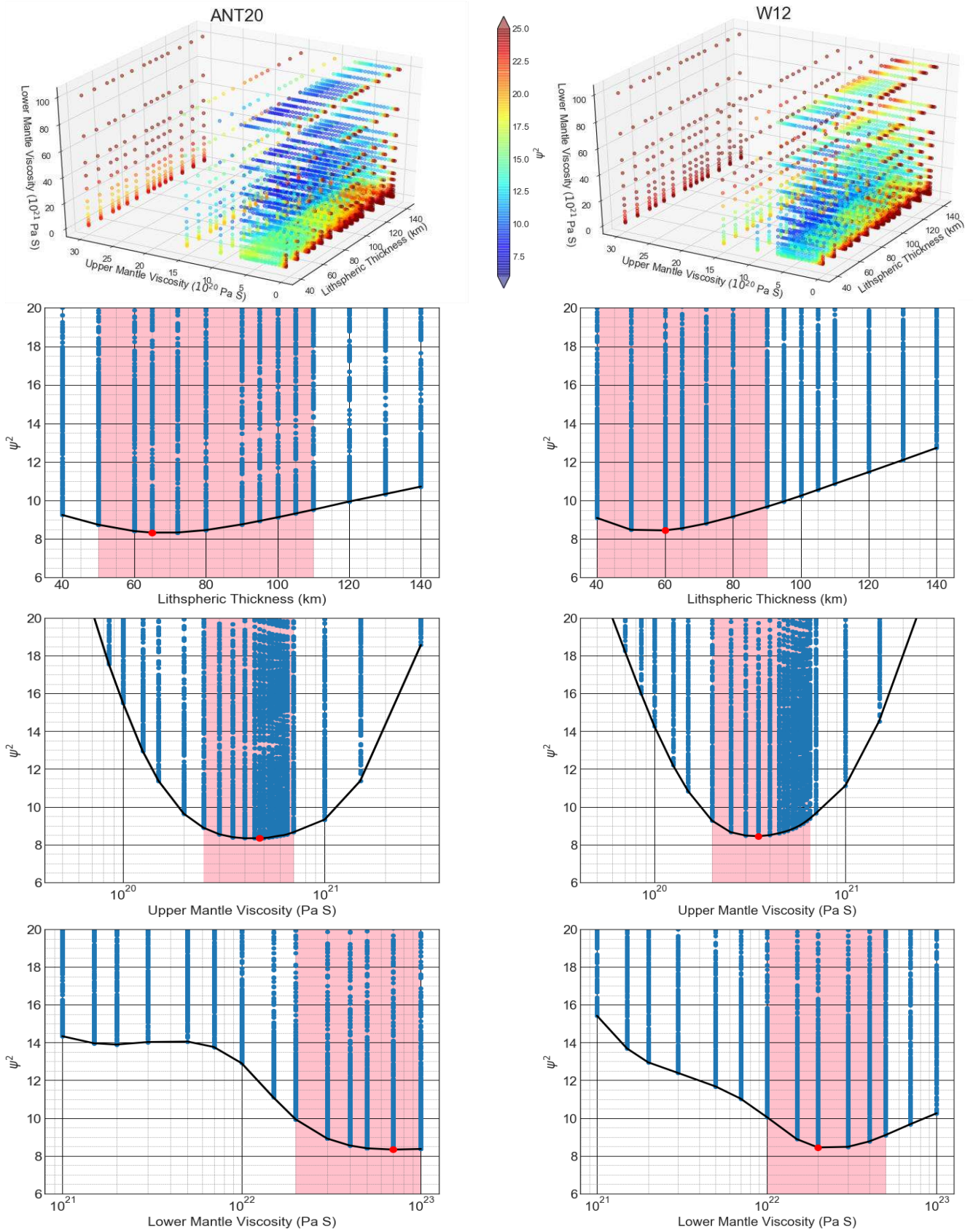
Figure S3 Earth-parameter solution for different AIS models and observational datasets. (a) 3D scatter plots of the variance values. (b,c,d) The variance value as a function of lithospheric thickness, upper and lower Mantle viscosity. The blue points are the tested Earth parameters. The black line indicates the minimum variance function and the red dot indicates the minimum value. The red bands indicate 95% confidence interval.
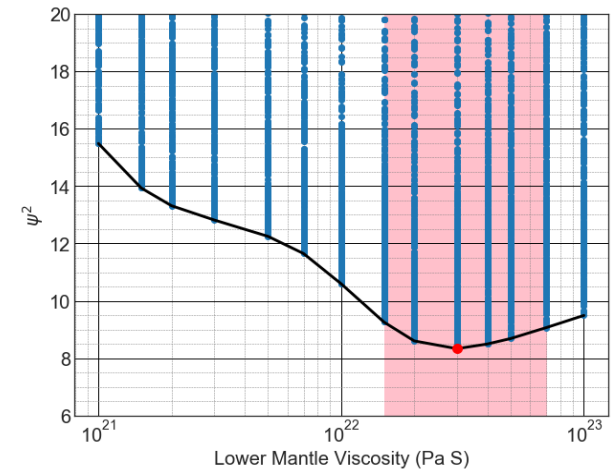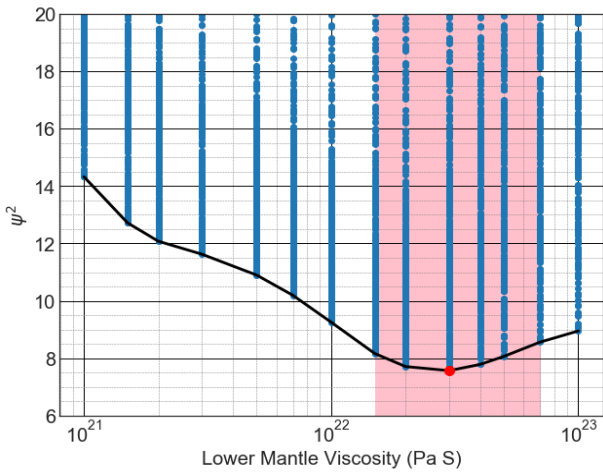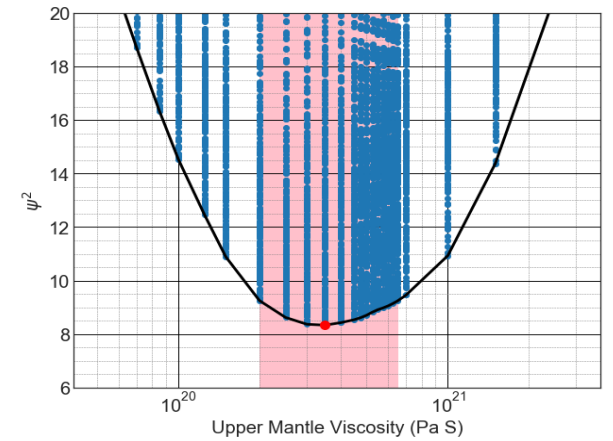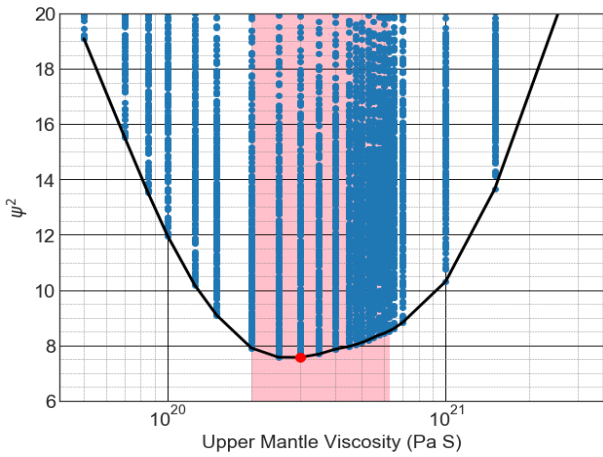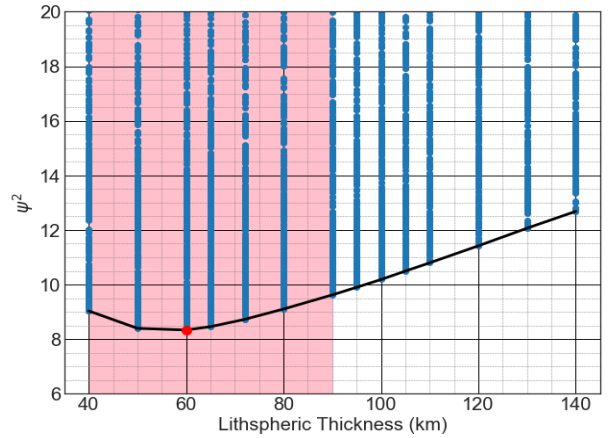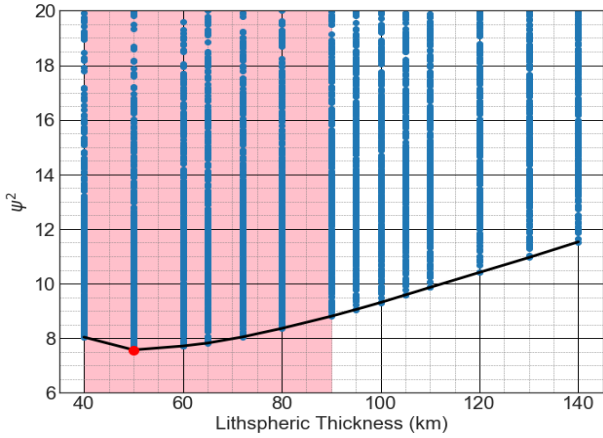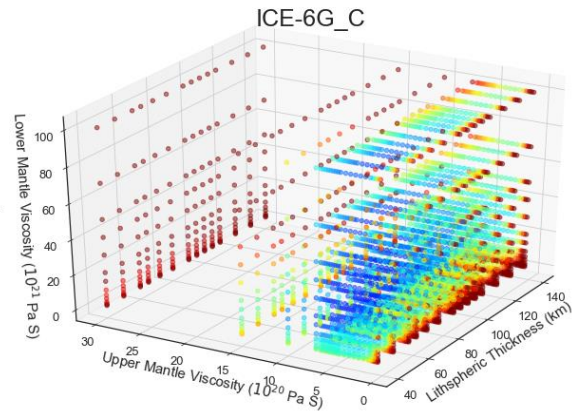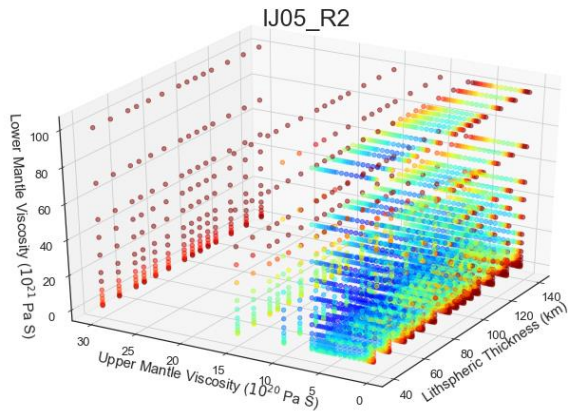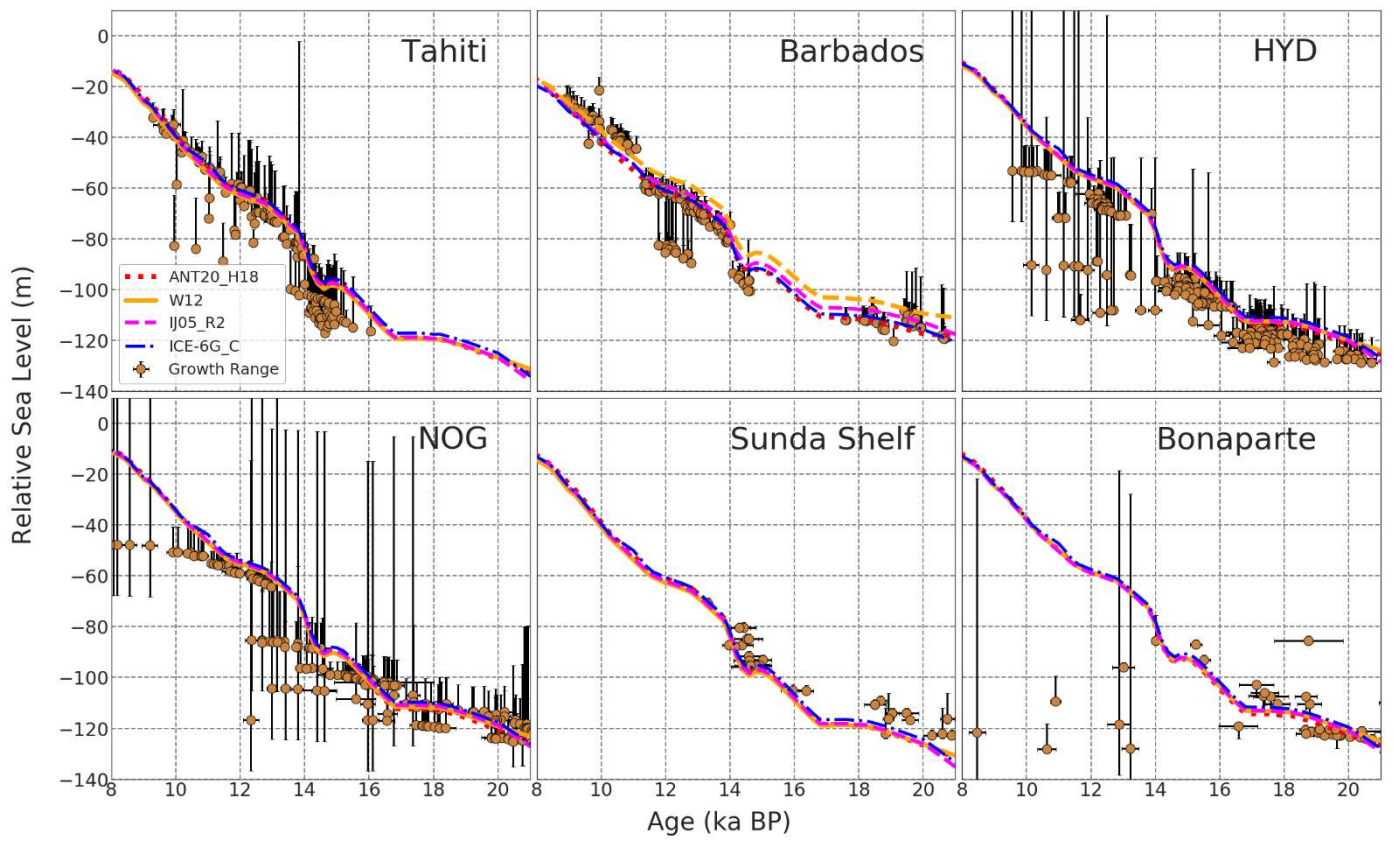
Fitting H18 Dataset
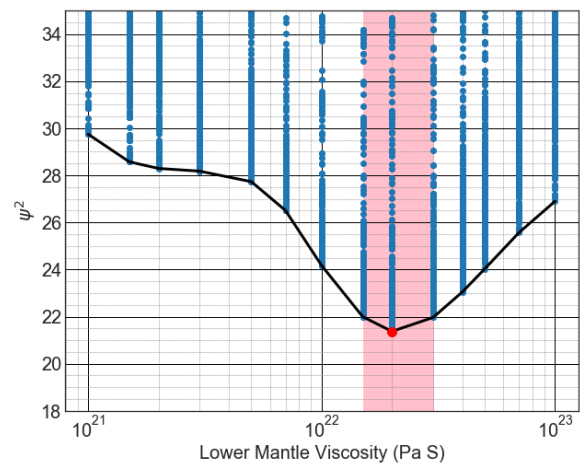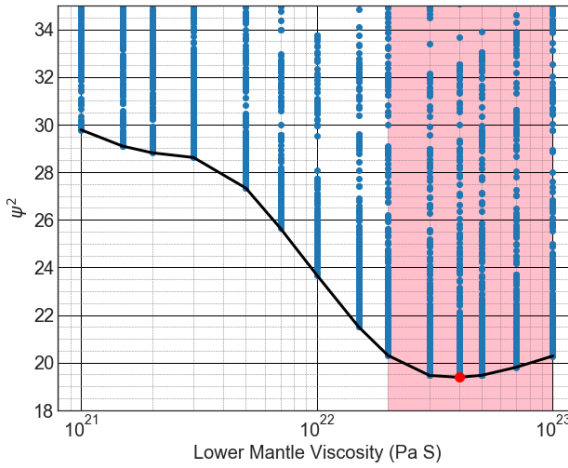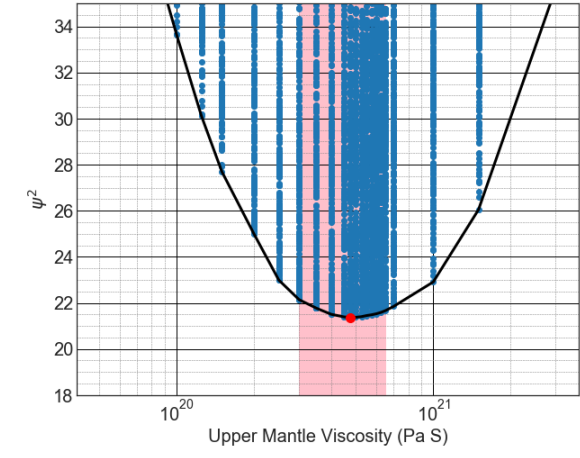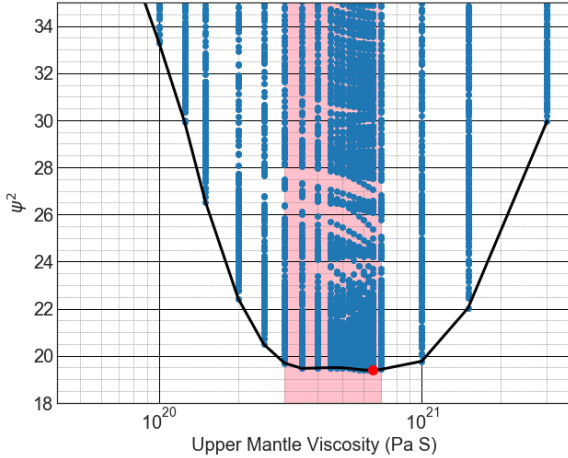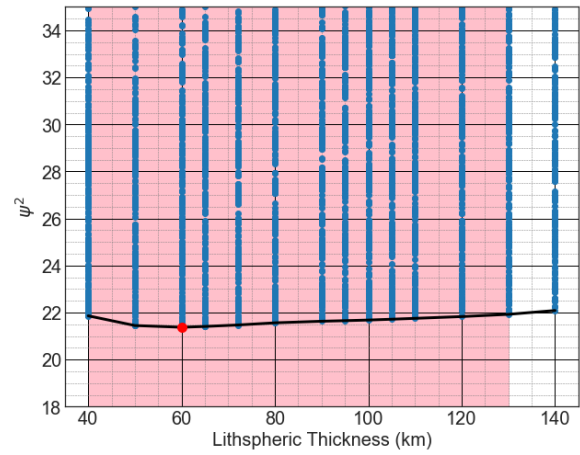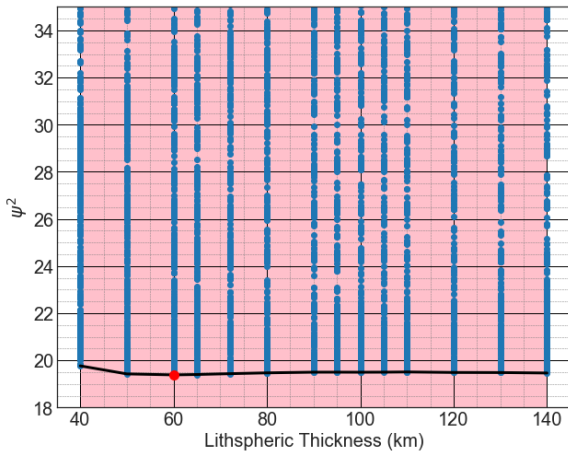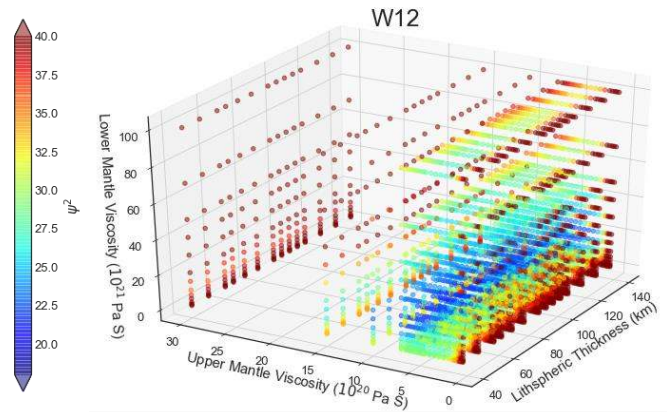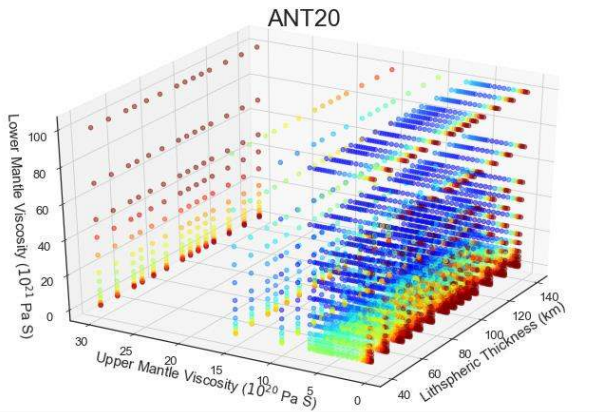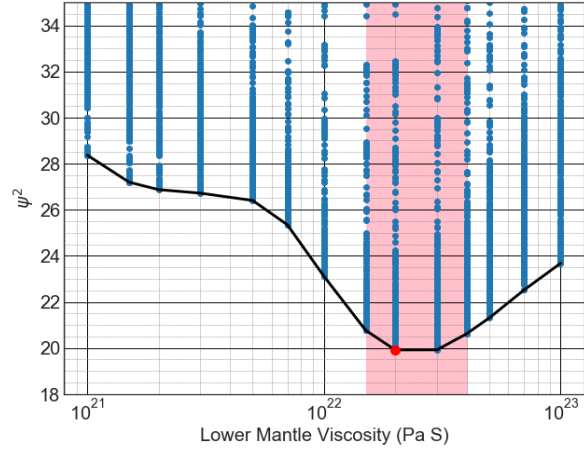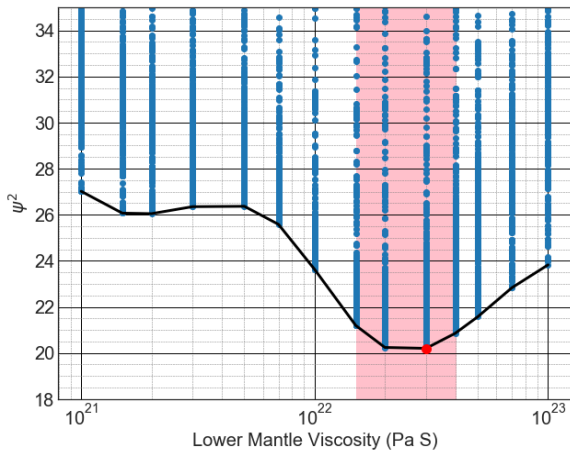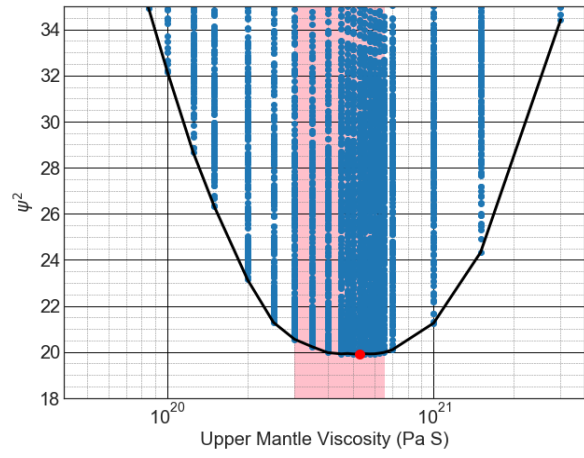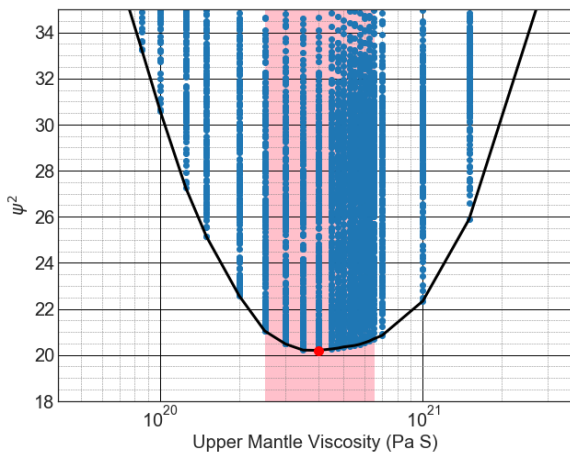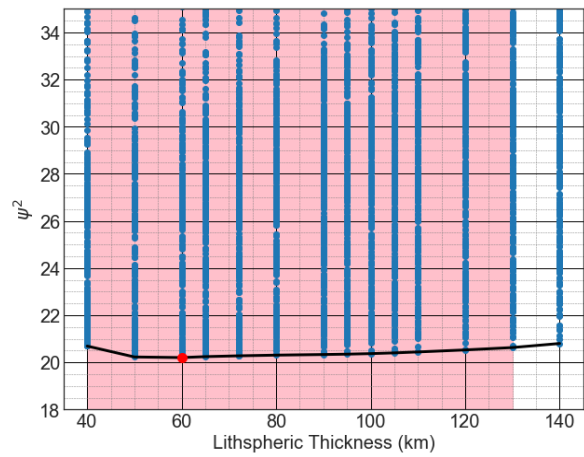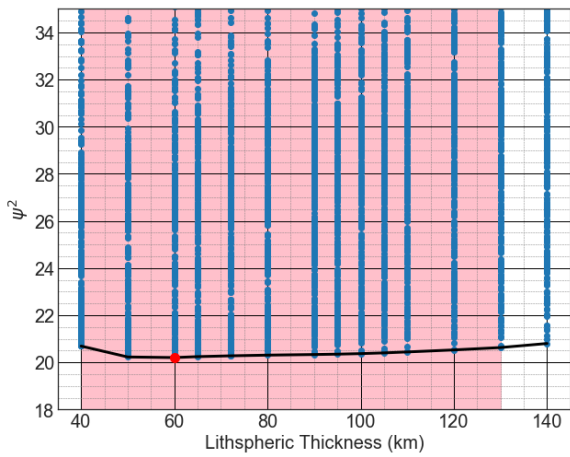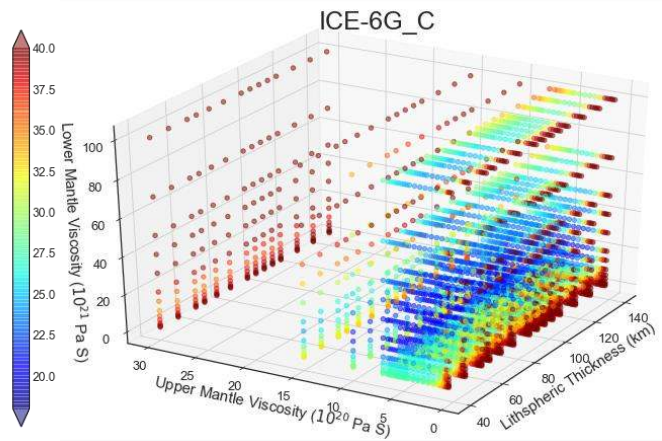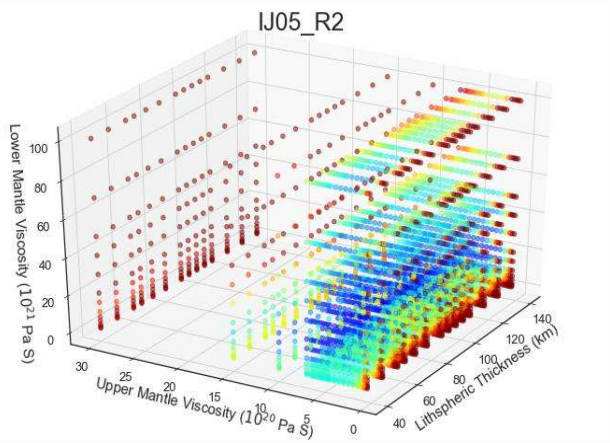
Figure S4 The sea-level predications by ice models for H18 dataset with corresponding best-fitting Earth models for selected sites. The growth ranges showing here are from the original publication. The horizontal error bars are 2 σ uncertainties for age estimations from the literature. HYD = Hydrographer's Passage, NOG = Noggin Pass, both from Great Barrier Reef.
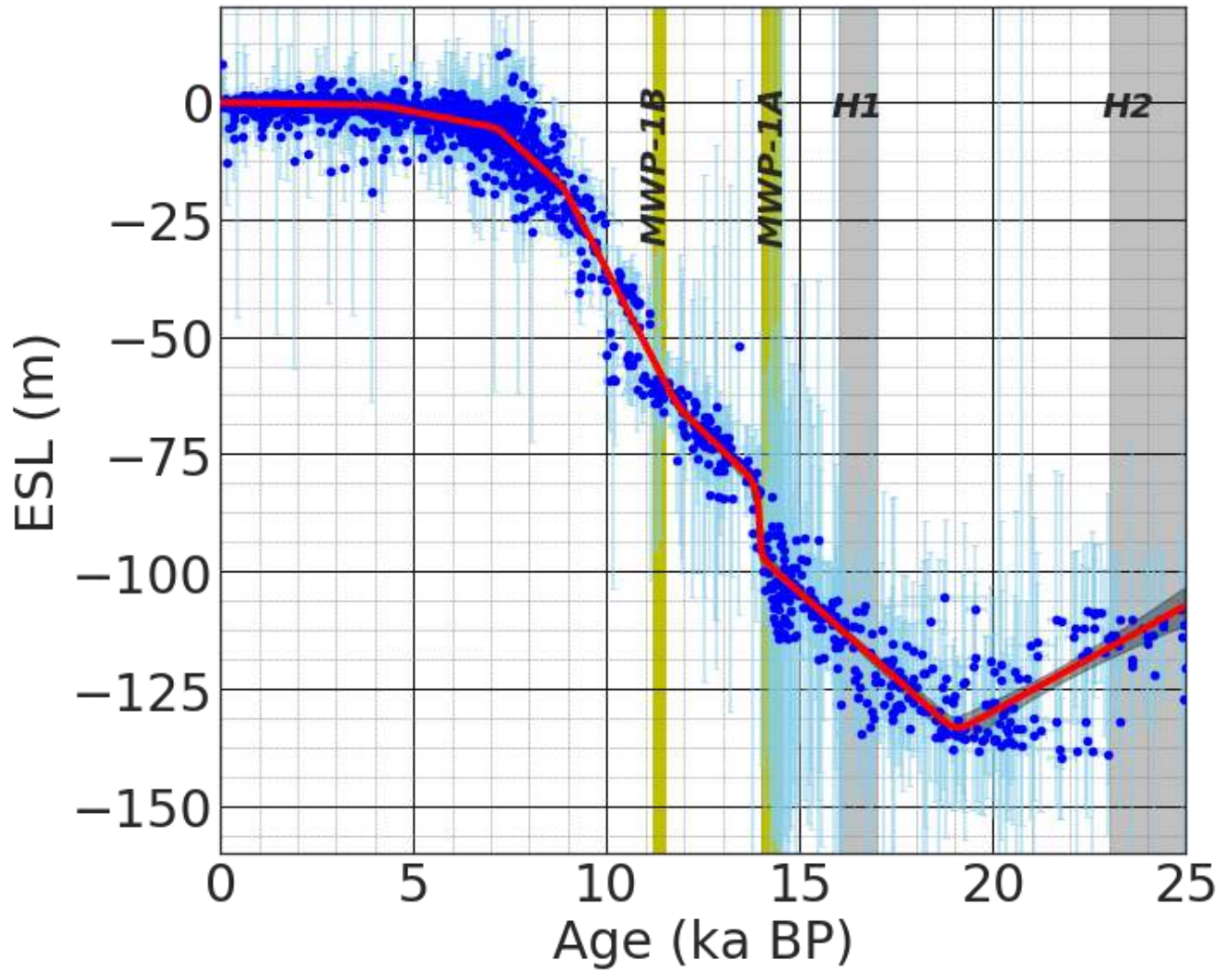
Figure S5 A example of using McMC algorithms to interpolate H18 dataset without considering dating uncertainties.

Table S1. Summary of Normalized Meltwater Fingerprint Value

Site	Longitude	Latitude	Normalized Sea-level change ELIS[#]	WAIS
Tahiti	-149.58	-17.53	1.18	1.14
Barbados	-59.54	13.04	0.66	1.18
Sunda Shelf	108.58	4.16	1.09 +	1.15
Hydrographer's Passage	150.24	-19.67	0.98	1.15
Noggin Pass	146.57	-17.10	0.98	1.15
Bonaparte Gulf	128.02	-12.18	0.98	1.16

+ The locations of record in Argentine Shelf and Sunda Shelf are not identical, the value shown here is the averaged value.

* The results showing here is from author's previous study named 'A joint method for inverting the amplitude and source of meltwater pulse 1A using sea-level constraints'.

ELIS and WAIS stand for East Laurentide Ice Sheet and West Antarctic Ice Sheet